UNIVERSITY OF SOUTHAMPTON

FACULTY OF PHYSICAL SCIENCES
AND
ENGINEERING

Electronics and Computer Science

Plasmonic Mirror for Light-trapping in Thin Film Solar Cells

by

Rufina Steffi Anthony Sesuraj

A thesis for the degree of Doctor of Philosophy

April 2014

UNIVERSITY OF SOUTHAMPTON

ABSTRACT

FACULTY OF PHYSICAL SCIENCES AND ENGINEERING

Electronics and Computer Science

Doctor of Philosophy

PLASMONIC MIRROR FOR LIGHT-TRAPPING IN THIN FILM SOLAR CELLS

by Rufina Steffi Anthony Sesuraj

Microcrystalline silicon solar cells require an enhanced absorption of photons in the near-bandgap region between 700-1150nm. Conventional textured mirrors scatter light and increase the path length of photons in the absorber by total internal reflection. However, these mirrors exhibit a high surface roughness which degrades the performance of the microcrystalline silicon device. An alternative solution is to use metal nanoparticles with low surface roughness to scatter light. An illuminated metal nanoparticle exhibits a resonant or plasmonic excitation which can be tuned to enable a strong scattering of light. This work aims to develop an efficient near-infrared light-scattering system using randomly arranged metal nanoparticles near a mirror.

Situating the nanoparticles at the rear of the solar cell helps to target weakly absorbed photons and eliminate out-coupling losses by the inclusion of a rear mirror. Simulation results show that the electric field driving the plasmonic resonance can be tuned with particle-mirror separation distance. The plasmonic scattering is maximised when the peak of the driving field intensity coincides with the intrinsic resonance of the nanoparticle.

An e-beam lithography process was developed to fabricate a pseudo-random array of Ag nanodiscs near a Ag mirror. The optimized plasmonic mirror, with 6% coverage of 200nm Ag discs, shows higher diffusive reflectivity than a conventional textured mirror in the near-infrared region, over a broad angular range. Unlike a mirror with self-organised Ag islands, the mirror with Ag nanodiscs exhibits a low surface roughness of 13.5nm and low broadband absorption losses of around 10%.

An 8.20% efficient thin n-i-p μc-Si:H solar cell, with the plasmonic mirror integrated at the rear, has been successfully fabricated. The optimised plasmonic solar cell showed an increase of 2.3mA in the short-circuit current density (J_{sc}), 6mV in the open-circuit voltage (V_{oc}) and 0.97% in the efficiency (η), when compared to the planar cell counterpart with no nanodiscs. The low surface roughness of the plasmonic mirror ensures no degradation in the electrical quality of the μc-Si:H layer – this is also confirmed by the constant value of the fill factor (FF). The increase in J_{sc} is demonstrated to be mainly due to optical absorption enhancement in the near-infrared region as a result of plasmonic scattering, by detailed calculation of the exact photogenerated current in the plasmonic and planar devices, for the 700-1150nm wavelength range.

Contents

List of Acronyms

PV	Photovoltaic
TFSC	Thin film solar cell
TCO	Transparent Conducting Oxide
SOI	Silicon-on-Insulator
VHF	Very high frequency
PECVD	Plasma-enhanced chemical vapour deposition
NIR	Near-infrared
TIR	Total internal reflection
AFM	Atomic force microscopy
SEM	Scanning electron microscope
TEM	Transmission electron microscopy
EBL	Electron-beam lithography
FDTD	Finite-difference time-domain
DDA	Discrete dipole approximation
FEM	Finite element method
TFSF	Total-field scattered-field
PML	Perfectly matched layer
LSP	Localised surface plasmon
PSP	Propagating surface plasmon
AR	Anti-reflection
IS	Integrating sphere
EQE	External quantum efficiency
AID	Angular intensity distribution
WARS	Wavelength-angle resolved scattering

FF	Fill-factor
PMMA	Poly(methyl methacrylate)
MMA	Methyl methacrylate
MIBK	Methyl isobutyl ketone
IPA	Isopropyl alcohol
CAD	Computer-aided design
SCCM	Standard cubic centimetre per minute
STP	Standard temperature and pressure
SMU	Source measure unit
AIST	National Institute of Advanced Industrial Science and Technology
SNC	Southampton Nanofabrication Centre

Declaration of Authorship

I, RUFINA STEFFI ANTHONY SESURAJ
declare that this thesis entitled
PLASMONIC MIRROR FOR LIGHT-TRAPPING IN THIN FILM SOLAR CELLS
and the work presented in it are my own and has been generated by me as the result of my own original research.

I confirm that:

- This work was done wholly or mainly while in candidature for a research degree at this University;
- Where any part of this thesis has previously been submitted for a degree or any other qualification at this University or any other institution, this has been clearly stated;
- Where I have consulted the published work of others, this is always clearly attributed;
- Where I have quoted from the work of others, the source is always given. With the exception of such quotations, this thesis is entirely my own work;
- I have acknowledged all main sources of help;
- Where the thesis is based on work done by myself jointly with others, I have made clear exactly what was done by others and what I have contributed myself;
- Parts of this work have been published as:

1. R.S.A. Sesuraj, T.L. Temple and D.M. Bagnall , *Optical Characterization of a Spectrally Tunable Plasmonic Reflector for Application in Thin Film Silicon Solar Cells,* Solar Energy Materials & Solar Cells, vol. 111, pp.23-30, 2013.

2. R.S.A. Sesuraj, T.L. Temple and D.M. Bagnall, *Tunable Low-loss Plasmonic Mirror for Diffuse Optical Scattering,* Applied Physics Express, vol. 5, pp.125205-1–125205-3, 2012.

3. R.S.A. Sesuraj, T.L. Temple and D.M. Bagnall, *Spectrally Tunable nanoplasmonic reflector for thin film Si Solar Cells,* SPIE Proceedings, vol.8457, doi:10.1117/12.956502, SPIE Optics and Photonics, San Diego, 2012.

4. R.S.A. Sesuraj, T.L. Temple and D.M. Bagnall, *Spectrally Tunable Plasmonic Light Trap for Thin Film Si Solar Cells,* Proceedings of the 8th Photovoltaic Science and Application Technology Conference, pp.185-188, Newcastle upon Tyne, England, 2012.

5. R.S.A. Sesuraj, T.L. Temple and D.M. Bagnall, *Diffuse Reflectance and Absorption Characterisation of a Plasmonic Back Reflector for Application in Thin Film Si Solar Cells,* Material Research Society Online Proceedings, vol. 1391, doi:10.1557/opl.2012.854, MRS Fall Meeting, Boston, 2011.

6. R.S.A. Sesuraj, T.L. Temple and D.M. Bagnall, *Design, Fabrication and Characterisation of a Nanoplasmonic Back Reflector for a-Si:H Thin Film Solar Cells,* Proceedings of the 7th Photovoltaic Science and Technology Conference, pp.17-20, Edinburgh, Scotland, 2011.

Signed: ....

Date:..

Acknowledgements

I would like to thank Prof. Darren M. Bagnall and Prof. Harold M.H. Chong for providing me with the opportunity to conduct this research and for their continued motivation and encouragement over the years as my supervisors. A special thanks goes to Dr. Mark C. French for his invaluable guidance during my early years at ECS and for supporting my decision to pursue research after my undergraduate degree. I am very grateful to Dr. Tristan L. Temple for the inspiring discussions on plasmonics. Dr. Temple's contribution as a co-author for the papers published as parts of this thesis is also acknowledged.

I would like to thank all the staff and members of the Nano Research Group for their support over these 4 years, particularly, Dr. David Payne, Dr. Stuart Boden and Dr. Asa Asadollahbaik for their help with optical characterisation techniques. I am grateful to all the cleanroom technical staff at the Southampton Nanofabrication Centre, especially Jim and Peter Ayliffe for technical help with e-beam lithography and Dr. Owain Clark for his help with the ALD system. I would like to thank Dr. Yudong Wang for useful discussions on e-beam lithography.

I am very grateful to JSPS for providing me with the short-term fellowship to spend four months at AIST in Tsukuba, Japan. I truly enjoyed learning about Japanese culture and visiting beautiful places around Japan. As a result of the JSPS fellowship, I was also able to successfully fabricate plasmonic microcrystalline silicon solar cells at AIST. I would like to thank Dr. Michio Kondo for giving me the permission to work in his group and Dr. Hitoshi Sai for his technical help with the PECVD process and for training me on solar cell characterisation techniques. I would also like to thank Sai-san and his family for making me feel welcome in Tsukuba. I must also acknowledge the encouragement and support by Prof. Darren M. Bagnall, Prof. Harold M.H. Chong, Dr. Tristan L. Temple and Prof. James S. Wilkinson for my application to the JSPS programme.

I would like to thank Nick, Angela, Jess and everyone at Heatherdeane for their cheerful company over these years. A special thanks to Robert for the many enjoyable discussions on life, philosophy and research.

I am grateful to Justin Chettan for his understanding and encouragement during the final stages of the write-up. I am extremely grateful to my parents for always being there for me, especially during some very trying and difficult times. Your love and support is invaluable to me.

[This page intentionally left blank]

Chapter 1

Introduction

In 1839, the discovery of the photovoltaic effect, the conversion of photon energy from sunlight into electricity, laid the foundations for photovoltaic (PV) technology [1]. The solar irradiance reaching the surface of the Earth (Figure 1.1) is dependent on the wavelength of electromagnetic radiation. A solar cell should be optimised to absorb photons over the range of wavelengths in the solar spectrum and efficiently use these absorbed photons to generate electricity.

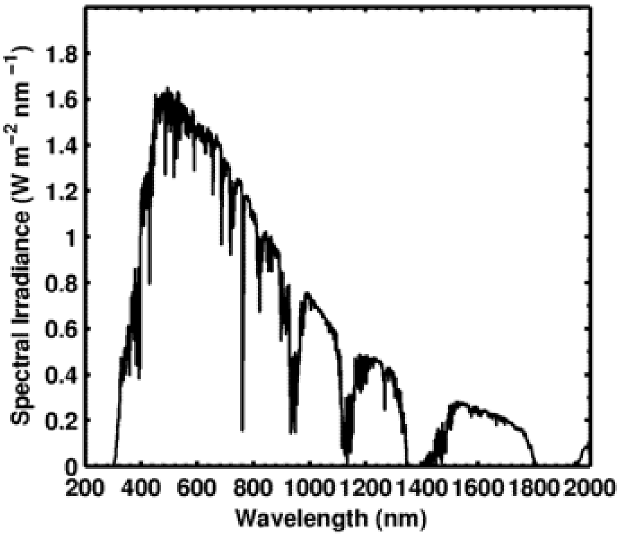

Figure 1.1 The AM1.5 Solar Spectrum [2]

The first reported PV Si solar cell was fabricated at Bell Labs in 1954 [3]. This cell exhibited 6% efficiency, where efficiency is defined as the ratio of the maximum output power to a given input solar power. Today, within 60 years, PV has matured into a large-scale commercial technology and has created a solid niche for itself in the renewable energy industry. Single-junction crystalline Si (c-Si) solar cells, which currently form approximately 90% of the PV market production, exhibit module efficiencies between 16-20%, with the best laboratory cell efficiencies reported of 25% [4].

It is interesting to briefly analyse the research trend which has led to the maturation of PV technology from 1839 to date. From 1839 to 1954, the motivation for research was to explain the fundamental physics of PV and to discover the first steps towards the processing of a suitable semiconductor for PV applications. As a result, important research milestones such as the explanation of the photoelectric effect by Einstein [5], the development of the Czochralski process for single-crystal silicon [6] and the fabrication of prototype Se and Ge photocells [7, 8] were successfully established during this time.

After 1954 the research focus shifted to developing techniques for improved efficiency of c-Si solar cells. Within 20 years, the research-cell efficiency of c-Si solar cells had already been developed to 15%. Given a reasonable efficiency and the establishment of a growth process for c-Si solar cells, the focus in the late 1970s had shifted to the large-scale production of solar cells. Consequentially, the main challenge was to manufacture efficient solar cells in a cost-effective way; this led to a new area of research on thin-film solar cells.

1.1 Thin Film Solar Cells

1.1.1 Current Status of Thin Film Photovoltaics

The current PV market is dominated by c-Si solar cells which offer module efficiencies of around 16-20% [4]. However, the biggest bottleneck in the production of these solar cells is the unavoidably high material cost associated with the use of crystalline silicon wafers (c-Si) or multi-crystalline silicon wafers (mc-Si). Also, there is a very limited scope for any further increase in the efficiency of single-junction c-Si solar cells: the reported record efficiency for laboratory cells is already very high and rather close to the theoretical efficiency limit predicted for a single-junction device [9, 10]. Hence, the challenge faced by the current PV market is to reduce the material costs without encountering a significant trade-off in the efficiency of the solar cell. Thin film photovoltaics have long been considered to have the potential for good efficiencies at significantly lower costs.

Chopra *et al.* define thin films as materials created by the "*random nucleation and growth processes of individually condensing/reacting atomic/ionic/molecular species on a substrate"* [11]. Thin films usually have thicknesses in the order of 0.001μm to 10μm. It is possible to manipulate the structural and chemical properties of thin films by tuning the deposition parameters involved in a process. Some of the main semiconductors developed for thin film solar cells (TFSCs) are cadmium telluride (CdTe), copper indium gallium selenide (CIGS), hydrogenated amorphous silicon (a-Si:H), and hydrogenated microcrystalline silicon (μc-Si:H).

TFSCs made of CdTe or CIGS require only 1-3μm of semiconductor material to achieve high efficiencies in the range of 15-20% [9]. However, raw materials such as Cd, In, Se, Te and Ga are scarce and hence, in the long-run, CIGS and CdTe devices are fundamentally less able to meet the large-scale production requirements of the PV market [9, 11]. Comparatively, Si is available in significant quantities in its raw form and hence Si-based TFSCs could be viewed as the main candidates for a sustained large-scale production.

1.1.2 Atomic structure of Si allotropes: a-Si:H and μc-Si:H

Si-based TFSCs include a-Si:H and μc-Si:H solar cells. The main benefit of the thin Si TFSCs when compared to c-Si solar cells is the reduced thickness of the semiconductor material used in these devices: the thickness of a-Si:H layer is in the order of 100nm whereas μc-Si:H layers are typically around 1-3μm in thickness. These thicknesses are usually two to three orders of magnitude less than the thickness required for a c-Si device. Thin film Si devices also have the added advantage of being developed using low temperature ($T<600^{0}C$) plasma-enhanced chemical vapour deposition techniques (PECVD) [11]. In PECVD, the chemical reaction between source gases in a generated plasma is used for the deposition of thin layers on a given substrate. This allows for the deposition of TFSCs on low-cost substrates such as glass. In chapter 7 of this work, we will briefly discuss a PECVD process used for the fabrication of μc-Si:H solar cells.

A detailed discussion of the growth process and atomic-structure of the thin Si films is beyond the scope of this work. However, we will very briefly highlight the main differences between the atomic structures of a-Si:H and μc-Si:H in order to appreciate the uniqueness of these two allotropes of Si. On an atomic scale, the structure of a-Si:H is predominantly random, with a short-range order in the arrangement of Si atoms. That is, on a short-range, each Si atom is covalently bonded to four other Si atoms. However, due to differences in bond-angles and bond-lengths over the long range, a-Si has a random arrangement of Si atoms as opposed to the periodic, crystalline atomic structure of c-Si [14].

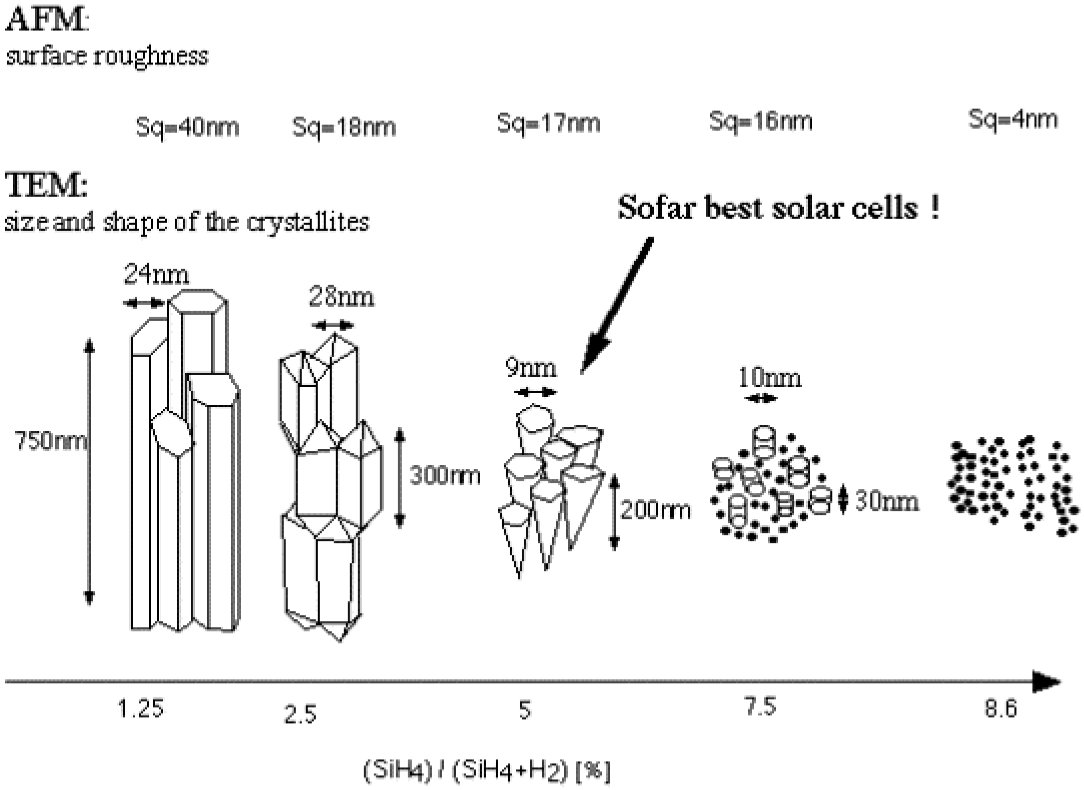

Figure 1.2: Variety in microstructure of μc-Si:H obtained by changing the ratio of SiH_4 to H_2, in a VHF-PECVD deposition process. [12, 13]

The variation in bond-angle and bond-length in a-Si also leads to bonds being weaker and eventually breaking to form unconnected Si bonds or dangling bonds. Due to the existence of dangling bonds, hydrogen passivation is required for a-Si layers. The first μc-Si:H layers were developed in 1968 [15] just 2 years after the development of the first a-Si:H solar cell. μc-Si:H consists of nanometre-sized grains of crystalline silicon which are obtained merely by changing the ratio of SiH_4 to H_2 (the same gases are used for deposition of a-Si:H) in the PECVD process. Vallat-Sauvain *et al.* discovered that only a certain ratio of SiH_4 to H_2 results in the formation of μc-Si:H layers with grain sizes useful for fabrication of working TFSCs (Figure 1.2) [13]. A high dilution of H_2 results in large crystallites which cannot be used for solar cells as they cause cracks (i.e. structural defects) and induce shunts in the device; a very low dilution of H_2 results in only amorphous layers [12, 13]. It was also demonstrated experimentally that in general, μc-Si:H layers unlike a-Si:H layers, do not suffer from light-induced degradation or the Staebler-Wronski effect [12].

As mentioned before, a solar cell needs to be optimised for both, optical and electrical performance. In this work, we choose to focus only on μc-Si:H TFSCs. In Sections 1.1.3 and 1.1.4 we will focus on the optical and electrical properties of μc-Si:H solar cells.

1.1.3 Optical Absorption in μc-Si:H

Figure 1.3 compares the absorption coefficient spectrum for μc-Si:H, c-Si and a-Si:H layers, across an energy range from 2.5eV to 0.7eV which approximately corresponds to spectral wavelengths between 496nm to 1770nm, respectively. The absorption coefficient (α) is a function of the wavelength of the incident light. The optical absorption depth is defined as the inverse of α. The absorption depth for a photons of a given energy, is defined as the distance travelled by the photons in a given semiconductor layer before being absorbed or before reaching 1/e of the initial intensity.

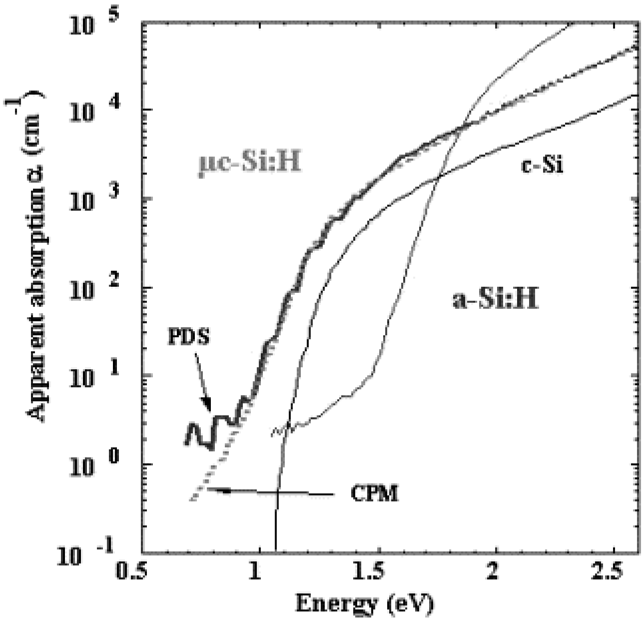

Figure 1.3: Optical absorption coefficient (α) of μc-Si:H, c-Si and a-Si:H. The abbreviations CPM and PDS in the figure stand for Constant Photocurrent Method (refer [16]) and Photothermal Deflection Spectroscopy, respectively; these are methods used to measure the α values for the μc-Si:H layer deposited by VHF-PECVD. [9]

It can be observed that a-Si:H exhibits higher values of α when compared to μc-Si:H and c-Si, for energy ranges down to its near band-gap edge of 1.75eV (or a wavelength of 700nm). Below 1.75eV, the values of α for a-Si:H exhibit a sharp decrease. As observed in

Figure 1.3, μc-Si:H has a bandgap close to that of c-Si. Hence, μc-Si:H shows a significantly better absorption of near-infrared (NIR) photons when compared to a-Si.

For example, at 1.4eV (or a wavelength of approximately 885nm), the value for α exhibited by μc-Si:H is 1000cm^{-1} which corresponds to an absorption depth of 10μm. The corresponding value of α for c-Si is approximately 200cm^{-1}, corresponding to an absorption depth of 50 μm and that for a-Si:H is only 4cm^{-1} corresponding to a significantly large absorption depth of 2500μm. This simple calculation shows that in order to absorb a NIR photon with a wavelength of 885nm, the required thickness of the μc-Si:H layer is 5 times less than that of the c-Si layer and almost 1000 times less than the required thickness for the a-Si:H layer.

1.1.4 Electrical Properties of a μc-Si:H solar cell

A typical single junction c-Si solar cell consists of a highly doped, thin (less than 1μm) n-type emitter which is diffused into a p-type base. The resulting depletion region is also thin. The electric field-assisted drift process only occurs over the width of the thin depletion region; i.e. it does not extend into the active regions of the solar cell. As a result, c-Si solar cells with the p-n junction structure rely on diffusion as the predominant process for movement of charge carriers[1]. The diffusion lengths of minority carriers in c-Si solar cells are typically in the order of 100μm [17]. However in the case of doped μc-Si:H, the typical ambipolar diffusion lengths lie in the range of 0.2μm to 0.8μm [9] as a result of grain boundary defects and defects introduced by dopants in the atomic structure.

Hence if μc-Si:H solar cells were to rely primarily on the diffusion process, then there is a clear discrepancy between the thickness of the μc-Si:H layer required for carrier diffusion and the thickness of the layer required for efficient absorption of NIR photons. As already noted in Section 1.2, the thickness of the μc-Si:H layer needs to be around 10μm, in order to absorb a photon with a wavelength of 885nm. Therefore, it is not possible to have a μc-Si solar cell with a p-n junction, as there is a high probability that the electrons and holes will recombine shortly after separation, due to low diffusion lengths.

---

[1] The interested reader can refer to Appendix 1 for the basics of a p-n junction solar cell.

As a result, μc-Si:H solar cells, unlike c-Si solar cells have a p-i-n (or n-i-p) structure as shown in Figure 1.4[2]. The details of the structures will be explained in Section 1.2. An intrinsic (i-) layer is introduced between the doped layers and the resultant electric field is experienced over the entire thickness of the i-layer. As a result, in μc-Si:H solar cells, the creation of electron-hole pairs occurs in the i-layer and the movement of the charge carriers is assisted by the electric field, and hence by drift rather than diffusion. Shah *et al.* present a very simple and useful relation (Equation 1) to prove that the drift length L_{drift} is higher than the diffusion length L_{diff} and significantly higher than conventional i-layer thicknesses of 1-3μm for μc-Si:H solar cells. [18, 19, 9][3]:

$$\frac{L_{drift}}{L_{diff}} = \frac{\gamma \cdot L_{diff}}{d_i} \qquad (\mathbf{1})$$

$$\gamma = \frac{V_{bi} \cdot q}{k \cdot T} \qquad (\mathbf{2})$$

Where, d_i is the thickness of the i-layer in a p-i-n μc-Si:H solar cell and V_{bi} is the voltage across the i-layer as a result of the electric field across this layer. q is the elementary charge, k is Boltzmann's constant and T is the reference temperature. In Equation 1, substituting a typical value of γ=40 [9], and L_{diff} < 1μm, it can clearly be seen that L_{drift} will be significantly larger than L_{diff} for conventional i-layer thicknesses of 1-3μm. Hence due to a significantly large L_{drift} value, the p-i-n structure of a μc-Si:H solar cell ensures efficient collection of charge carriers.

---

[2] A band diagram of the p-i-n structure explained in this Section is included in Appendix 1 for the interested reader.

[3] The interested reader can refer to the paper by Shah *et al.* [9] for a complete derivation of this relation and an example calculation. As the reference already includes a detailed work-out and example, in this work we have avoided a repetition of any example calculations. We have only included equation (1) and (2) for the sake of completeness in the understanding of the drift-assisted charge transport mechanism in μc-Si:H devices.

1.2 Light-trapping for μc-Si:H solar cells

In Section 1.1.3, we observed that μc-Si:H demonstrates a higher optical absorption of NIR photons in the 800-1100nm wavelength range when compared to c-Si and a-Si:H. In a p-i-n μc-Si:H solar cell, the useful absorption of the photons occurs in the i-layer. Figure 1.3 shows that the i-layer needs to have a maximum thickness of 15μm in order to absorb NIR photons of wavelengths up to 1100nm; this thickness is significantly less than the conventional wafer thickness of a c-Si solar cell. However, the main motivation behind TFSCs is the fabrication of a low-cost yet efficient device. Hence, the thickness of the i-layer needs to be reduced, preferably to a few microns, for better electrical quality and for a decreased material cost.

Given that the conventional i-layer thickness is around 1-3μm, NIR photons of wavelengths larger than 800nm will be poorly absorbed if they were to pass through the i-layer only once. Light-trapping schemes are designed to increase the probability of absorption of photons (in a target wavelength range) by increasing their apparent optical path lengths in the absorber layer. An enhanced optical absorption of photons directly correlates to an increase in the photogenerated current and efficiency of the device. In this Section, we will briefly review different light-trapping schemes for μc-Si:H solar cells.

1.2.1 Light-Trapping using Textured TCOs and Mirrors

Figure 1.4 shows the two common configurations of μc-Si:H solar cells: n-i-p and p-i-n. The difference in the two types of configurations lies in the order of deposition of the layers. In a p-i-n solar cell, the substrate is usually a textured transparent conducting oxide (TCO) on glass followed by the deposition of p-, i- and n- layers, a thin TCO layer and a planar Ag layer respectively. The textured TCO has to exhibit low resistivity, high transparency, and excellent light-scattering properties for a target wavelength range, as explained later in this Section. The Ag layer serves as the rear electrical contact and as a back mirror. The textured front TCO in the p-i-n structure is also the front electrical contact. In an n-i-p structure, the substrate is usually a textured TCO on a Ag back contact, followed by the deposition of the n-, i- and p- layers, a TCO with thickness optimised for anti-reflection, and Ag grid-contacts which serve as the front electrode. The p-, i-, n- layers are usually deposited by PECVD as explained in Section 1.1.2. Due to a conformal growth process [20],

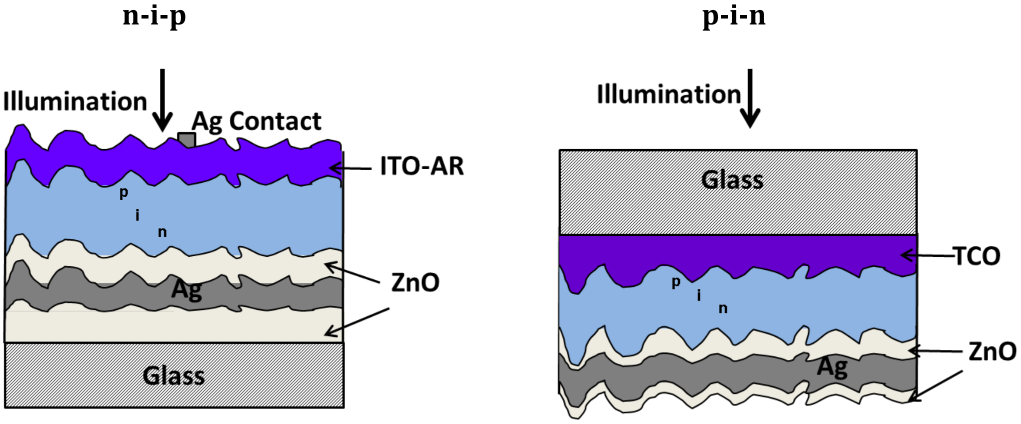

Figure 1.4: Two common configurations of μc-Si:H solar cells: n-i-p and p-i-n (from [20])

the texture of the TCO on the substrate is transferred onto the subsequent layers, thereby affecting the surface roughness and morphology of the μc-Si:H solar cell.

The purpose of the front and back surface texture in a TFSC is to aid light-trapping. Light-trapping enables the coupling of energy from a photon into the absorber layer by increasing the optical thickness of the absorber as perceived by an incident photon. The front surface texture randomises the direction of the incident light such that the light undergoes multiple passes within the high-refractive index absorber due to total internal reflection (TIR). The texture at the rear surface of the solar cell targets light which is poorly absorbed; this includes light in the wavelength range of 800-1100nm for μc-Si:H solar cells. Assuming a random textured surface at the rear, the poorly absorbed light is preferentially scattered into the high-index absorber layer and the optical path length of the light is increased due to TIR. Several structures have been designed and implemented for purposes of light-trapping in μc-Si:H solar cells. In this Section, we will briefly review some of these light-trapping structures.

Asahi-U type TCOs (textured SnO_2) with randomly arranged 'pyramidal' structures (Figure 1.5b), are commercially used as front TCOs in p-i-n devices. They can also be used for texturing the rear mirror in n-i-p devices. Asahi-U type structures have a surface roughness (σ_{rms}) of approximately 30nm [20]. The σ_{rms} of a textured substrate is a crucial parameter as it determines the trade-off between the light-scattering properties of the substrate and the quality of the μc-Si:H layer grown conformally on the substrate. A substrate with features exhibiting high aspect ratios (and hence a high value for σ_{rms}) may cause defects in the μc-Si:H layer, thereby impairing the electrical performance of the solar cell – this aspect is reviewed in detail in Chapter 3 of this work. The haze value (defined as the ratio of diffuse reflectance to total reflectance) of textured TCOs decreases with increasing wavelength; the texture of Asahi-U is specifically optimised for light-trapping in a-Si:H solar cells rather than for μc-Si:H solar cells, although several studies also use this TCO as the conventional substrate for μc-Si:H solar cells [20].

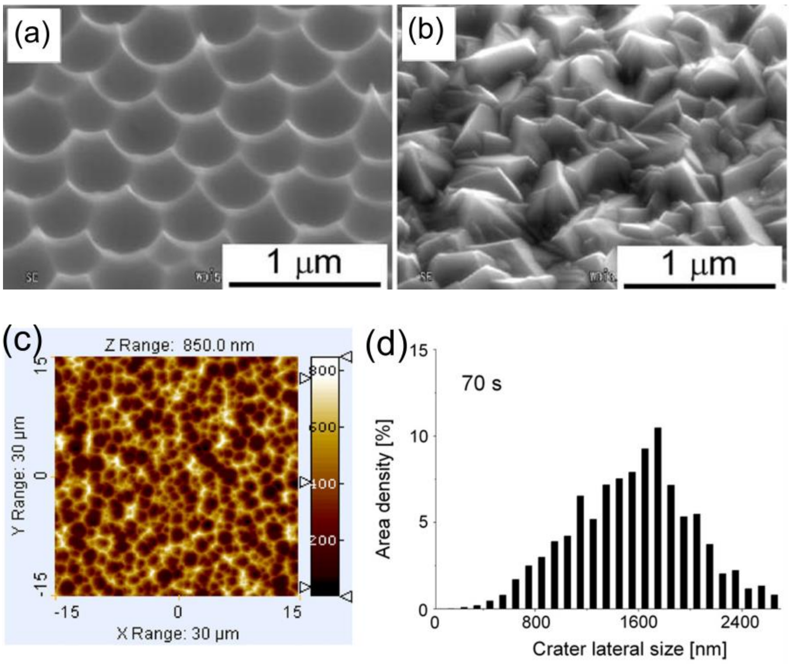

Figure 1.5: SEM image of: (a) Dimple-patterned Al substrate obtained by anodic oxidation of Al at 195 V [18] (b) Asahi-U type textured SnO_2 on glass [18] (c) AFM image of ZnO-crater texture obtained by etching ZnO for 70s in HCl (d) Lateral crater size distribution for ZnO substrate in (c) [21]

Despite the fact that Asahi-U is not an optimal texture for μc-Si:H solar cells, a recent study by Sai *et al*. showed that texturing p-i-n devices using an Asahi-U type TCO results in an increase in the photocurrent (by 3mA) and efficiency (by 2%) when compared to corresponding values for flat p-i-n devices (with polished front and rear surfaces) [18]. Similar enhancement, with slightly higher values for photocurrent and efficiency, were also demonstrated for n-i-p devices with Ag mirrors textured by Asahi-U substrates.

Sai and Kondo fabricated a textured back mirror by depositing Ag onto patterned Al 'dimple' structures (Figure 1.5a), obtained by anodic oxidation of Al. The photocurrent is shown to be dependent on the period of the Al dimples; for an n-i-p device with a 1µm thick i-layer, the maximum photocurrent is obtained when the period of the Al dimples is also 1µm. The n-i-p device with the dimple-textured back mirror also demonstrates a better efficiency than its flat device counterpart and a device fabricated with a back mirror exhibiting an Asahi-U texture.

Another TCO which is commonly used in µc-Si:H solar cells and which can be textured for light-trapping purposes is ZnO (or Ga:ZnO). Bottler *et al*. use a textured ZnO substrate prepared by etching sputtered ZnO in HCl, for texturing the rear Ag mirror in n-i-p devices (Figure 1.5c) [21]. The photocurrent of the device is shown to be dependent on the lateral size of craters formed by etching the ZnO. However, we note here that despite high values for the σ_{rms} (approximately 150nm) for the etched ZnO texture, the authors rule out any detrimental effects on the quality of the µc-Si:H deposited onto the textured mirror.

We observe that the self-ordered dimple pattern developed by Sai and Kondo is similar to the ZnO craters used by Bottler *et al*. for texturing the back mirror in n-i-p devices. However, the σ_{rms} of the mirror patterned by Al dimples (approximately 50nm) is significantly less when compared to the σ_{rms} of the mirror patterned by ZnO craters; a low-surface roughness value is definitely a key advantage of the Al dimple-texture over the etched ZnO texture .

Hänni *et al*. recently reported a p-i-n device with a record efficiency of 10.9%, with a textured ZnO layer as a front TCO [22]. The natural texture of ZnO deposited by low pressure plasma chemical vapour deposition is used for light-scattering purposes. However, in this study, the authors highlight the disadvantage of incurring defects in the µc-Si:H layer deposited onto the textured ZnO substrate. Several post-deposition treatments, (such as hydrogen plasma treatment[4]) are suggested to improve the electrical performance of the solar cell grown on the rough substrate.

---

[4] A detailed review of the required post-cell deposition treatments is beyond the scope of this work. The interested reader can refer the relevant paper cited in this Section.

Although textured substrates may exhibit good light-scattering properties, the main disadvantage is the high surface roughness of these substrates which deteriorates the quality of the μc-Si:H layer [23, 24]. Hence, there is a motivation for research into other methods for light-scattering in thin solar cells. Recently, a flattened light-scattering substrate with a two-dimensional (2D) ZnO grating and a Ag reflector has been proposed to overcome the problem of high surface roughness [25]. In the following Section, we will introduce the concept of using metal nanostructures with low surface roughness, to scatter light.

1.2.2 Plasmonic Light-Trapping

The interaction of light, of a given wavelength with a metal nanostructure results in the resonant oscillation of the electron cloud on the surface of the nanostructure. It is possible to tune this resonance, termed as the plasmonic resonance, to enable a strong scattering or absorption of light by the nanostructure. The plasmonic resonance will be explained in detail in Chapter 2. Here, it is sufficient to note that a resonant metal nanoparticle can be tuned to predominantly scatter or absorb light in a target wavelength range by varying the size, shape, metal type of the particle and refractive index of the surrounding homogenous medium.

The motivation to exploit the unique optical behaviour of metal nanoparticles has resulted in the emergence of several new applications across different fields ranging from applications for sensors [26] to applications in photodetectors and solar cells [27, 28]. In the medical field, for instance, gold nanoparticles have been used in photo-thermal therapy to absorb photons in the NIR and convert the photon energy to heat in order to destroy cancer cells [29]. Only recently in 2013, NASA proposed a very novel space application where the strong optical force fields, created during plasmonic resonance in metal nanostructures, can be used to propel small spacecrafts [30].

To date, there have been only a handful of studies on the use of metal nanostructures for light-scattering in μc-Si:H solar cells. This is partly because development of μc-Si:H is still a relatively new process which itself is undergoing several optimisations, with record efficiencies still being reported for μc-Si:H devices with conventional texturing [22]. In this work we propose the integration of metal nanostructures, near the metal mirror of a n-i-p μc-Si:H solar cell to optimise light-scattering near the band-edge of μc-Si:H. Our aim will be to firstly understand the mechanism of light-scattering by nanoparticles near a planar mirror. Next, we will investigate the effect on the optical and electrical performance of an n-i-p μc-Si:H solar cell, as a result of integrating plasmonic nanostructures near the back mirror.

1.3 Structure of the Thesis

This thesis aims to develop an efficient light-scattering system for the enhancement of optical absorption in μc-Si:H solar cells. In Chapter 2, a review on the fundamental principles of localised surface plasmons is presented. This includes a review of theory and recent research on the optical behaviour of metal nanoparticles. Chapter 3 includes a critical review on recent advancements in using plasmonics for light-trapping in μc-Si:H solar cells. The first part of Chapter 4 includes Mie simulation results on the optical behaviour of metal nanoparticles as reviewed in Chapter 2. The latter part of Chapter 4 introduces the design rules for the numerical finite-difference time-domain (FDTD) method to be used for simulating the optical properties of metal nanoparticles and plasmonic structures throughout this work. Chapter 5 presents an experimental investigation of a plasmonic scattering system with metal islands near a planar mirror. The first part of Chapter 6 presents FDTD simulation results to understand the influence of separation distance on the optical scattering by a single metal particle near a planar mirror. Important conclusions are derived relating the driving field intensity to the scattering by the plasmonic particle. The latter part of Chapter 6 includes an experimental investigation and optimisation of light-scattering by e-beam lithography (EBL) defined metal nanodiscs near a mirror. In Chapter 7, the EBL defined plasmonic mirror is integrated into a μc-Si:H solar cell. This Chapter also presents experimental results and detailed analyses on the optical and electrical properties of the fabricated plasmonic solar cell. Chapter 8 includes a discussion of the important contributions of this work to recent advancements in plasmonic μc-Si:H solar cells – this includes a comparison with research results by different groups, summarised in the review in Chapter 3. The latter part of Chapter 8 presents the main conclusions and suggestions for future work.

[This page intentionally left blank]

Chapter 2

Fundamentals of Plasmonics

2.1 Introduction

Localised surface plasmons (LSPs) are excitations caused due to charge density in a conductive nanostructure, oscillating in resonance to a coupled electromagnetic field [31]. Upon illumination by light and consequent interaction with the oscillating electric field, the electron cloud on the surface of the nanostructure is displaced as shown in Figure 2.1 [31]. A restoring Coulomb force between the displaced electron cloud and the nuclei of the nanostructure causes the coherent and resonant oscillation of the electron cloud, thereby resulting in LSPs. The coupling of incident photons to the LSPs results in enhanced local electric fields.

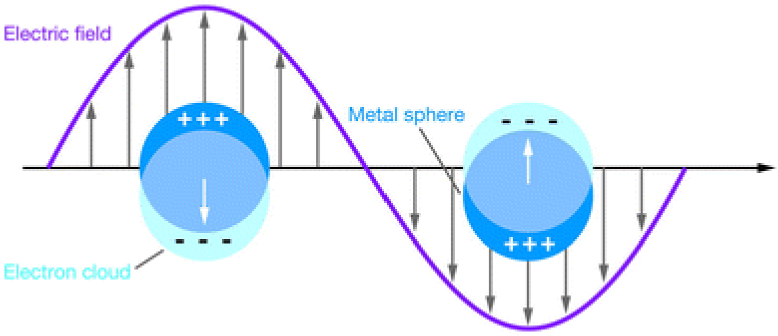

Figure 2.1: Excitation of localised surface plasmons on a metal nanosphere in an electric field [31].

Excited LSPs decay radiatively and non-radiatively. Radiative decay results in photon re-radiation and this process is known as scattering of the exciting electromagnetic wave. Non-radiative decay, due to photon absorption, can result in electron-hole pairs created via intraband or interband transitions. Intraband transitions occur within the conduction bands whereas interband transitions occur as a result of electron transition from d-bands to sp-conduction bands [31]. Noble metals such as Au and Ag, widely used in plasmonic applications exhibit interband transitions at specific regions in the electromagnetic spectrum [32]. Extinction, defined as the sum of scattering and absorption, indicates the decrease in optical transmission of incident light due to excitation of LSPs.

Propagating surface plasmons (PSPs) are another type of surface plasmon excitation which occur at the interface between a dielectric and a planar conductive surface[5]. PSPs differ from LSPs, in that they cannot be directly excited by incident photons. There has to be a momentum or 'energy' matching between incident photons and the PSPs and this can be achieved using complex structures such as prism or grating couplers [33, 34]. To date, PSPs have been widely used in sensor-based applications [34]. In terms of photovoltaic applications, recent studies have demonstrated optical absorption enhancement in thin solar cells as a result of coupling between PSPs excited in a patterned metal back contact and photonic modes in the absorber layer of the cell [28]. However, due to the need for complex device designs for excitation of PSPs, the potential of PSPs for photovoltaic applications is currently limited. In this work, we will focus only on LSPs and their use for light-scattering applications in photovoltaic devices.

In the first part of this Chapter, we will review analytical theories which predict the optical behaviour of an illuminated dielectric sphere in a homogenous medium. Next, we will review the effect of surrounding medium, nanoparticle size, shape and metal type on the plasmonic properties of a nanoparticle. This will also include a brief review of recent research on the fundamentals of plasmonics.

2.2 Dipole Approximation Theory

For a conductive nanosphere with a radius, r , much smaller than the wavelength, λ , of incident light, the electric field observed across the surface of the sphere will have constant phase and hence can be considered to be (quasi-) static. The incident static electric field, $\mathbf{E}_\mathrm{i}$, will induce a dipole moment inside the conductive sphere. If κ_s is the

---

[5] Another term commonly used in literature for propagating surface plasmons (PSPs) is propagating surface plasmon polaritons (SPPs).

complex dielectric constant[6] of the nanosphere (which if dependent on frequency is $\kappa_s(\omega)$), and κ_m is the dielectric constant of the surrounding non-absorbing isotropic medium, then the induced dipole moment **P** and polarizability α of the sphere can be defined as [35, 31]

$$\mathbf{P} = \varepsilon_o \kappa_m \alpha \, \mathbf{E}_i \qquad \textbf{(1)}$$

$$\alpha = 4\pi r^3 \frac{\kappa_s - \kappa_m}{\kappa_s + 2\kappa_m} \qquad \textbf{(2)}$$

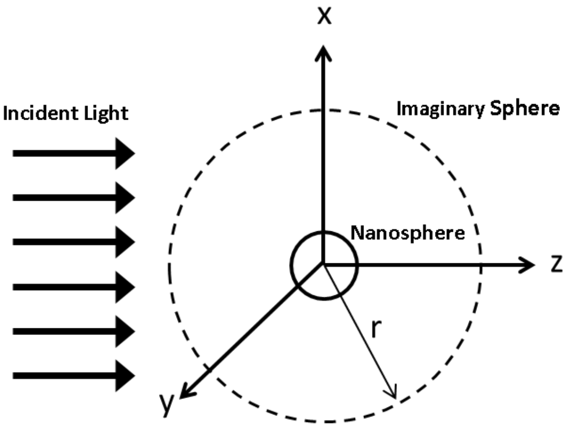

Figure 2.2: Extinction by an illuminated nanosphere: An imaginary sphere of radius 'r' is drawn concentric to the nanosphere. W_s is the net rate at which scattered energy crosses the boundary of the imaginary sphere. The rate at which energy is absorbed by the nanosphere, W_a, is the decrease in the rate of incident and scattered fields crossing the boundary of the imaginary sphere [adapted from [32]].

As shown in Figure 2.2, if an imaginary sphere of arbitrary radius (valid for a non-absorbing medium) is drawn concentric to the nanosphere, with the nanosphere at the centre of the imaginary sphere, then W_s can be calculated as the net rate at which scattered energy crosses the boundary of the imaginary sphere. The rate at which energy is absorbed by the particle, W_a can be calculated as the decrease in the rate of incident and scattered fields crossing the boundary of the imaginary sphere – a detailed mathematical

---

[6] The dielectric constant κ, of a material, is defined as the ratio of the permittivity, ε of the material to the vacuum permittivity, ε_o, where $\varepsilon_o = 8.85 \times 10^{-12}\ \mathrm{Fm}^{-1}$.

derivation can be found in Bohren and Huffman [32]. Here we concentrate on the physical interpretation of the important results.

If I_i is the irradiance (power per unit area) of the incident light, then the scattering cross section, C_{scat}, absorption cross section, C_{abs} and extinction cross-section, C_{ext} are defined as:

$$C_{scat} = \frac{W_s}{I_i} = \frac{k^4}{6\pi}|\alpha|^2 = \frac{8\pi}{3}k^4r^6\left|\frac{\kappa_s - \kappa_m}{\kappa_s + 2\kappa_m}\right|^2 \qquad (\mathbf{3})$$

$$C_{abs} = \frac{W_a}{I_i} = k\,\mathrm{Im}\{\alpha\} = 4\pi k r^3 \mathrm{Im}\left\{\frac{\kappa_s - \kappa_m}{\kappa_s + 2\kappa_m}\right\} \qquad (\mathbf{4})$$

$$C_{ext} = C_{scat} + C_{abs} \qquad (\mathbf{5})$$

Where k is the wave number defined as, $k = \frac{2\pi}{\lambda}$, where λ is wavelength of the incident light in the surrounding medium. Based on equations 1-5, we can derive important conclusions about the optical behaviour of a metal nanosphere in a (quasi-static) electric field.

With reference to (2), a resonant condition in the polarizability α occurs when $|\kappa_s + 2\kappa_m|$ is a minimum. Metals satisfy the requirement of a negative real component for κ_s, and hence, the resonance condition for $\kappa_s + 2\kappa_m$ tending towards zero, can be met for metals. If the imaginary component of κ_s changes slowly or is small around the resonance, then the resonance condition can be simplified to

$$Re\{\kappa_s(\omega)\} = -2\kappa_m \qquad (\mathbf{6})$$

The frequency at which equation (6) is satisfied is termed the *dipolar surface plasmon resonance frequency.* Noble metals, in particular, such as Ag and Au satisfy the requirements of a slow-varying imaginary component and a large negative real component for κ_s at the resonance [36, 37]. Hence, the noble metals can be viewed as ideal candidates for plasmonic applications.

In equations (3) and (4), the C_{scat} and C_{abs} are shown to be dependent on the optical constants of the nanosphere, the surrounding dielectric medium and the radius of the nanosphere. Given that the volume of a sphere is proportional to the cube of its radius, C_{abs} is directly proportional to the volume of the sphere, whereas C_{scat} is proportional to the square of the volume. Hence, with increasing size, the sphere will scatter more light than it absorbs. Very small spheres, on the other hand, will be highly absorbing.

The dipole approximation cannot be applied for nanospheres with radius, $r >> \lambda$: in larger spheres, the phase of the electric field across the volume of the sphere is no longer constant. The limitations of the dipole approximation can be overcome by Mie theory which is an analytical solution of Maxwell's electromagnetic equations on the surface of a dielectric sphere [38]. Mie theory can be used to calculate the C_{scat}, C_{abs} and C_{ext} of an illuminated isotropic dielectric sphere of *any* size, embedded in (i.e. completely surrounded by) an infinite isotropic dielectric medium [32].

A detailed mathematical derivation of Mie theory is beyond the scope of this work. The interested reader can refer a comprehensive and detailed derivation of Mie theory in Bohren and Huffman [32]. For purposes of this work we will highlight the important aspects of Mie theory and aim to establish a physical interpretation of its main results, using [32] as the main reference for the important equations of this theory.

2.3 Mie Theory

The interaction of electromagnetic radiation with a metal sphere of any given size involves resolving three fields: the incident electric field ($\mathbf{E_i}$), the electric field inside the sphere ($\mathbf{E_j}$) and the scattered electric field ($\mathbf{E_s}$) which arises due to the scattering of electromagnetic radiation by resonant LSPs [32]. These three fields together influence the driving field ($\mathbf{E_d}$) which essentially 'drives' or influences the characteristics of the LSP resonance. A detailed discussion of the driving field is conducted in Chapter 6.

Mie theory uses vector spherical harmonics to express the incident, scattered and internal fields in spherical vector co-ordinates. Taking the particle centre as the origin of a spherical co-ordinate system, the incident plane electromagnetic wave, $\mathbf{E_i}$ is expressed as an infinite series expansion of using vector spherical harmonics as

$$\mathbf{E_i} = E_o \sum_{n=1}^{\infty} i^n \frac{2n+1}{n(n+1)} (\mathbf{M}_{o1n} - i\mathbf{N}_{e1n}) \qquad \textbf{(7)}$$

Where $\mathbf{E_i}$ is the incident electric field, E_o is a constant related to amplitude of the electric field and $\mathbf{M}_{o1n}$ and $\mathbf{N}_{e1n}$ are vector spherical harmonics [7] (i.e. solutions to vector wave equation [32], in spherical co-ordinates).

The expansion of the internal and scattered fields can also be done in vector spherical harmonics by imposing suitable boundary conditions at the surface of the sphere: the interface between the sphere and the surrounding dielectric medium [32]. The next step in Mie theory is to derive expressions for the scattering, absorption and extinction cross-sections. If we consider *r* as the radius of the nanosphere with complex refractive index N_s embedded in a dielectric medium with refractive index N_m, we can define the following dimensionless parameters [32]

$$m = \frac{N_s}{N_m} \text{ and } \quad x = kr, \qquad (\mathbf{8})$$

where k is wave number, $k = \frac{2\pi}{\lambda}$, and λ is wavelength of the incident light in the surrounding medium. The extinction, scattering and absorption cross-sections are given by the formulae:

$$C_{ext} = \frac{W_{ext}}{I_i} = \frac{2\pi}{k^2}\sum_{n=1}^{\infty}(2n+1)\,\mathrm{Re}\{a_n + b_n\} \qquad (\mathbf{9})$$

$$C_{scat} = \frac{W_S}{I_i} = \frac{2\pi}{k^2}\sum_{n=1}^{\infty}(2n+1)(|a_n|^2 + |b_n|^2). \qquad (\mathbf{10})$$

Where W_s and I_i have the same definitions as in equations **(3)** and **(4).** W_{ext} is the net rate of extinction of the electromagnetic energy, and hence C_{abs} can be expressed as:

$$C_{abs} = C_{ext} - C_{scat} \qquad (\mathbf{11})$$

---

[7] Note that we have used Equation (7) to merely illustrate the important step in Mie theory which is to express the incident field in vector spherical harmonics. The equation is a result of an extensive complicated mathematical derivation in [32]; as a mathematical derivation is beyond the scope of this work, the interested reader can refer to the same, in order to realise the mathematical significance of the subscripts for vector harmonics: **M** and **N** in equation (7).

Where a_n and b_n are the scattering coefficients expressed as:

$$a_n = \frac{m\psi_n(mx)\psi_n'(x) - \psi_n(x)\psi_n'(mx)}{m\psi_n(mx)\xi_n'(x) - \xi_n(x)\psi_n'(mx)} \qquad \textbf{(12)}$$

$$b_n = \frac{\psi_n(mx)\psi_n'(x) - m\psi_n(x)\psi_n'(mx)}{\psi_n(mx)\xi_n'(x) - m\xi_n(x)\psi_n'(mx)} \qquad \textbf{(13)}$$

Where m and x are the dimensionless parameters defined in **(8)**. $\Psi_n(z)$ and $\xi_n(z)$ are the Ricatti-Bessel functions of order n. The primes represent differentiation. The main physical significance of the above result is that the summation index n denotes the order of the harmonic and hence the order of the multipole excitations or higher order modes, in the illuminated nanosphere. For instance, dipolar mode is denoted by n = 1, quadrupolar mode is denoted as n = 2 and octupolar mode is denoted by n = 3, *etc.* For $n = 1$, the corresponding solutions for C_{scat}, C_{abs}, C_{ext} are the same as the solutions obtained for the dipolar mode using dipole approximation theory. Although the series in **(10)** and **(11)** is infinite, the summation can be restricted to a few terms, $n = L$, as the influence of the higher order modes becomes negligible with increasing n; Bohren and Huffman propose the truncation order as: $L = kr + 4kr^{\frac{1}{3}} + 2$ [32]. As Mie theory is based on classical electromagnetics, it cannot be applied for nanospheres with diameter much smaller than 10nm due to the presence of quantum effects in this size regime [32, 36].

2.4 Optical Behaviour of Illuminated Nanoparticles

In this Section, we briefly review literature which demonstrates the effect of the surrounding dielectric environment, nanoparticle size and composition on the optical behaviour of an illuminated nanoparticle. As Mie theory can only be used to calculate the optical properties of a spherical nanoparticle (or an infinite cylinder), in sub-section 2.4.4.1, we review numerical methods used to determine the effect of the shape of a nanoparticle on its plasmonic behaviour.

2.4.1 Surrounding Dielectric Environment

The dipole approximation theory discussed in Section 2.2 already predicts the effect of the surrounding dielectric medium on the plasmonic resonance of a metal nanosphere. We will first briefly examine this theoretical prediction and then review some experimental results which confirm the effect predicted by theory.

In Equation 6, the real part of the frequency dependent dielectric constant, $\kappa_s(\omega)$ can be expressed as [31]

$$Re\{\kappa_s(\omega)\} = 1 - \frac{\omega_p^2\tau^2}{1+\omega^2\tau^2} \qquad \mathbf{(14)}$$

Where, ω_p is the bulk plasmon frequency, given by $\omega_p = (Nq/m_e\varepsilon_0)^2$, N is the free electron density, q is the electronic charge, m_e is the effective mass of the electrons and ε_0 is the vacuum permittivity. τ is the relaxation time of free electrons, with a value of approximately 10^{-14}s at room temperature [39]. We limit our discussion to frequencies, $\omega < \omega_p$ where metals retain their metallic character; as ω tends to ω_p, the product $\omega\tau \gg 1$. It must be noted that Equation 14 does not account for the interband transition effects in noble metals. Nevertheless, we have included this equation to merely get an idea of the effect of the surrounding dielectric constant on plasmonic resonance of ideal metal nanoparticles. Inserting Equation 14 into Equation 6, we see that plasmonic resonance frequency, ω is predicted to decrease with increasing dielectric constant κ_m (and hence, refractive index) of the surrounding medium.

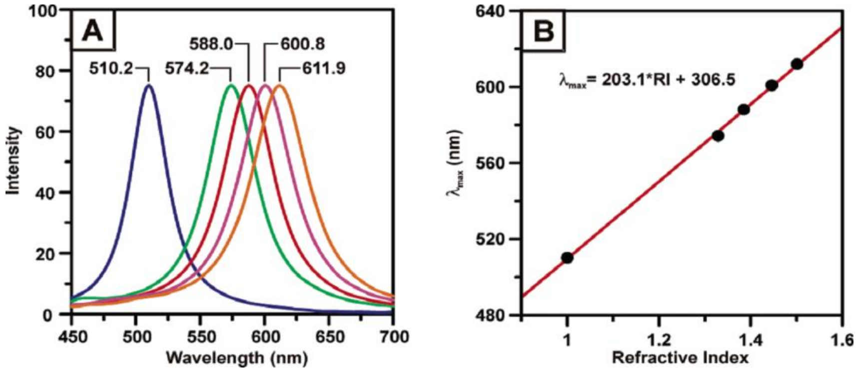

Figure 2.3: Single Ag nanoparticle scattering spectra in various solvent environments [40].

In an early experiment by Underwood and Mulvaney, aqueous Au sols with nanoparticles of approximately 16nm diameter, were transferred into organic solvent mixtures with varying refractive indices [41]. The colour of the Au sols is shown to be dependent on the refractive index of the surrounding medium, with the surface plasmon resonance wavelength depicting a red-shift with the refractive index of the solvent. This observation confirms the earlier theoretical prediction of a decrease in plasmonic resonance frequency (hence, increase in the resonance wavelength) with an increase in the refractive index of the surrounding medium. A similar study has recently been conducted by McFarland and Van Duyne, on the scattering spectra of single Ag particles immersed in solvents with varying refractive indices [40]. Figure 2.3 shows the results of this study, which indicate a clear linear relationship between the solvent refractive index and the spectral position of the plasmonic resonance.

2.4.2 Size of the Nanoparticle

The effect of the size of a metal nanosphere on its plasmonic resonance has been extensively reviewed by Kreibig and Vollmer [36]. The study indicates that there are two types of size-effects: intrinsic and extrinsic. Intrinsic size effects are valid for nanospheres with radii less than 10nm, where quantum-mechanical methods come into play (thereby making Mie-theory invalid in this size range) and the optical functions of the nanosphere, i.e. even the dielectric constant, vary as a function of the particle size. For a nanosphere with radius larger than 10nm, the optical functions can be assumed to be constant with size and the dependence of its plasmonic properties on size is termed as extrinsic. In this case, Mie theory based on classical electromagnetics can be applied to predict the optical behaviour of the nanoparticle. In Chapter 4 of this work, we use Mie theory simulation results to demonstrate an increase in the bandwidth and wavelength of the plasmonic resonance with the size of a metal nanosphere. Radiative damping, which results in the emission of photons, also increases with the size of a plasmonic nanoparticle [31]. Maier offers an interesting intuitive explanation to the red-shift of plasmonic resonance with the size of the nanoparticle [31]: referring to Figure 2.1, we see that that there is a restoring Coulomb force between the charges at opposite interfaces of an illuminated metal nanoparticle. Maier explains that as the size of the nanoparticle increases, the distance between the charges at opposite interfaces also increases thereby resulting in a weakening of the restoring Coulomb force. The weakening of the restoring force is depicted in the resonance spectrum, as a lowering of the resonance frequency (i.e. red-shift in the resonance wavelength) with nanoparticle size.

2.4.3 Composition of the Nanoparticle

For a given application, design specifications such as spectral range of interest: UV, visible or NIR, the required dominant process: radiative or non-radiative decay etc. play an important role in choosing the composition of the nanoparticle. For example, in thin Si solar cells which use light-trapping mechanisms, the plasmonic nanoparticle should efficiently scatter light (radiative decay) in the visible-NIR spectral range [28]. On the other hand, in applications such as plasmonics for photothermal cancer therapy [29], the nanoparticle should be optimised to act as a 'nanoheater' via efficient non-radiative decay processes in the NIR spectral range. In Section 2.2 it has already been highlighted that for plasmonic applications, the κ_s of the nanosphere needs to exhibit a large negative real component. It is clear from Equation 14 that this requirement is satisfied if ω_p, the plasma frequency, is significantly larger than ω, the required frequency, of application [37].

Metal	ω_p (eV)	$\lambda_p(nm)$	ω_{int}(eV)	λ_{int}(nm)
Ag	9.20	135	3.90	318
Au	8.90	139	2.30	539
Cu	8.70	143	2.10	590
Al	12.7	97.6	1.41	879

Table 1: Calculated values of plasma frequency ω_p (and corresponding wavelength λ_p) and frequency of onset for interband transition, ω_{int} (and corresponding wavelength λ_{int}) for commonly used metals in plasmonic applications, as calculated using Drude model parameters. [adapted from [37]].

Table 1 lists the plasma frequency, ω_p (and wavelength λ_p) for the commonly used metals in plasmonic applications. In light of the above discussions, it can be seen that of the four metals, Al is best suited for deep-UV applications as it has a highest value of 12.7eV for its plasma frequency. Table 1 also lists the frequency, ω_{int} (and wavelength, λ_{int}) at which the interband transition region sets in for the four metals. As described earlier, interband transitions contribute to non-radiative decay through the generation of electron-hole pairs when electrons are promoted to higher energy levels due to absorption of incident photons [31, 37]. At frequencies larger than ω_{int}, the metals lose their ideal metal (i.e. Drude metal) properties. In this work which will later concentrate on plasmonic scattering applications, interband transitions are a lossy, undesired mechanism. In Table 1, it is clear that Ag is the best material for visible to NIR applications as its interband transition wavelength, λ_{int} is in the UV range. While Au and Cu have interband transition regions in the visible range, Al has absorption losses in the NIR range. Hence it is clear as to why Ag and Au have been the most widely used metals for low-loss plasmonic applications in the visible-NIR spectral range.

Another reason for the decreased use of Al and Cu for practical applications is the ready formation of oxide layers on nanoparticles made of these metals. Langhammer *et al.*, experimentally demonstrated a red-shift in plasmonic resonance as a result of Al_2O_3 oxide formation on Al nanoparticles upon exposure to air [42]. Schatz *et al.*, demonstrated that if the CuO and Cu_2O layers which readily form on Cu nanoparticles upon exposure to air, are removed, then Cu can exhibit intense and narrow LSP resonance similar to Ag and Au [43].

Other studies have also explored the use of metals such as Pt and Pd for plasmonic applications [44]. However, in this case the metals exhibit continuous interband activity over the UV-visible-NIR spectrum resulting in weaker, damped plasmonic resonances in this spectral range [44].

Several experimental and simulation studies have also been conducted for the use of semiconductor materials such as ITO and GZO for near-infrared plasmonic applications [37]. The semiconductor materials need to be heavily doped in order to exhibit a large negative real κ_s component, and hence function as plasmonic materials in the desired frequency range. While the non-stoichiometric nature of oxides such as ITO, GZO, AZO allows for tuning of the optical properties during fabrication, heavy doping is not always found to work in favour of increased carrier concentration. Heavy doping of AZO for instance may lead to formation of $ZnAl_2O_4$ which only serves to limit carrier mobility rather than increase carrier concentration [45, 37].

2.4.4 Shape of the Nanoparticle

In Section 2.1, we noted that incident light polarizes a plasmonic nanoparticle. A change in the shape of the nanoparticle will affect the polarization of charge which in turn, will affect the optical properties such as absorption and scattering of light by the nanoparticle. Analytical techniques such as Mie theory can only be used to predict the optical properties for shapes such spheres, spheroids or infinite cylinders. The plasmonic properties of nanoparticles with complex shapes can be predicted using numerical methods such as discrete dipole approximation (DDA), finite-element method (FEM) and finite-difference time-domain (FDTD) method.

In the first part of this Section we will only briefly discuss the main concepts of the stated numerical simulation methods. For an extensive description of each method the interested reader may refer to a detailed review by Parsons *et al*. [46]. This work will primarily use the FDTD method for simulation of plasmonic particles using the ready software, Lumerical FDTD Solutions (v 8.7). Chapter 4 of this work will discuss the design principles required for this particular software-based implementation of the FDTD method.

2.4.4.1 Numerical Methods for Complex Shapes

In DDA, a nanoparticle of arbitrary shape is modelled as an array of N point dipoles on a cubic lattice [46, 47]. The period of the lattice is significantly smaller than the wavelength of the incident radiation, such that the dipole moment of every dipole in the lattice is due to the interaction between the incident field and the induced electric field from the neighbouring dipoles [47]. The solution of Maxwell equations is thereby reduced to an algebraic problem of coupled dipoles. The accuracy of the method (and computation time) depends on the spacing between the dipoles and the total number of dipoles [47].

In FEM, the arbitrary shape is discretised in space into a mesh of smaller tetrahedral regions. The electric and magnetic fields in each region are then described by a local function obtained by solving the Maxwell's equations in the frequency domain [48]. In this case, the accuracy of the simulation depends on the refinement of the meshed region, which in turn depends on the number of tetrahedral regions used to define the surface of the arbitrary shape [48].

FDTD is also a grid-based, iterative numerical solution to Maxwell's differential equations. In FDTD, the simulation region, which can contain an arbitrary shaped particle, is discretised in time and space in accordance to the Yee scheme [49]. The main concept of FDTD is to inject a plane wave source at an initial time and compute the new electric and magnetic field vector components in a discretised volume in space using field components calculated in the preceding time interval [49, 50, 51]. As a rigorous mathematical description of the FDTD computational algorithm is beyond the scope of this work, the interested reader may refer to other sources of literature, referenced in this paragraph. As FDTD solutions of electric and magnetic fields are evaluated in the time-domain, a Fourier transform of one simulation can be used to obtain broadband spectral results. This is particularly useful for simulations where it is important to trace the plasmonic resonance wavelength in the scattering spectrum and evaluate the broadband characteristics of the resonance peak.

2.4.4.2 Effect of Nanoparticle Shape on Plasmonic Properties

With the development of numerical simulation techniques, several extensive studies have been conducted on the analysis of plasmonic properties of particles with non-spherical shapes [44, 48, 53-55]. Wiley *et al*. use DDA simulations to clearly demonstrate the effect of particle shape on the plasmonic resonance [52, 53]. The results in Figure 2.4 show the simulated extinction, absorption and scattering spectra obtained using DDA simulations for 3D silver nanostructures. It can clearly be seen that in the cube the plasmonic peak is red-shifted when compared to the sphere. Wiley *et al*. attribute this observation to accumulation of charges in the corners; the increased separation of charges due to the presence of sharp corners, weakens the restoring Coulomb force which translates into a lowering of resonance frequency (and hence a red-shift in the resonance wavelength). Comparing the optical response of the cube to the sphere, it can be seen that the former has more resonance peaks. This is due to higher number of symmetries in the cube when compared to the sphere, which increases the number of ways for polarization in the former nanostructure.

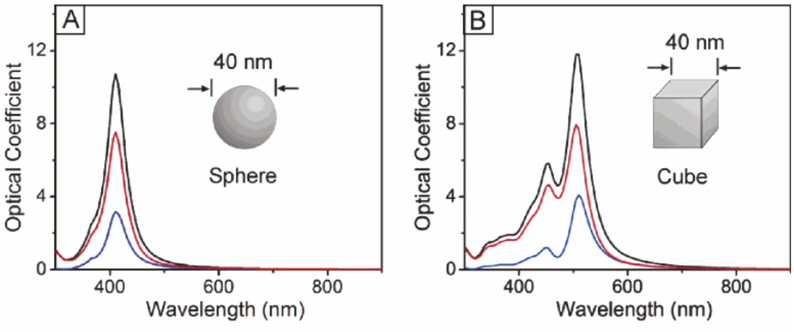

Figure 2.4: UV-Visible extinction (black), absorption (red) and scattering (blue) spectra of 3D Ag nanostructures: (a) sphere and (b) cube computed using DDA simulations [52].

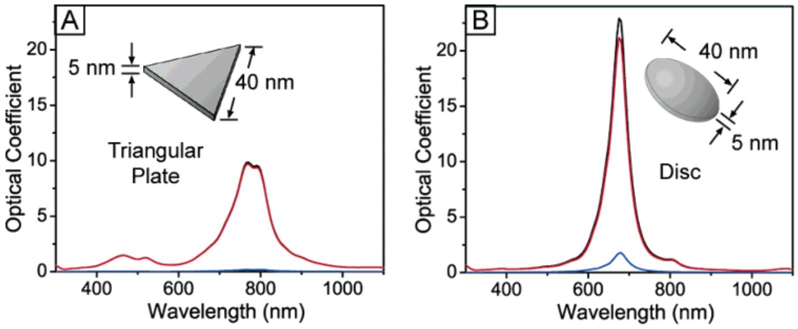

Figure 2.5: UV-Visible extinction (black), absorption (red) and scattering (blue) spectra of 2D Ag nanostructures (a) triangle and (b) disc computed using DDA simulations [52]

Figure 2.5 illustrates the optical properties simulated for 2D silver nanostructures. The resonance intensity exhibited by the disc is significantly higher when compared to the triangle. This is again due to the symmetry of the nanostructure. Unlike the charges in the triangle, the charges in the disc separate with mirror symmetry which increases the dipole moment and hence the resonance intensity [52].

Fabrication methods such as nanoimprint lithography [54], electron-beam lithography [55] and solution-phase synthesis [56] have allowed for the manipulation of the shape of nanoparticles. Several experimental studies utilising these techniques have shown how optical properties of non-spherical nanostructures can be selectively optimised for applications ranging from LSPR biosensors [57] to solar cells [28] to surface-enhanced Raman spectroscopy [58].

2.5 Conclusions

In this Chapter, we first reviewed the dipole approximation theory and Mie theory which dictate the optical behaviour of illuminated dielectric nanospheres in a homogenous medium. The dipole approximation theory is valid only for spheres with radii much smaller than the wavelength of incident light. Mie theory is valid for nanospheres of any size and successfully predicts the existence of higher order modes (i.e. multiple resonance excitations) in illuminated nanospheres with sizes much larger than the wavelength of incident light, using vector spherical harmonics. These theories dictate the expressions for the extinction, scattering and absorption cross-sections of an illuminated nanosphere.

Theoretical predictions indicate that the scattering cross section is directly proportional to the square of the volume of the sphere, whereas the absorption cross section is proportional to the volume of the sphere: hence, scattering to extinction ratio will increase with the size of the sphere. In the latter half of this Chapter we reviewed recent research results and relevant theory, on the effect of the surrounding medium, nanoparticle size, shape and metal type on the optical properties of the nanoparticle. The wavelength of plasmonic resonance increases with nanoparticle size and refractive index of the surrounding medium. Noble metals such as Ag, Au, Al and Cu, which have a large negative real component for their complex dielectric constant, support plasmonic resonances. Ag and Au are best suited for light-scattering applications in the NIR region as the lossy interband transitions occur outside this target wavelength range for both the metals. We then reviewed numerical techniques such as DDA, FEM and FDTD for simulation of nanoparticles with different shapes. A change in the shape will affect the polarization of charge and hence, will also influence the optical properties of the nanoparticle.

Chapter 3

Plasmonic Applications in Photovoltaics with a focus on Microcrystalline Silicon Solar Cells.

3.1 Introduction

There is recently an increased interest in using plasmonic nanoparticles for new applications such as: enhanced multicolour photodetection by graphene photodetectors [26], enhanced absorption in organic and inorganic photovoltaic devices [59, 60, 61], and high resolution bioimaging and biosensing [62]. As reviewed in Chapter 2, the plasmonic resonance can be spectrally tuned by modifying the size, shape and composition of the metal nanoparticle as well as the optical properties of the surrounding medium.

From an application perspective, a realistic medium maybe a multilayer structure with interfaces between materials of different refractive indices. The interference between incident and reflected light waves, at each interface of the multilayer structure, will influence the spectral characteristics of the electric field driving the plasmonic resonance. The separation distance between the plasmonic nanoparticle and the interface will determine whether the interference is destructive or constructive at a given wavelength. The consideration of interfaces is also of importance for photovoltaic applications as a solar cell is essentially an optical stack of materials with different refractive indices.

In this Chapter, we will first briefly review some pioneering studies on plasmonic scatterers near (multilayer) substrates. After highlighting the important results in these studies, we will discuss the recent advancements in plasmonic applications for thin film solar cells, particularly for µc-Si:H solar cells.

3.2 Plasmonic Nanoparticles near a Substrate

One of the most significant experiments of a particle near a substrate is the investigation by Drexhage into the radiative properties of a dye molecule near a planar metal [63]. Although Drexhage did not consider a metal nanoparticle, his experiment is significant because (i) A dipole approximation was implemented to explain the sensitivity of the radiative properties of the dye molecule to the distance from the metal substrate. The distance from the mirror can be used as a parametric probe to trace the interference, which is either constructive or destructive, between the reflected light and light incident onto the mirror. It is this interference effect that was shown to influence the radiative properties of the molecule. (ii) Empirical evidence was provided to demonstrate the optical coupling to evanescent PSP modes at small separations from the mirror. The implementation of the dipole approximation is of significance as metal nanoparticles with oscillating LSPs can also be approximated with an oscillating point dipole (subject to size constraints). Hence, the observations such as the sensitivity of the radiative properties of the molecule to the distance from the mirror and the coupling to the PSP mode on the metal are also applicable to plasmonic metal particles.

From a photovoltaics application perspective, the studies by Stuart and Hall demonstrated the first signs of the awareness of plasmonic applications. These first experiments in the late 1990s, instigated a plethora of numerical and empirical investigations into the area of plasmonic devices. The fact that researchers, even in the recent years, have derived numerical models to fit the results by Stuart and Hall [64, 65], nearly a decade after the publication of the authors' first paper, indicates the need for research in understanding the plasmonic mechanism of integrated random arrays of nanoparticles.

The first set of experiments with a plasmonic applications perspective, investigated the scattering properties of a random array of Ag islands near a mirror. The studies were conducted first, by Holland and Hall [66] and later by Stuart and Hall [67]. Thin Ag films were evaporated onto a substrate consisting of LiF layer on a Ag mirror. Ag islands are formed by thermally annealing the Ag films which agglomerate due to the surface tension of Ag [68]. In order to account for the enhancement in the scattering properties of the Ag islands near a mirror, Stuart and Hall suggest that the plasmonic activity in the Ag islands excites PSP modes in the mirror, and photonic modes in LiF spacer layer (for thickness in the order of 100nm). The authors argue that these modes in turn affect the interparticle interactions in the random array, and it is these substrate-mediated particle interactions that enhance the scattering.

However, we note here the quoted separation distances of the particles from the mirror, ranging from 40nm to 250nm. Even at a separation of 40nm, the authors fail to consider the decay length of the evanescent fields (LSP and PSP modes) and the propagation depth or dispersion profile into the LiF layer, of the apparently excited PSP modes. These characteristics are crucial in determining the degree of interaction between the excited surface modes and the particles and can be predicted with numerical solutions. Johansson numerically demonstrated that scattering enhancements observed for the array configuration considered by Stuart and Hall, were more likely due to the effect of the resultant driving field which is a consequence of interference effects in the multilayer substrate [64]. Johansson however also states that the PSP-LSP coupling effect proposed by Stuart and Hall is possible for periodic array configurations, as there is no wave-vector averaging in the latter configuration. The recent experimental results and numerical simulations, demonstrating LSP-PSP mode coupling between a periodic array of Au nanoparticles near an Au mirror, by Chu *et al.*, re-emphasise Johansson's statement [69].

Stuart and Hall also studied the optical characteristics of Ag islands on a silicon-on-insulator (SOI) waveguide structure [67, 27]. The Ag islands were separated from the SOI using a LiF spacer layer. In this first experiment (in 1996), the authors had reported absorption enhancements (and consequentially, photocurrent enhancements) due to the coupling of the incident light into waveguide modes, as a result of plasmonic scattering by the Ag islands [67]. In a subsequent paper studying the same structure in detail, the authors also stress that the observed absorption enhancement is due to surface-mode mediated interparticle coupling [27].

We note here, some inconsistencies in the magnitudes of the enhancement that the authors report in their two successive papers. In the first paper, the peak enhancement factor has a magnitude of 4, as seen in Figure 3.1b, for the waveguide with Ag islands. However, in their second paper (in 1998) [27], which implements Ag islands with very similar optical properties as the Ag islands in the first paper (comparing transmission spectra in Figures 3.1a and c), and the same waveguide configuration, the authors report an enhancement factor of 20, which is 5 times the previously quoted enhancement factor.

While it may be argued that the magnitude of enhancement is of little relevance as long as it depicts the spectral influence of the Ag islands, it must be pointed out that the magnitude is important in interpreting the optical mechanism for the enhancement. In

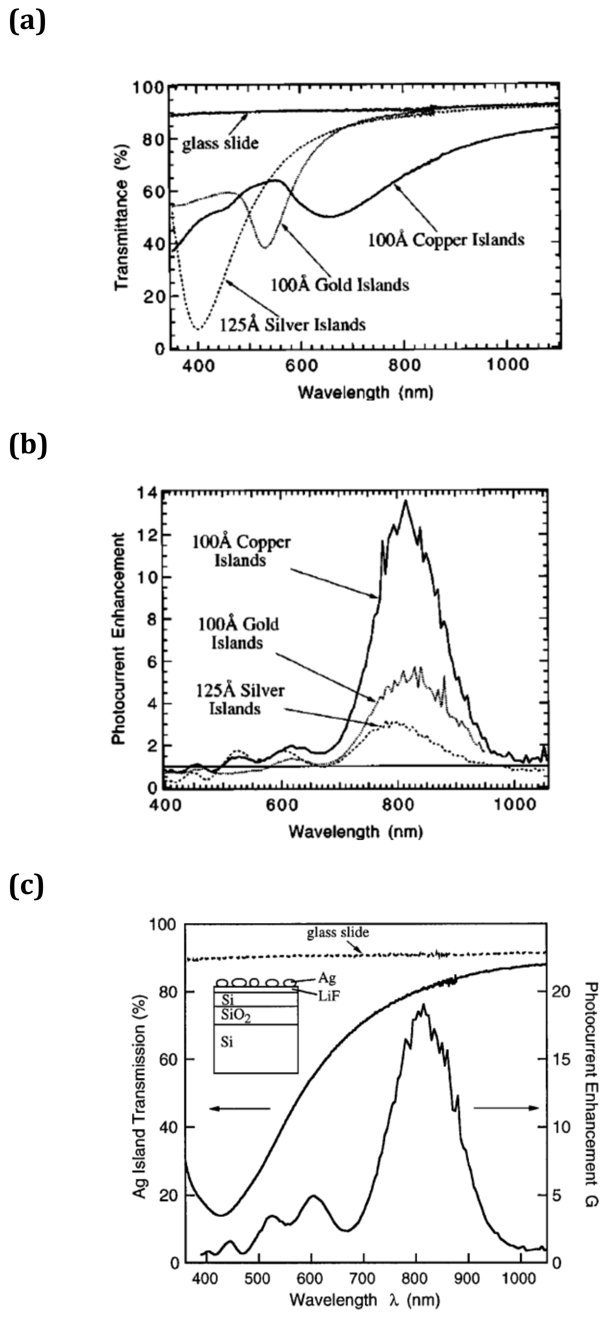

Figure 3.1: Inconsistencies in the waveguide enhancement results reported by Stuart and Hall in 1996 **(a, b)** and in 1998 **(c)** respectively. Note that the in the corresponding waveguide configuration for the spectra in **(a)** and **(b),** the Ag islands were separated from the waveguide by a 30nm LiF structure, as is the case with the configuration considered in **(c).** [67, 27]

fact, the authors argue in their first paper that since a perfect antireflective (AR) coating produces an enhancement of a factor of 4 at 800nm wavelength, the factor of 12 enhancement in the waveguide with Cu islands, must be due to coupling with the waveguide modes. However, the authors apparently fail to notice that the peak enhancement magnitude provided by the Ag islands is around a factor of 4 suggesting that the Ag islands could be functioning as an AR coating (or as scatterers) rather than coupling to the waveguide modes. If the apparent inconsistencies between the results of the 1996 and 1998 experiments are considered from a perspective of the above argument, then the authors' argument of a waveguide mediated dipole-dipole interaction is weakened.

In fact, Johansson numerically demonstrated, as in the case of particles near a mirror, that the absorption enhancement in the waveguide is due to direct influence of the driving field rather than the influence of the waveguide modes [64]. In a recent numerical model formulated by Catchpole *et al.*, the authors implement a single-dipole model (based on the Mertz model) to replicate the results of Stuart and Hall [65]. As Catchpole *et al.* consider a single-dipole model, they argue that the scattering enhancements depicted by Stuart and Hall's results are due to waveguide-mode coupling, but *not* due to surface mode-enhanced interparticle coupling.

In this Section, we have briefly reviewed pioneering studies in optoelectronic applications of plasmonic nanoparticles. Plasmonic nanoparticles near a substrate entail a wide range of optical phenomena such as scattering, coupling to photonic modes in a waveguide configuration (i.e. multilayer substrate) and coupling to PSP modes in a mirror. These observed effects are essentially different methods of energy transfer; the energy from the photon is transferred into the optical medium in the proximity of the plasmonic array. In photovoltaic (PV) devices, this mechanism of energy transfer can be used to increase the absorption efficiency of the absorber layer. Increased optical absorption efficiency should effectively translate into an increased electrical efficiency. In the following Section, we will review the application of plasmonic nanoparticles for light-trapping in μc-Si:H solar cells.

3.3 Plasmonic Light-Trapping in μc-Si:H Solar Cells

The need for light-trapping in μc-Si:H solar cells is outlined in detail in Chapter 1 of this work. If μc-Si:H solar cells are to approach the efficiency levels of c-Si solar cells, the single most important parameter that needs to be improved is the short circuit current density [8] (J_{sc}) [9]. Assuming that the photogenerated current density in a solar cell is equal to the J_{sc}, an increase in the J_{sc} is an indication of an increase in the optical absorption efficiency. Figure 3.2 shows the three different configurations for the integration of a plasmonic array into solar cells for light-trapping purposes. Although Figure 3.2 shows a periodic arrangement of plasmonic particles in the three configurations, it must be noted that the particles can also be assembled in a random arrangement. It is clear from the figure that different mechanisms of energy transfer can be exploited by placing the plasmonic array in different sections of the solar cell. In this Section, we will mainly review studies on randomly arranged nanoparticles for light-scattering in μc-Si:H solar cells, as this technique is the main focus of this work. One advantage of randomly arranged nanostructures is that they can be fabricated on a large-scale, commercial level, for example by using techniques such as thermal evaporation and annealing of thin films. In

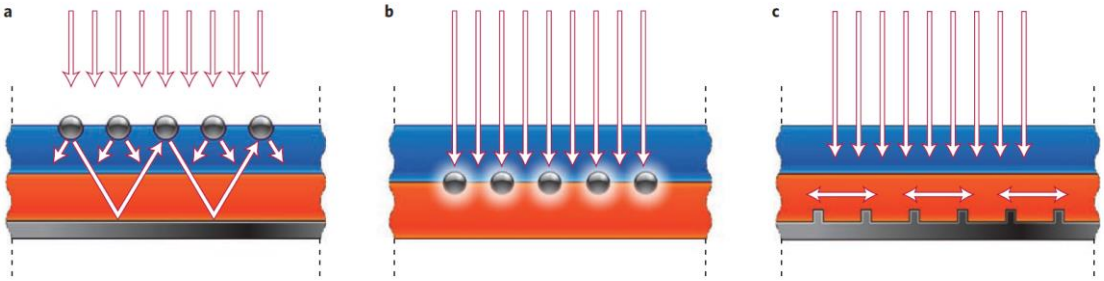

Figure 3.2: Three different configurations for plasmonic light-trapping in thin film solar cells. **(a)** Plasmonic particles on the front surface of the device: light-trapping is achieved by multiple high-angle scattering preferentially into the absorber layer. **(b)** Plasmonic particles embedded in the absorber layer: near-field enhancement in the plasmonic particles is used to create electron-hole pairs in the semiconductor layer. **(c)** Periodically spaced nanoscale metal patterns at the rear of the device used to couple to PSP or photonic modes propagating in the semiconductor layer [28].

---

[8] Short circuit current density is calculated by normalising the short circuit current to the area of the solar cell.

order to provide a complete overview of the advancements in plasmonic μc-Si:H solar cells, the latter part of this Section will also review the use of periodically arranged nanostructures for light-trapping.

3.3.1 Light-trapping by Randomly Arranged Nanostructures

Random arrays of Ag islands or colloids (Refer Figure 3.3) have been widely studied in attempts to increase the efficiency of thin film solar cells, by scattering light into high angles and trapping the light in the high refractive index absorber layer by total internal reflection [24, 70, 71]. For an array of scatterers on the front surface of a solar cell, Catchpole and Polman indicate that in addition to high-angle scattering, it is important that the array is configured to increase the preferential scattering of light into the substrate [72]. This is an important point to consider because total internal reflection (TIR) of light also entails multiple scattering events, every time the photons encounter the plasmonic array. If the plasmonic array does not preferentially scatter light into the substrate, then at every photon-array encounter, the photon may be scattered out of the substrate and an 'optical loss' occurs due to back scattering.

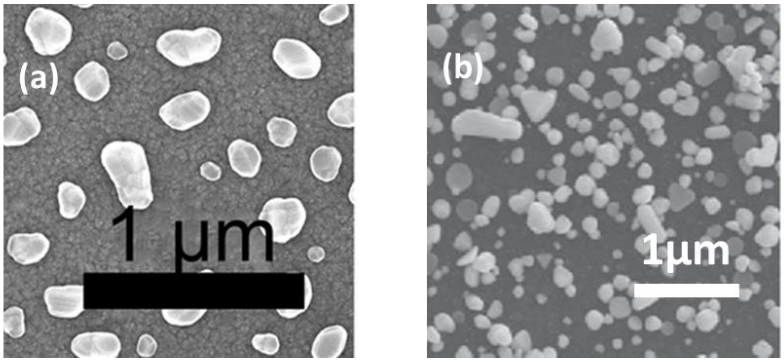

Figure 3.3 Random arrangement of metal nanostructures achieved by (a) Ag metal islands [24] (b) Ag colloids [70]

One method to overcome this loss due to back scattering is to position the array of scatterers at the rear of the solar cell. In this case, the design challenge of adjusting the back to forward scattering ratio is resolved. The photons will be back scattered into the absorber layer. The forward-scattered light can be manipulated by a mirror to reinforce the scattering mechanism of the plasmonic array. As the rear of a conventional solar cell incorporates a metal contact, this contact can influence the scattering of the plasmonic layer as in the case of a plasmonic array near a mirror (Refer Section 3.2). Another important advantage of integrating plasmonic arrays at the rear, as empirically demonstrated by Eminian *et al.*, is the avoidance of EQE (external quantum efficiency) losses due to parasitic short-wavelength photon absorption in the nanoparticles [73]. This is because in thin Si solar cells, the plasmonic array at the rear will target only the poorly absorbed NIR photons.

The EQE is a measurement of the ratio between the number of carriers collected by a device to the number of photons of a given wavelength incident on the device [74]. A brief explanation of the EQE measurement technique can be found in Appendix 3. A typical EQE spectrum is shown in Figure 3.4 – the details of the spectrum will be explained in the relevant part of the review concerning the study related to this result. For plasmonic light-scattering applications in μc-Si:H solar cell, authors also use an increase in the EQE in the NIR region (between 700-1100nm) as an indication of enhanced optical absorption by plasmonic scattering.

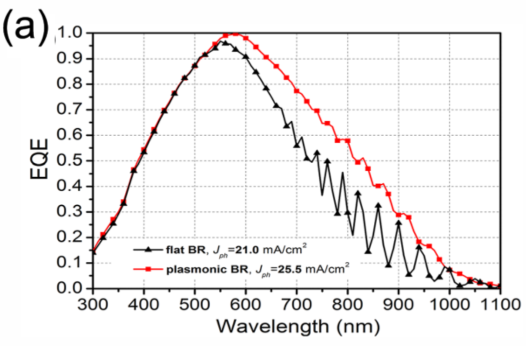

Figure 3.4: (a) EQE spectra for solar cell deposited on the plasmonic back mirror with 600nm Ag islands and for solar cell deposited on a flat Ag contact [24].

Tan *et al.* use a plasmonic mirror structure comprised of Ag islands (Figure 3.3a), at 20% surface coverage, near the back Ag contact of a n-i-p μc-Si:H solar cell [24]. They report an increase in the J_{sc} and EQE (NIR) (Figure 3.4) of the plasmonic device. The average diameter of the Ag islands is around 600nm and is larger (almost twice as large) than the typical size of metal islands used for light-scattering applications [68, 71, 23].

However, the authors argue that the large metal islands support higher-order modes[9] which enable high-angle scattering: a characteristic which is crucial for efficient TIR in the absorber layer [72]. As reviewed in Chapter 2, larger plasmonic nanostructures also tend to exhibit a higher scattering to extinction ratio (hence lower parasitic absorption losses) in the NIR region.

Tan *et al*. also highlight the importance of angular intensity distribution (AID) studies, by examining the AID of the plasmonic mirror structure (Ag islands/ZnO/Ag mirror) in air and comparing it to the AID of a Lambertian or randomly textured mirror which consists of random texturing. An ideal Lambertian mirror enhances the optical absorption of an absorber layer by $4n^2$ (n is the refractive index of the absorber layer) [75]. The AID in air, of the plasmonic back mirror developed by Tan *et al.*, exceeds that of the Lambertian distribution between 25^o to 55^o, at a resonance wavelength of 800nm. The authors seem to suggest that the broad-angular scattering characteristic of the mirror in air will also help with the increase in optical absorption efficiency when the mirror is integrated near the absorber layer of a solar cell. This assumption is most probably based on the preferential scattering by the mirror into a medium of higher-refractive index.

An important parameter that Tan *et al*. do not mention is the root-mean-square surface roughness (σ_{rms}) of the plasmonic mirror. It is difficult therefore to decide whether the observed light-scattering effect and the consequent increase in optical absorption is due to plasmonic light-scattering or due to light-scattering as a result of increased surface roughness – this question arises due to the high surface coverage (20%) of large (600nm) metal island films. In the light of this question, it is important to note that the spectral characteristics of the EQE of the plasmonic mirror are similar to that of a textured mirror (refer Figure 5 in [24]).

One important fact that Tan *et al*. mention is a decrease in the fill-factor (FF) of the plasmonic μc-Si:H device to 57.5% when compared to the FF value of 66.3%, for a device without the plasmonic nanostructures. In a solar cell, the FF value is affected by the series resistance (R_s), shunt resistance (R_{sh}) and recombination losses in the device [9]. Generally, it is desirable to have low R_s value and a high R_{sh} value for a solar cell with high FF; the best (non-plasmonic) μc-Si:H solar cells fabricated to date are quoted to have a FF

---

[9] Refer Chapter 2, Section 2.3 and Chapter 4, Section 4.2 for a detailed discussion and explanation of higher-order modes.

value between 70-77% [9]. An undesirable increase in the R_s value can be due to insufficiently doped p- or n- layers and highly resistive TCO layers. The R_{sh} value can be decreased due to cracks in the intrinsic μc-Si:H layer. Referring to the definition in the review in Chapter 1, Chopra *et al*. describe the thin film growth as an 'ab-initio' growth process, it must be noted that the type of substrate may dictate the quality of the μc-Si:H material grown/deposited onto it. For the plasmonic substrate developed by Tan *et al*., the surface morphology of the metal islands may be a reason for the observed decrease in the FF of the device as a result of a decrease in the quality of the μc-Si:H layer.

In fact, several authors have reported a decrease in FF and sometimes the open circuit voltage (V_{oc}), when using plasmonic metal islands in μc-Si:H solar cells [23, 24, 70]. A significant decrease in FF and V_{oc} will result in a decrease in the overall efficiency of the device, despite any increases observed in the J_{sc} due to enhanced optical absorption efficiency. Moulin *et al.*, who used Ag islands of size 300nm, near the back mirror of a n-i-p solar cell attributed a decrease in the FF to alteration (possibly decrease in material quality although authors are not specific) in μc-Si:H growth due to the presence of nanoparticles [23]. Mizuno *et al.* used Ag colloids (Figure 3.3b) near the mirror of a p-i-n structure [70]. In this configuration, the Ag colloids were deposited by wet-chemical procedure after the growth of the active layers. Hence, in this particular case, the authors attribute the decrease in the FF and V_{oc} values to the wet-chemical procedure affecting the quality of the active layer. Both the studies by Moulin *et al*. and Mizuno *et al*. show an increase in the J_{sc} value of the plasmonic device when compared to a device without the Ag nanostructures. Interestingly, Chantana *et al.*, also include Ag island films with an average diameter of 300nm, in a n-i-p device structure [71]: a configuration which is very similar to that implemented by Moulin *et al*. However, in this case, the authors mention the σ_{rms} of the plasmonic mirror to be as low as 16.5nm (conventional Asahi-U textured substrates have a σ_{rms} of 30nm [20]). The plasmonic device fabricated by Chantana *et al*. shows FF and V_{oc} values similar to that of a device fabricated on a rough textured substrate. The authors choose to use a device on a textured substrate as a reference cell, instead of a flat device without nanoparticles which is commonly used as the reference cell in other studies. The authors demonstrate that the plasmonic device outperforms the device on a conventional textured substrate by depicting a higher J_{sc} and conversion efficiency value.

The discrepancy in the results obtained by Chantana *et al*. and Moulin *et al.*, who use similar configurations for the plasmonic μc-Si:H solar cells, highlights the difficulty in comparing devices with randomly arranged metal islands. The islands, due to the thermal annealing procedure, have an irregular shape and size distribution. Hence, the σ_{rms} of such large irregular islands cannot be expected to be the same across different studies. A fair comparison of devices with integrated metal islands of similar sizes is therefore difficult due to the irregularity in the size and shape of these islands. The inability to control the size and shape distributions of metal islands is an important limitation in the fabrication process of evaporation and thermal annealing of metal films.

3.3.2 Light-trapping by Periodically Arranged Nanostructures

The optical absorption of the absorber layer can also be enhanced using a periodic arrangement of nanostructures or a periodic grating, as shown in Figures 3.2c and 3.5. A recent study by Paetzold *et al*. used a back mirror with periodically arranged 'half-ellipsoidal' Ag nanostructures with a diameter of 110nm (Figure 3.5b), in an n-i-p µc-Si:H solar cell [19]. The authors demonstrated an increase in the J_{sc} of the plasmonic device when compared to a device with a planar Ag back contact. As the pitch of the periodic nanostructures is on the order of the wavelength of incident light, the periodic arrangement serves to diffract the incoming light into discrete diffraction orders; given that there is a wave-vector matching between the diffracted order beam and the supported guided mode in the absorber layer, light is coupled into the waveguide modes of the absorber [33]. Paetzold *et al*. demonstrate that it is possible to tune the pitch of the

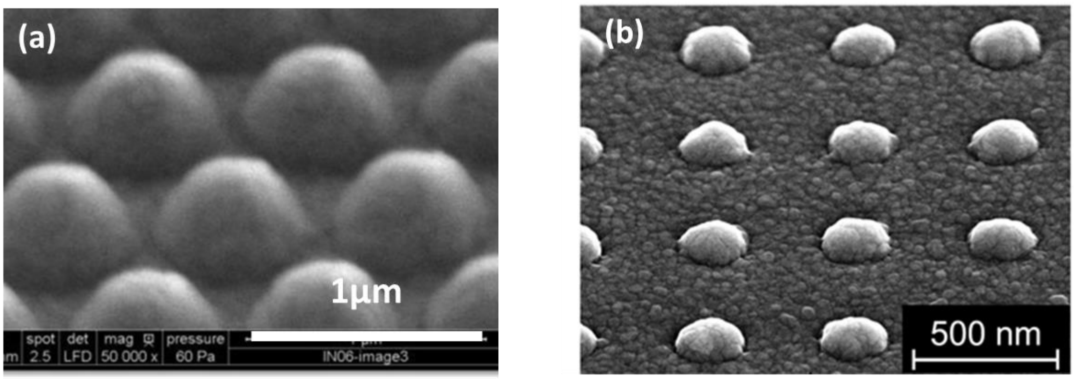

Figure 3.5 Periodic arrangement of metal nanostructures achieved by plasmonic-photonic grating structures; Figure (a) is obtained from [54] , and (b) is obtained from [19]

nanostructures to achieve a value of J_{sc} which is close to that of a device with a conventional randomly textured mirror. Bhattacharya *et al*. also use a periodically textured back mirror and successfully demonstrate an increase in the J_{sc} of the plasmonic n-i-p device [54]. A comparison of the nanostructures used by Paetzold *et al*. and Bhattacharya *et al*. indicates that both studies have used the 'half-ellipsoidal' nanostructure, with the nanostructures used by Bhattacharya *et al*. being almost 3 times the size of the nanostructures used by Paetzold *et al*. (c.f. Figures 3.5a and 3.5b). The authors in both studies fail to give a reason for the selection of the size of the nanostructures. Bhattacharya *et al*. also demonstrated that the device with the periodically arranged nanostructure has a higher J_{sc} than the device with a conventional random textured substrate. Both studies however fail to state the FF, V_{oc} and efficiency values of the plasmonic devices – as a result it is not possible to analyse the effect of the periodic structures on the electrical quality of the µc-Si:H absorber layer. Paetzold *et al*. for instance, state that the J_{sc} value is directly proportional to the efficiency of the device and hence an increase in J_{sc} should denote an increase in efficiency. However, this assumption fails to account for the plausible negative effect in FF and V_{oc} values which may occur due to the degradation of µc-Si:H layer being deposited on a textured substrate (refer discussion in Section 3.3.1)

3.3.3 Summary of Recent Results for Plasmonic µc-Si:H Solar Cells

In Sections 3.3.1 and 3.3.2, we reviewed the use of plasmonic nanostructures near a mirror, in a random as well as periodic arrangement, for purposes of light-trapping in µc-Si:H solar cells. In this Section, we will attempt to summarise the 'best' results obtained for µc-Si:H solar cells, using the different configurations of the plasmonic back mirror: mainly randomly arranged metal island films, colloidal nanoparticles and periodically arranged nanostructures. This comparison has been feasible as there are currently only a few studies, as reviewed in this Chapter, on plasmonic µc-Si:H solar cells, given that the development of µc-Si:H is still a topic of research. We will also include, for purposes of comparison, the results for a device fabricated on a conventional textured mirror.

A comparison of results is actually difficult as the studies on the different configurations of the plasmonic mirror use different parameters to justify an enhancement

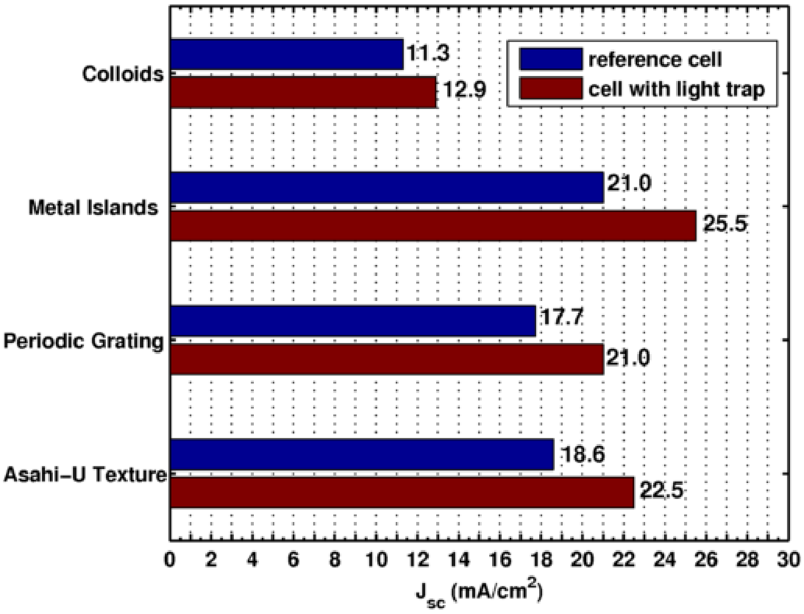

Figure 3.6: Summary of the results which represent the 'best' (highest) J_{sc} values for the plasmonic device with corresponding J_{sc} value for reference device, for different plasmonic back mirror configurations: colloids [70], Ag islands [24], periodic grating [19], and Asahi-U texture [18].

in the efficiency of the device. Ideally, it would be desirable for all studies to state the J_{sc}, FF, V_{oc} and efficiency values for the plasmonic device and a reference device, where the latter is usually a μc-Si:H solar cell fabricated on a flat metal contact. However, only few studies state all these measurements; most studies are limited to comparing the J_{sc} value of the plasmonic device to that of a reference device to indicate an enhancement in the optical efficiency. Hence, in Figure 3.6, based on a review of literature on random and periodically arranged nanostructures for light-trapping in μc-Si:H solar cells, we have summarised the results which represent the 'best' (highest) J_{sc} values for μc-Si:H solar cells with different plasmonic mirror configurations. The corresponding J_{sc} value of the reference device used in each study is also plotted to facilitate a fair comparison of the optical enhancement due to plasmonic light-trapping.

Based on Figure 3.6, the randomly arranged metal island films near a planar mirror, fabricated by Tan *et al.*, appear to show the highest increase in J_{sc} when compared to a flat reference cell. Also, the performance of the plasmonic device with the metal island films is comparable to that of the device on a conventional Asahi-U textured substrate. While there is a limited scope to the improvement in the conventional device, the plasmonic device with the randomly arranged metal islands can be further improved. The effect on the device performance as a result of varying the interparticle distance, the degree of uniformity in the nanoparticle size and shape distribution and varying the distance between the plasmonic layer and mirror needs to be investigated. In this work, we will aim to design and fabricate an efficient plasmonic back mirror structure with randomly arranged plasmonic nanoparticles to be integrated at the rear of an n-i-p μc-Si:H device. We will also aim to develop a fabrication procedure to obtain a regular distribution in the size and shape of the nanoparticles unlike the case of randomly arranged metal islands. In Chapter 8 of this work, we will compare the performance of our plasmonic device with the devices in Figure 3.6 in order to critically evaluate the contribution of this work to the advancements in plasmonic μc-Si:H solar cells, on an international research platform.

3.4 Conclusions

In this Chapter we reviewed the recent progress in plasmonic-light trapping applications for μc-Si:H solar cells. Plasmonic nanoparticles placed at the rear of solar cells can overcome losses due to back-scattering. The forward-scattered light can be reflected by the planar metal back contact in the solar cell to reinforce the plasmonic light-scattering mechanism. We observe that randomly arranged metal islands placed near the back mirror can be used for preferential, omnidirectional scattering of light into the absorber layer. The reviewed studies demonstrated an enhancement in the optical absorption efficiency of the μc-Si:H solar cell as a result of integration of metal islands; the enhancement is indicated by an increase in the J_{sc} value. Studies also demonstrate cases where the angular distribution intensity of the light scattered by metal islands exceeds that of a conventional Lambertian mirror over a specific angular range. However, these results are not reported in all studies, i.e. this observation is not consistent due to the irregularity in the shape and size of metal islands – a limitation in the fabrication procedure of thermal annealing of thin metal films. The surface morphology of the large (300-600nm) random metal islands may play a role in degrading the electrical quality of the μc-Si:H layer deposited onto them, especially in n-i-p type solar cells, thereby negatively affecting the FF, V_{oc} and efficiency values of the device. Hence, when designing a solar cell with an integrated plasmonic layer it is crucial to ensure that the enhanced optical efficiency offered by the plasmonic layer is not outweighed by the negative effects on electrical efficiency due to the integration of the layer. In the case of periodically arranged nanostructures, the pitch of the periodic array is designed to be on the order of the wavelength of incident light. This results in the diffraction and coupling of the incident light into waveguide modes of the absorber layer, resulting in light being 'trapped' in the absorber and a consequent increase in optical absorption efficiencies. The fabrication process for periodic gratings is more complicated (and yet to implemented on a large scale) when compared to the fabrication of random metal islands: the nanostructures in the former case need to have well-defined separation distances, sizes and shapes. This is usually achieved by electron-beam lithography or nanoimprint lithography. The studies on plasmonic-photonic grating structures indicated that the light-scattering and subsequent absorption enhancements obtained by these structures is comparable to, or better than that obtained by using a conventional randomly textured substrate.

[This page intentionally left blank]

Chapter 4

Mie Simulation Results and the FDTD Simulation Technique

4.1 Introduction

In order to analyse the plasmonic scattering by a metal nanoparticle, the electric and magnetic fields need to be resolved according to Maxwell's differential equations [32]. Mie theory is one method of solving Maxwell's equations to determine the optical scattering cross-section (C_{scat}) and absorption cross-section (C_{abs}) of a dielectric sphere in a homogenous medium (refer Chapter 2, Section 2.3 for definitions of C_{scat} and C_{abs}). Chapter 2 of this work presented a detailed review of Mie theory and the optical behaviour of an illuminated metal nanoparticle with respect to its size, refractive index of the surrounding medium and metal type. In the first part of this Chapter, we will present simulation results confirming the fundamental predictions by Mie theory for the optical properties of a metal nanosphere in a homogenous medium.

As explained in Chapter 2, Mie theory also has its limitations: it can only be applied for the simple geometry of a sphere in a homogenous medium. For plasmonic applications there may be a need to vary the shape of the nanoparticle and introduce substrates such as a mirror or even multilayer substrates in the case of solar cells. The limitations of the analytic Mie solutions can be overcome by implementing a numerical technique of solving Maxwell's equations. In this work we will primarily be using the numerical technique of finite-difference time-domain (FDTD) for the simulation of plasmonic particles. The latter part of this Chapter will discuss the design principles required for the implementation of the FDTD simulation method.

4.2 Mie Simulation Method

The Mie theory results in Section 4.3 were simulated using a Fortran implementation of Mie theory developed by Bohren and Huffman [32]. The aim of the program is to calculate the absorption and scattering by an isolated dielectric sphere in a homogenous medium.

The inputs to the program include the size of the sphere, the real refractive index of the surrounding medium and the complex refractive index for the dielectric material of the sphere. The optical constants data used for the Ag sphere in the simulations were obtained from tabulated results by Johnson and Christy [76]. While we have already defined the extinction, scattering and absorption cross-sections: C_{ext}, C_{scat} and C_{abs}, respectively, (refer Section 2.2 and 2.3 in Chapter 2), we now define the values, Q_{ext}, Q_{scat} and Q_{abs} which are the extinction, scattering and absorption efficiencies[10]. Q_{scat}, at a particular wavelength, is calculated as the ratio of the value of C_{scat} at that wavelength, to the geometrical cross-sectional area of the sphere. Q_{abs} is calculated in the same way using the value of C_{abs}. Q_{ext} is then defined as the sum of Q_{scat} and Q_{abs}.

The physical significance of the values of Q_{scat} and Q_{abs} is that they represent the target area presented to an incident photon by an illuminated nanoparticle for scattering and absorption, respectively [77]. For example, a Q_{scat} value of 3 indicates that the effective cross-sectional area for the scattering of light is 3 times larger than the actual geometrical cross-sectional area of the sphere.

4.3 Mie Simulation Results

4.3.1 Effect of Varying the Particle Size

Figure 4.1 (a-c) depict the general trend in Q_{ext}, Q_{scat} and Q_{abs} when the diameter of a Ag sphere is increased from 40nm to 400nm, in a medium of refractive index, n=1. A local maximum in the Q_{ext} spectrum indicates a plasmonic resonance. In Figure 4.1a, it can be seen that an increase in the size of the sphere firstly results in a decrease in the corresponding peak value of Q_{ext}. Secondly, particles with a larger diameter show additional long-wavelength peaks in the Q_{ext} spectra. If we examine the individual spectra of selected particles in Figure 4.1d, we can see that the plasmonic peak for a 40nm particle is narrow with a significantly high value of extinction, at a wavelength of approximately 350nm. When the size of the particle is increased to 160nm, there are two peaks in the

---

[10] Note that the conventional term 'efficiency' may not best describe these ratios as the value of Q_{scat}, Q_{abs} and Q_{ext} are not confined between 0 and 1 [77].

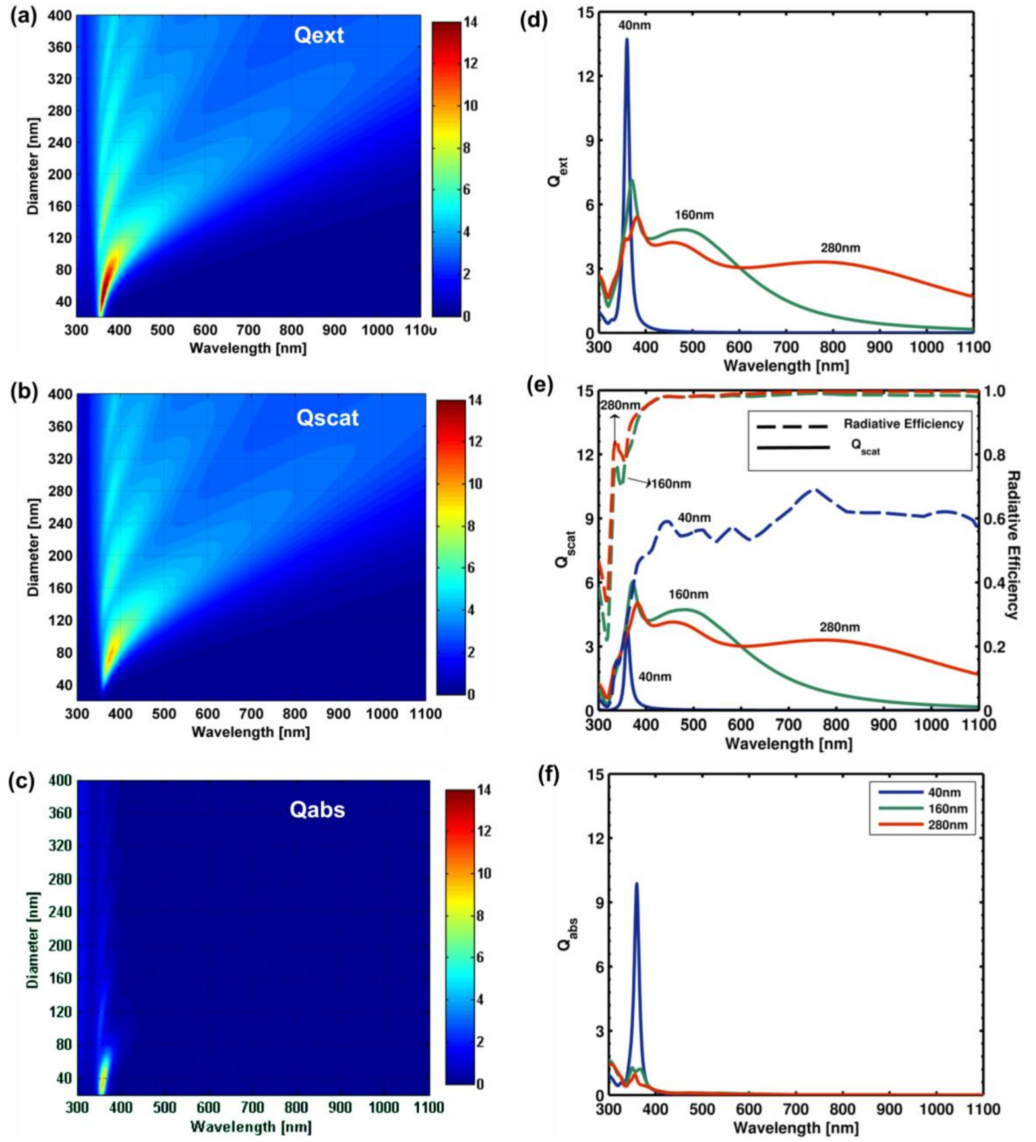

Figure 4.1 (a-c): Effect of varying the diameter of a Ag nanoparticle, from 40nm to 400nm on the Q_{ext}, Q_{scat} and Q_{abs} spectra. **(d-f):** Detailed spectral characteristics of the Q_{ext}, Q_{scat} and Q_{abs} spectra for Ag nanoparticle of sizes: 40nm, 160nm and 280nm. Figure 4e also illustrates the calculated radiative efficiencies for the selected particle diameters. The surrounding medium has a refractive index, n = 1.

corresponding Q_{ext} spectrum: a peak in the short-wavelength range near 400nm and a broader, asymmetric peak at a wavelength of 500nm. Both the peaks have relatively smaller magnitudes than the peak value of Q_{ext} for the 40nm Ag sphere. The presence of multiple resonance peaks with an increase in the size of the particle is due to the excitation of higher order modes. Higher order modes were discussed from a theoretical

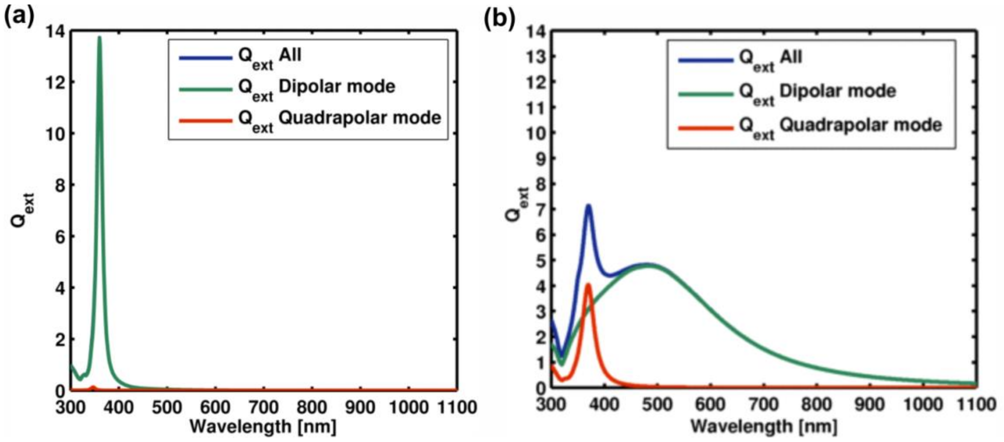

Figure 4.2: Mie simulation results for higher order modes in the Q_{ext} spectrum for a Ag nanoparticle of diameter **(a)** 40nm and **(b)** 160nm, surrounded by a medium of refractive index, n = 1.

perspective in Chapter 2. They occur due to the non-uniform distribution of the electric field across a particle with a size on the order of the wavelength of incident light. Further, based on the literature review on plasmonic applications of nanoparticles in Chapter 3, the higher order modes are also useful for high-angle scattering of light [24]. Figure 4.2b shows the excitation of the quadrupolar mode and dipolar mode in the Q_{ext} spectra of the 160nm Ag particle. It is the dipolar mode which red-shifts with an increase in particle size. As seen in Figure 4.2a, there is barely any excitation of higher order modes in the 40nm Ag particle as the electric field across the particle is uniform.

It is visually evident from Figure 4.1 (a-c) that as the size of the particle is increased, it scatters more efficiently than it absorbs. The radiative efficiency of a nanoparticle is defined as the ratio of Q_{scat} to Q_{ext} and is a measure of the strength of scattering by the nanoparticle. In Figure 4e, it can be seen that the radiative efficiency of the larger particles, with radii 160nm and 280nm approaches a value of 1 for wavelengths beyond 450nm: almost all the light that is incident on these particles is scattered with minimal absorption. The radiative efficiency for the 40nm particle averages to a value of 0.6 in the visible to NIR range[11].

---

[11] The irregular radiative efficiency spectrum of the 40nm particle is result of the calculation with fluctuating, near-to-zero values of Q_{scat} and Q_{ext} in the 400nm to 1100nm wavelength range.

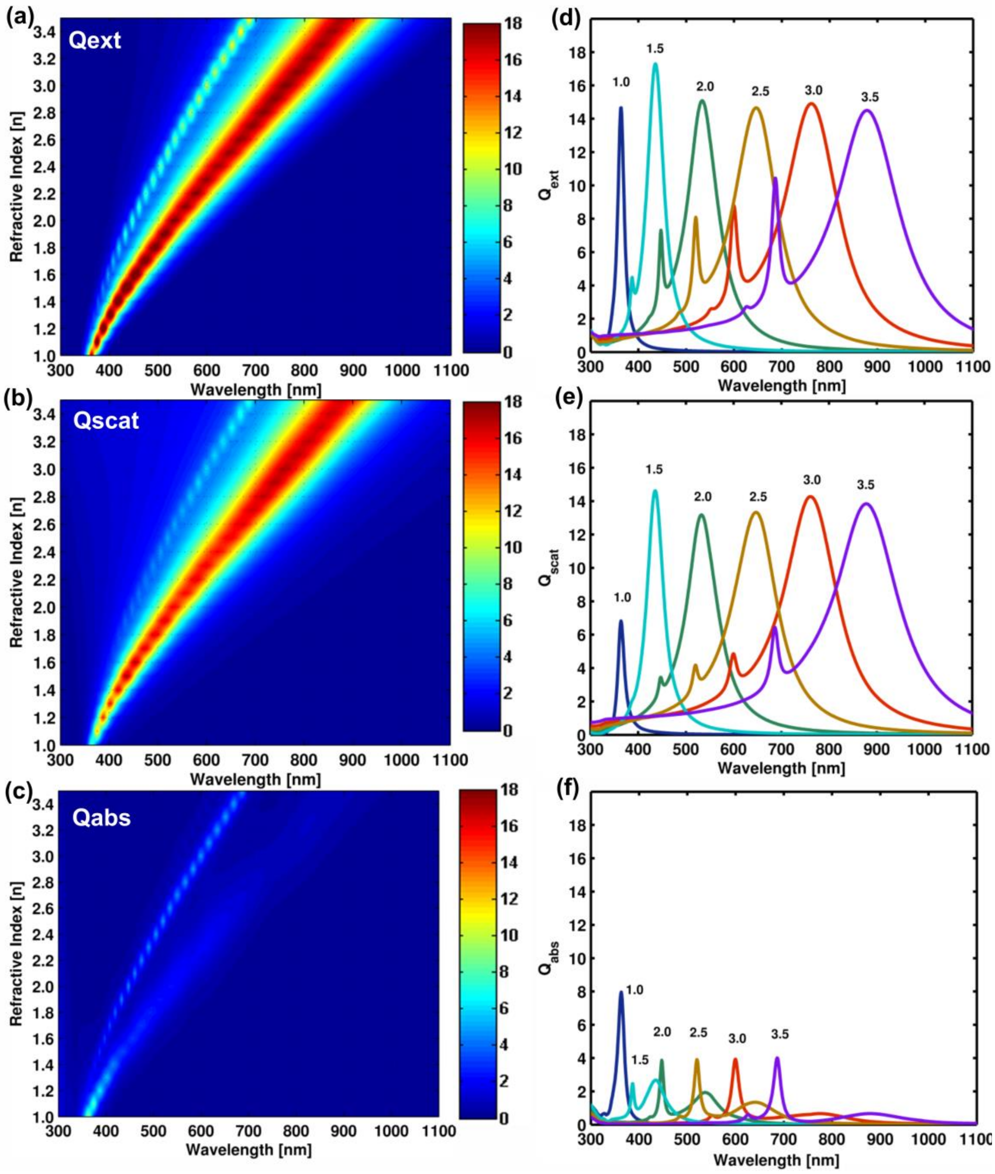

Figure 4.3 (a-c): Effect of varying the refractive index of the surrounding medium from 1.0 to 3.4 on the Q_{ext}, Q_{scat} and Q_{abs} spectra of a Ag nanosphere **(d-f):** Detailed spectral characteristics of the Q_{ext}, Q_{scat} and Q_{abs} spectra for a Ag nanosphere for surrounding medium with selected refractive indices. The Ag nanosphere has a diameter of 50nm.

Hence, Mie simulation results confirm that an increase in the particle size is accompanied with a decrease in the peak extinction magnitude. The radiative efficiency and the wavelength of the plasmonic dipolar resonance increase with particle size. Particles with diameters in the order of 100nm of incident light exhibit multiple resonances due to the excitation of higher order modes.

4.3.2 Effect of Varying the Refractive Index of the Surrounding Medium

Figure 4.3 (a-c) illustrate the general trend in the Q_{ext}, Q_{scat} and Q_{abs} spectra when the refractive index of the medium surrounding a Ag nanosphere of diameter 50nm, is varied from a value of n=1.0 to n=3.4. Firstly, it can be observed that the plasmonic resonance red-shifts and broadens with the refractive index of the surrounding medium. Secondly, the peak magnitude of Q_{ext}, Q_{scat} and Q_{abs} does not significantly change with an increase in the refractive index. The individual Q_{ext}, Q_{scat} and Q_{abs} spectra for selected refractive indices in Figure 4.3 (d-f) confirm these two observations. A closer examination of the Q_{ext} spectra in Figure 4.3d shows the emergence of a 'shoulder' peak at a lower wavelength when compared to the dominant plasmonic peak; the shoulder peak emerges for refractive index values greater than 1. This shoulder-peak exhibits a gradual increase in its magnitude and also red-shifts with increasing refractive index. The corresponding Q_{abs} spectra in Figure 4.3f indicate that while the Q_{abs} value of the dominant peak decreases with refractive index, the Q_{abs} value of the shoulder-peak is fairly constant and higher than the Q_{abs} value of the dominant peak, irrespective of the increase in the refractive index.

4.3.3 Effect of Varying the Metal Type

Figure 4.4 shows the radiative efficiency (Q_{scat}/Q_{ext}) for a nanosphere of size 100nm and metal types: Ag, Au, Al and Cu, in a medium of refractive index, n = 1. As this work focuses mainly on plasmonic scattering applications, we choose to examine the simulation results for radiative efficiency. It can be seen that the Ag nanosphere has the maximum radiative efficiency in the visible to NIR wavelength region. The broadband radiative efficiency of the Au nanosphere is lower than that of the Ag sphere with a significant dip around a wavelength of 500nm. The Cu and Al nanosphere also exhibit a lowering of the radiative efficiency around 590nm and 880nm, respectively. The wavelengths at which the trough

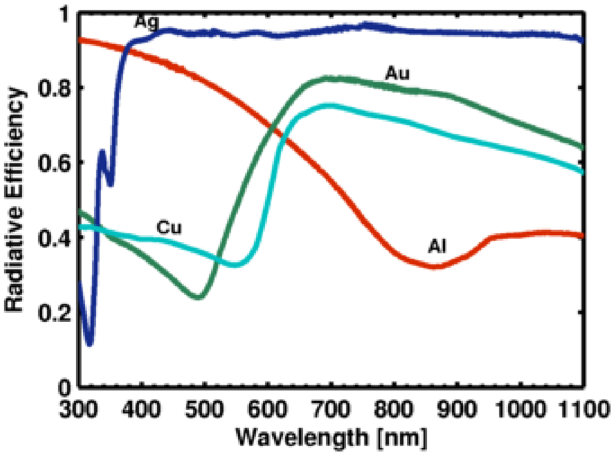

Figure 4.4: Simulated radiative efficiency spectra (based on Mie theory) for a nanosphere of diameter 100nm and metal types: Ag, Au, Al and Cu. The refractive index of the surrounding medium: n =1.

in radiative efficiency occurs for Au, Cu and Al coincide with the wavelengths for the onset of the interband transitions in these metals. As already explained in Section 2.4.3, interband transitions in a metal are non-radiative mechanisms which are undesirable for scattering applications. Hence, the Mie simulation results in Figure 4.4 confirm that Ag is the most suitable metal type for plasmonic scattering applications in the visible to NIR region; the lossy interband transition in Ag occurs in the deep-UV region, at a wavelength of 318nm.

In this Section, we have used Mie theory simulations to briefly review the effect of varying the particle size, refractive index of the surrounding medium and the type of metal, on the optical behaviour of an illuminated nanosphere in a homogenous medium. These simulation results can be viewed as a supplement to the detailed review on Mie theory and optical characteristics of plasmonic nanoparticles in Chapter 2 of this work. In the next Section, we will describe the implementation of the numerical FDTD technique for the simulation of plasmonic particles.

4.4 Finite-Difference Time-Domain Simulation Technique

The Finite-Difference Time-Domain (FDTD) technique is a grid-based numerical solution to Maxwell's differential equations. FDTD can be viewed as a method to discretise and evaluate electric and magnetic fields in time and space, in accordance to an algorithm proposed by Yee [49]. The FDTD technique offers several advantages when it comes to simulating the plasmonic light-scattering by metal nanoparticles. As the solutions to electric and magnetic fields are evaluated in the time-domain, a Fourier transform of one simulation can be used to obtain broadband spectral results. This is particularly useful for plasmonic scattering simulations, where it is important to trace the plasmonic resonance wavelength in the scattering spectrum and evaluate the broadband characteristics of the resonance peak. Unlike Mie solutions, the FDTD technique can be used to resolve electric field intensities for nanoparticles with complex geometries. However, as FDTD is an iterative numerical technique, its solutions are in some cases computationally intensive and subject to numerical inaccuracies, as will be highlighted in the following sections.

4.4.1 Optical Characteristics of a Single Nanosphere

4.4.1.1 Evaluating Q_{scat} and Q_{abs}

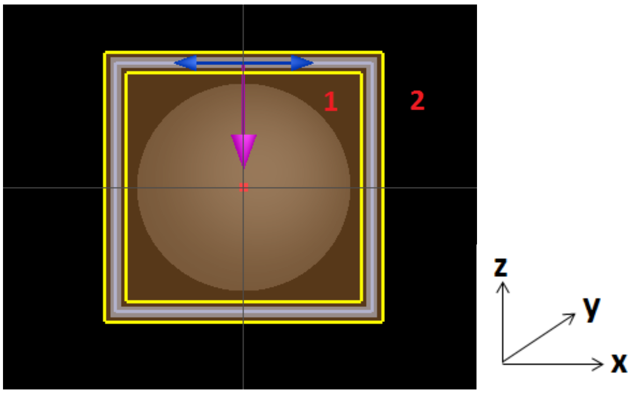

Figure 4.5: Snapshot of the x-z plane of a Total-Field Scattered-Field (TFSF) p-polarised source, propagating in the z-direction, injected into a Ag nanosphere. The grey shaded region represents the boundary of the TFSF source. The boundary separates the computation region into (1) Total field (incident + scattered field region) (2) Scattered field region. The outlines in yellow represent the box formed by the power monitors to calculate the total and scattered power. The orange region that extends to cover the TFSF source, is the mesh override region used to obtain higher resolution near the curved edges of the sphere. Note that the PML boundaries are not shown in this snapshot.

Throughout this report, unless otherwise stated, we have used Lumerical FDTD Solutions, a FDTD based software for simulating the optical characteristics of a single nanoparticle in three-dimensional space. Figure 4.5 illustrates the FDTD simulation design used to compute the Q_{scat} and Q_{abs} of a Ag nanosphere in vacuum. In order to separately evaluate the Q_{scat} and Q_{abs} of the nanosphere, we implement the Total Field Scattered Field (TFSF) light source provided by Lumerical. The TFSF source is a plane wave source which separates the computation region into a total field region (sum of incident and scattered field) and a scattered field region [78]. The TFSF boundary is represented as a grey shaded region in Figure 4.5. If the simulated nanostructure has a rotational symmetry, as is the case for the nanosphere and nanodisc structures simulated in this thesis, the optical properties of the single nanostructure are independent of the source polarisation. The nanosphere in Figure 4.5 is in a meshed region (represented in orange) with a span equal to that of the TFSF source – the need for a mesh and the significance of mesh size is discussed in detail in Section 4.4.1.2.

The calculation of Q_{abs} requires an evaluation of the power absorbed by the nanoparticle. The Poynting vector, which can be derived from Maxwell's differential equations, defines the direction and density of power flow at a given point. The Poynting vector is defined as [79]

$$\vec{\mathbf{P}} = \vec{\mathbf{E}}\,\mathbf{x}\,\overrightarrow{\mathbf{H}^{*}} \qquad (1)$$

where,

$\vec{\mathbf{P}}$ is the time-average Poynting vector,

$\vec{\mathbf{E}}$ is the electric field vector,

$\vec{\mathbf{H}}^{*}$ denotes the conjugate of the magnetic field vector

Note that $\vec{\mathbf{P}}$, $\vec{\mathbf{E}}$ and $\vec{\mathbf{H}}$ are all frequency dependent.

We confine the nanoparticle in a box defined by 6 power monitors, placed in the total field region of the TFSF source (Figure 4.5). The power monitor in each plane, records the time-average Poynting vector. We then use a built-in 'transmission' function to integrate the time-average Poynting vector, over the surface of a power monitor, to give the total power transmitted through that monitor.

Given the above method, the calculation of Q_{abs} can be understood in the following manner: in the absence of any particle in the total field region, the net power (calculated by summing the power through each power monitor in the box configuration) is zero, as the fields entering the space defined by the box equal the fields exiting the space. However, the presence of a nanoparticle, results in some power being absorbed and consequentially, the net power will be less than zero. The absolute value of this net power is the power absorbed by the nanoparticle. The absorption cross section area (C_{abs}) of the nanoparticle is then calculated as the ratio of the power absorbed to the intensity of the source, over a defined wavelength range. Finally, Q_{abs} is evaluated as the absorption cross section area, normalised to the cross sectional area of the nanoparticle, with reference to the incident source. Q_{scat} is calculated in a similar manner to Q_{abs}, with the only difference being that the box defined by the 6 power monitors is now placed in the scattered field region of the TFSF source.

In our simulations, we have ensured that there is at least 20nm spacing between the different objects in the simulation. The boundary conditions of the simulation region are set to be perfectly matched layers (PML), designed to absorb the stray scattered light. Each boundary is 24 PML layers thick. Increasing the number of PML layers increases the capability of the PML boundary to absorb light, but results in a trade-off in simulation time. Increasing the simulation region volume is another way to avoid unwanted reflection of light into the monitors from poorly absorbing PML layers.

4.4.1.2 Influence of Mesh Size

As FDTD is a grid-based numerical solution to Maxwell's differential equations, it is important to accurately define the grid size with mesh settings. Simulation studies in this work, will involve spherical and disc-shaped metal nanoparticles, in vacuum or on a multilayer stack. In order to account for the change in the wavelength of an electromagnetic wave with refractive index, an auto non-uniform mesh setting is used to ensure that the mesh size is graded with a material's refractive index. A mesh override region, as illustrated in Figure 4.5, allows for the description of a finer mesh, hence higher resolution, near a significant interface, for e.g. the curved surface of a sphere. Extending the mesh override region to include the TFSF source further improves the simulation results.

Figure 4.6 shows a comparison between the Mie theory-based values and FDTD simulated values for Q_{scat} and Q_{abs} of a 160nm diameter Ag nanosphere. The importance of the mesh size in the mesh override region can clearly be seen for simulated values of Q_{abs},

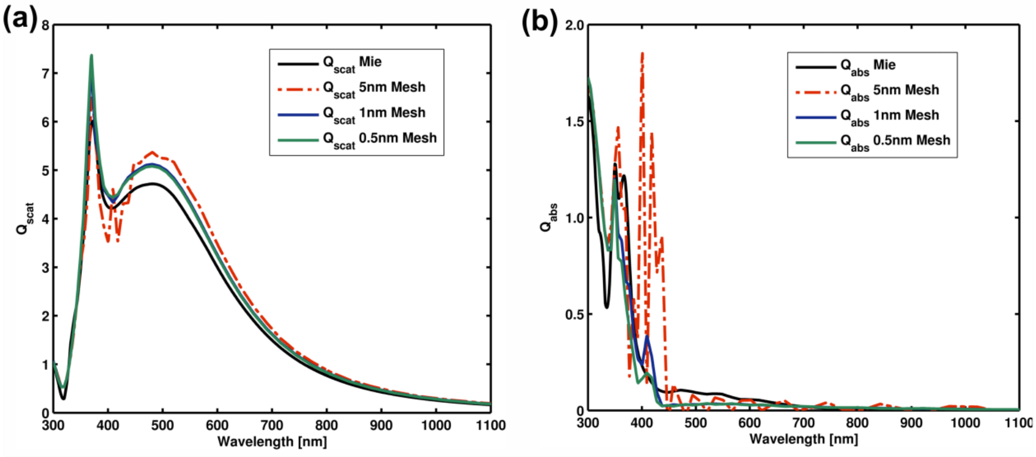

Figure 4.6: Comparison between the theoretical Mie solution and the FDTD simulation of **(a)** Q_{scat} data **(b)** Q_{abs} data for a 160nm diameter Ag sphere in vacuum, for different mesh sizes. The effect of decreasing the mesh size from 5nm to 0.5nm is illustrated: a finer mesh size results in lower discrepancy between the numerically simulated values and Mie-theory based analytic values.

where the difference between analytic and simulated results significantly reduces as the mesh size is reduced from 5nm to 0.5nm. The peak position of the plasmon resonance matches well with the corresponding Mie results. However, it is important to note that the simulated absorption spectra, irrespective of the mesh size used, do not represent the features of the analytic absorption spectrum, which occur just below the plasmon resonance at 352nm wavelength. These features in the absorption spectra of Ag arise due to electronic interband transitions [31]. The failure to represent these interband transition features can be considered to be a drawback of the multi-coefficient material fitting model (used to fit optical constants in FDTD by Lumerical), when compared to a Drude-Lorentz model, where the latter is specially designed to include interband transition effects. Further, Figure 4.6a clearly shows that despite a sufficiently good material fit, and fine mesh size of 0.5nm, the simulated value of the Q_{scat} peak, differs from the theoretical value by nearly 6%.

As seen in Figure 4.7, the FDTD simulation method, detailed in the sections above, gives near-to-analytical results for the Q_{scat} and Q_{abs} of Ag spheres with diameters of 160nm and 280nm, in a surrounding medium of refractive index, n = 1.

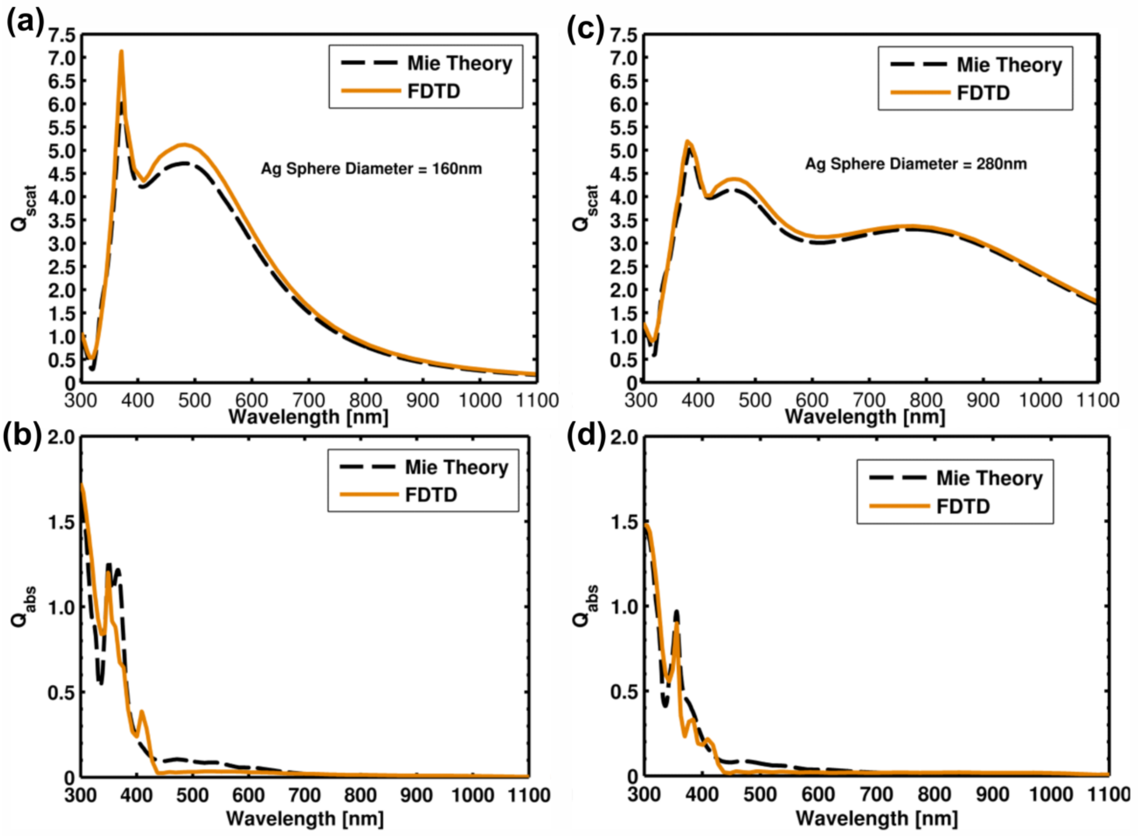

Figure 4.7: Comparison between the FDTD simulated **(a, b)**: Q_{scat} and Q_{abs} data for a 160nm diameter Ag sphere and **(c, d)**: Q_{scat} and Q_{abs} data for a 280nm diameter Ag sphere in vacuum, with a mesh size of 1nm in the mesh override region. The surrounding medium has a refractive index, n = 1.

4.5 Conclusions

In this Chapter, we reviewed the optical effects of varying the size, metal type and surrounding medium of a metal nanoparticle using simulations based on Mie theory, which is discussed in detail in Chapter 2. Mie simulations confirmed the reduction in the peak value of Q_{ext} with an increase in particle size. The simulations were also used to demonstrate that the radiative efficiency, the wavelength and the bandwidth of the plasmonic dipolar resonance increase with particle size. Higher order modes are excited in particles with diameters in the order of the wavelength of incident light. An increase in the refractive index of the surrounding medium also causes a red-shift in the plasmonic resonance with no significant decrease in peak magnitude. The broadband radiative efficiency comparisons for nanospheres with diameters of 100nm, composed of different types of metals: Ag, Al, Au and Cu, demonstrated that the Ag nanosphere has the highest broadband radiative efficiency in the visible to NIR wavelength range. We also reviewed the method for the numerical FDTD simulation technique for calculating the plasmonic scattering and absorption by a metal nanoparticle. The accuracy of the grid-based FDTD method is dictated by the size of the mesh used to define significant interfaces and curvatures. A simulation with a finer mesh size also requires a longer computational time. The FDTD simulation method, as developed in this Chapter successfully provided near-to-analytical results for Q_{scat} and Q_{abs} for metal nanospheres of different sizes.

[This page intentionally left blank]

Chapter 5

Self-organised Nanoparticles near a Mirror

(Results in this Chapter have been published in: R.S.A. Sesuraj, T.L. Temple and D.M. Bagnall, *Optical Characterization of a Spectrally Tunable Plasmonic Reflector for Application in Thin Film Silicon Solar Cells*, Solar Energy Materials & Solar Cells, **111**, pp23-30, 2013.)

5.1 Introduction

Based on the review of plasmonic solar cells in Chapter 3, we know that placing nanoparticles near the rear metal contact allows for the interaction with weakly-absorbed NIR photons and eliminates out-coupling losses due to the inclusion of the rear mirror. The review also showed that the thermal annealing of thin metal films into self-organised islands is the most common method used for the fabrication of randomly arranged nanostructures. Studies implementing the self-organised mirror structure include islands with an average diameter in the order of 100nm [71, 19]. This choice in the size of the islands can be backed by the Mie theory simulations (refer Chapter 4) which indicate that metal nanospheres with diameters in the order of the wavelength of incident light have a high broadband radiative efficiency (hence, low parasitic absorption losses), particularly in the visible-NIR region. Recent research on the self-organised mirror structure also includes studies on the light-scattering properties of the mirror in air [24]. The studies suggest that a mirror with a high diffuse reflectivity in air will also exhibit a high-diffuse reflectivity near a medium of high-refractive index and will preferentially scatter light into the medium [71, 24]. In this Chapter, we will experimentally investigate the light-scattering by Ag islands near a Ag mirror. The aim of the experiment is to firstly study the effect of varying the distance between the Ag islands and the Ag mirror on light-scattering. We will also study the limitations of the self-organised mirror system, particularly the extent of parasitic absorption losses. Such an investigation will aid the formation of design rules for producing a self-organised plasmonic mirror with high diffuse reflectivity in the NIR.

5.2 Experimental Method

5.2.1 Fabrication

As seen in Figure 5.1, the plasmonic mirror consists of self-organised Ag islands on varying thicknesses of ZnO on a planar Ag mirror substrate. ZnO and ITO are two of the commonly used transparent conducting oxide layers in a solar cell. In the current fabrication process, the availability of an ALD-based deposition method for ZnO is one of the reasons for using this material as the separation layer in the plasmonic mirror. The Ag islands were fabricated by the thermal annealing of thin Ag films. A Leybold BAK600 electron beam evaporator is used to deposit Ag films at a rate of 0.1nms^{-1} on a ZnO layer on a 100nm-thick Ag mirror. The ZnO layer is deposited using a PT05 OIPT FlexAl atomic layer deposition system. The thickness of the ZnO is varied to tune the separation distance between the Ag islands and the mirror. The Ag films were subject to a rapid thermal anneal of 400^{o}C for 30min in a N_2 atmosphere to form Ag islands. The thickness of the Ag film is varied to tune the size of the Ag islands (refer Section 5.4 for more details).

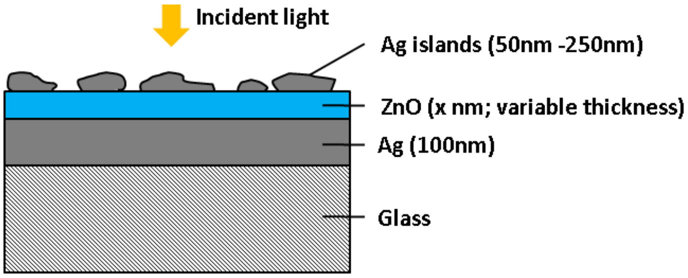

Figure 5.1: Cross-section diagram of the fabricated plasmonic mirror structure.

5.2.2 Optical Characterisation

Total and diffuse reflectance measurements are conducted using a 6-inch DTR6 integrating sphere (IS), coated on the interior with highly diffusive $BaSO_4$. A Quartz-Halogen (QH) probe source coupled with a TMc300 scanning multiple-grating monochromator is used as a light source. Both the DTR6 IS and the light source are part of a Bentham PVE300 photovoltaic spectral response characterization system. All IS measurements have been conducted for a beam with a spot-size of 2mm, incident at an angle of 8^{0} to the sample normal.

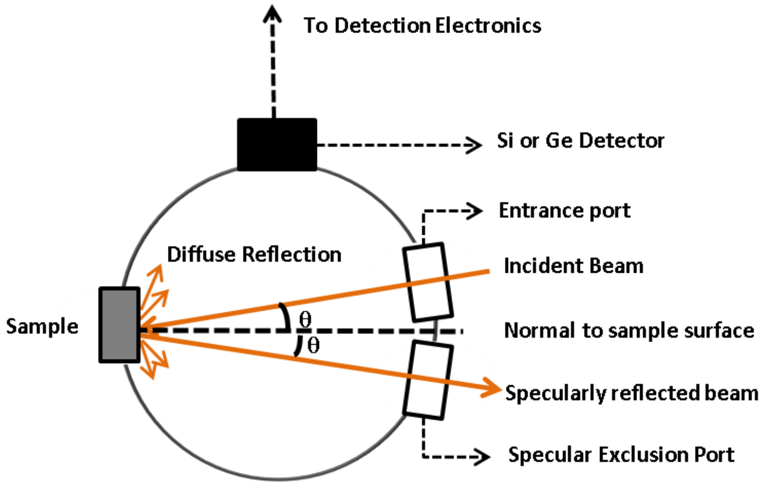

Figure 5.2: Side-view of the integrating sphere used for single-beam measurement of diffuse and total reflectance for a given sample. The light beam is incident at an angle, $\theta = 8^o$ with respect to the sample normal; light is specularly reflected at an angle of $8^o$and any light scattered an angle greater than 8^o is said to be diffusely reflected. Total and diffuse reflectance measurements are made by closing and opening the specular exclusion port, respectively. The diagram is not to scale.

IS-based diffuse reflectance measurement is an effective measure of the scattered radiation averaged over a broad range of scattered angles. In the current arrangement, light scattered at any angle greater than 8^o to the sample normal, is defined as diffusely reflected and hence is representative of the light scattered by the plasmonic mirror (Figure 5.2). Total reflectance measurements have been used to trace parasitic absorption losses in the plasmonic mirror. Total reflectance is the sum of diffuse and specular reflectance. A trough in the total reflectance spectra is indicative of optical absorption losses as percentage absorption is defined as 100%-total reflectance.

All IS measurements reported in this Chapter are single-beam measurements. The total sample area is around 0.1% of the surface area of the sphere. Hence, any errors in the measurements due to a change in the surface characteristics of the sphere with the introduction of the sample are assumed to be minimal. A wavelength range of 300nm to 1500nm is used for spectral characterisation. The characterisation over this wavelength range required two detectors: a Si detector for the 300nm to 800nm wavelength range and a Ge detector for the 800nm to 1500nm wavelength range. The spectral data obtained using the two detectors is corrected at the region of overlap (dependent on the sample) to concatenate the spectra.

5.3 Optical Characteristics of a Conventional Textured Ag Mirror

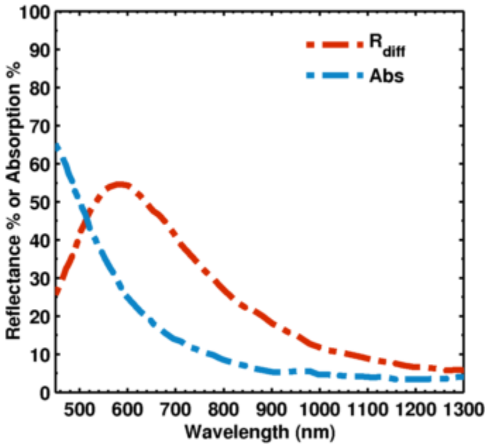

Figure 5.3 Percentage diffuse reflectance (R_{diff}%) and percentage absorption (Abs%) of a 200nm Ag mirror on an Asahi-U textured TCO substrate. The data has been obtained by digitisation[12] of published results in a recent study by Sai *et al.* [20]

A scattering component integrated at the rear of a μc-Si:H solar cell must exhibit high diffuse reflectance and low parasitic absorption losses in the near-bandgap, NIR region, from approximately 600-1100nm. Sai *et al.* in their study on textured surfaces in a μc-Si:H solar cell, measured the total and diffuse reflectance, in air, for a conventional textured Ag mirror used in μc-Si:H solar cells. The textured mirror is fabricated by depositing 200nm Ag onto an Asahi-U substrate [20]. Chapter 1 of this work also reviewed the potential of Asahi-U TCOs for light-trapping in solar cells. Figure 5.3, illustrates the parasitic absorption losses (calculated as 100%-total reflectance) and the diffuse reflectance for the textured mirror. Although the mirror shows low absorption losses in the NIR region, the diffuse reflectance also reduces sharply from 55% at 600nm to approximately 10% at 1100nm. We have included this result in order to later compare (Section 5.4) the NIR light-scattering properties of the plasmonic mirror with metal islands to that of a conventional textured Ag substrate.

---

[12] The digitisation of the graph from the paper by Sai *et al.* [20] was done using a freely available digitiser developed by Ankit Rohatgi: http://arohatgi.info/WebPlotDigitizer.

5.4 Experimental Results: Self-organised Mirror

5.4.1 Influence of the Spacer Thickness on the Island Morphology

The equivalent diameter of the metal islands is defined as the diameter of a circle with an equal area. The equivalent diameter is measured by processing the corresponding top-down SEM images of the Ag islands, using an open-source software, ImageJ. The insets in Figure 5.4a and 5.4d depict examples of top-down SEM images of metal islands formed by annealing 10nm and 15nm Ag films[13] at a separation distance of 50nm, respectively.

Ideally, the size of the metal islands should be constant irrespective of the change in the separation distance. However, the boxplots of the equivalent diameter distribution for annealed Ag films of 10nm and 15nm thicknesses (Figure 5.4c and 5.4f, respectively), clearly show a 40-70nm difference in the median diameter value with a change in separation distance. There is also a discernible variance in the size distribution of the metal island films at each separation distance as indicated by the width of the boxes (i.e. the interquartile range).

Hence, despite the thickness of the annealed film being constant at each separation distance and the samples being prepared under the same deposition conditions, there is a variance in the median diameter of the Ag islands with the thickness of the ZnO layer. Comparisons of SEM images of samples with as-deposited and annealed Ag films on varying thicknesses of ZnO on a Ag mirror (results not included) indicate that the observed change in metal island size with ZnO thickness is a result of the annealing process. The variance in the median size of the Ag islands with the island-mirror separation distance is an important limitation of the current fabrication process.

---

[13] The thickness of the film is typical of the film thickness used for fabrication of metal islands based on a review of relevant literature [71, 24, 61]. As the fabrication of metal-islands by thermal annealing has been extensively studied and reviewed in previous literature as detailed in Chapter 3 of this work, we have used the available data to determine the required film thickness and anneal temperature for fabricating islands with average sizes in the order of 100nm.

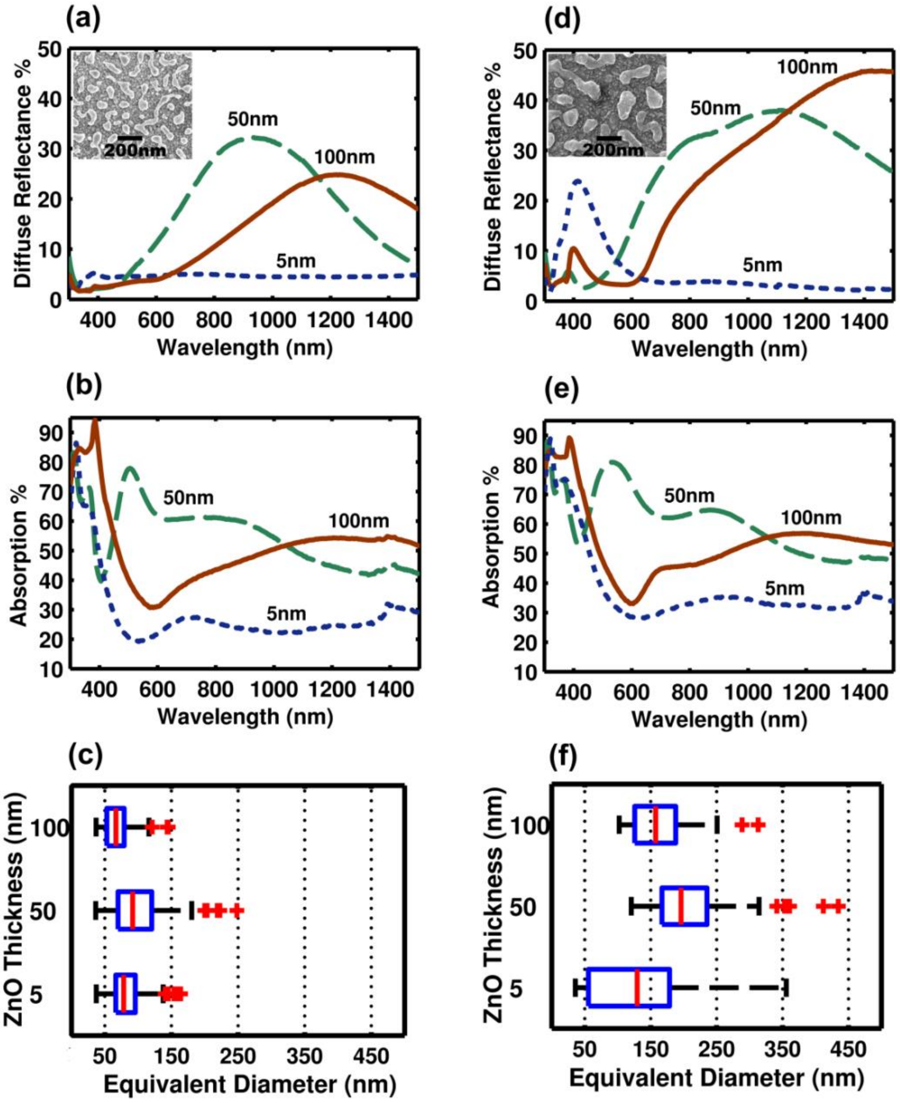

Figure 5.4 Morphological and optical characteristics for Ag islands formed by annealing a **(a-c)** 10nm Ag film and **(d-f)** 15nm Ag film at separation distances of 5nm, 50nm and 100nm from the Ag mirror: **(a,d)** Percentage diffuse reflectance (Diffuse Reflectance %). The insets in the figures show the SEM images of Ag islands formed by annealing **(a)** 10nm and **(d)** 15nm Ag films at 50nm separation distance from the Ag mirror. **(b,e)** Percentage absorption (Absorption%) **(c,f)** Boxplots of the equivalent diameter distribution for Ag islands at each separation distance. The line within the boxes depicts the median value. The width of the boxes indicates the diameter range comprising 50% of the size distribution. The crosses indicate the outlier diameter values.

5.4.2 Influence of the Spacer Thickness on Diffuse Reflectance

The diffuse reflectance is a measure of the scattering of light by the Ag islands-near-mirror structure. The review on LSPs in Chapter 2, showed that the electric field driving the plasmonic resonance, and hence the scattering and absorption of light by a metal nanosphere, is influenced by the incident electric field ($\mathbf{E_i}$), the electric field inside the sphere ($\mathbf{E_j}$) and the scattered electric field ($\mathbf{E_s}$) which arises due to the scattering of electromagnetic radiation by resonant LSPs.

In Chapter 3, for the Ag islands-near-mirror structure implemented by Stuart and Hall [67], Johansson numerically demonstrated that the diffuse reflectance intensity is most likely due to the driving field being influenced by interference effects in the multilayer substrate [64]. Hence, in our case, the diffuse reflectance of the plasmonic mirror can also be presumed to be influenced by the interference between the incident, scattered and reflected-scattered radiation. This interference will also include the interaction between the unscattered radiation reflected at the ZnO-air interface and at the ZnO-Ag mirror interface which has an additional phase lag as a result of the ZnO layer.

Figure 5.4a and 5.4d illustrate the trend in diffuse reflectance with island-mirror separation distance, for Ag islands formed by annealing Ag films of thicknesses, 10nm and 15nm, respectively. It is evident from these figures that the plasmonic mirror exhibits a significantly higher diffuse reflectance in the NIR region when compared to the conventional textured Ag mirror (Figure 5.3). In Figures 5.4a and 5.4d, for Ag islands at separation distances of 50nm and 100nm, the diffuse reflectance beyond a wavelength of 900nm, is almost 20-30% higher than that of the textured Ag mirror in this spectral region.

A closer analysis of the experimental trend in diffuse reflectance, in Figure 5.4a, indicates a red-shift and an increase in the bandwidth of the diffuse reflectance peak as the separation distance is varied from 5nm to 100nm. In Figure 5.4d, the average size of the Ag islands is increased by increasing the thickness of the annealed film to 15nm. An increase in the average size of the islands, results in an increase in the absolute magnitude of the peak diffuse reflectance at each separation distance (cf. Figures 5.4a and 5.4d). Mie theory predicts an increase in the scattering cross-section with the size of a metal nanosphere [38]. Hence, the increase in the percentage diffuse reflectance with the size of the metal islands can be attributed to the increase in radiative efficiency with average metal-island size.

Theoretically, the plasmonic resonance should also exhibit a red-shift with an increase in the size of a plasmonic particle. For the 15nm Ag film (Figure 5.4f) the median metal island size is larger at a separation distance of 50nm when compared to the island size at a separation distance of 100nm. However, despite the increase in the metal island size, the diffuse reflectance spectra of the Ag islands at a separation distance of 100nm, is more red-shifted than the corresponding spectra for a separation distance of 50nm (Figure 5.4d). A similar effect is observed for the 10nm Ag film annealed at separation distances of 50nm and 100nm (cf. Figures 5.4a and 5.4c). Hence, the spectral diffuse reflectance of the mirror is influenced more by the separation distance between the islands and the mirror than the average size of the islands. For a very close separation distance of 5nm, the diffuse reflectance is reduced significantly beyond a wavelength of 600nm, irrespective of the metal island size (c.f. Figure 5.4a and 5.4d).

In Figure 5.4d, at a distance of 100nm, there are two diffuse reflectance maxima: a peak at 400nm, with a magnitude of 10% and a narrow bandwidth and a second peak at 1440nm with a significantly higher diffuse reflectance of 46% and a wider bandwidth. Between these two maxima, in the intermediate spectral range of 480-630nm, there is a distinct reduction in the magnitude of the diffuse reflectance. Hence, the diffuse reflectance for an island-mirror separation of 100nm (Figure 5.4d) illustrates the spectrally selective feature of the interference between the incident, reflected-scattered and unscattered fields.

5.4.3 Influence of the Spacer Thickness on Absorption Losses

The percentage absorption losses of the mirror can also be modulated by varying the separation distance. Figure 5.4b shows that a doubling of the separation distance from 50nm to 100nm, results in a 16-48% decrease in percentage absorption in the 500-1000nm spectral range. The absorption losses of the plasmonic mirror exceed the losses exhibited by the textured Ag substrate (c.f. 5.4b and 5.3). The high broadband absorption losses are one of the main limitations of the metal islands-near-mirror structure. From a thin film solar cell application perspective, the absorption peaks in the short wavelength range, for e.g. at a separation distance of 50nm, will not contribute to absorption losses in a rear-integrated plasmonic mirror as short-wavelength photons are readily absorbed in the absorber layer before reaching the plasmonic mirror.

The similarity between the absorption spectra at varying separation distances, between the 10nm Ag film in Figure 5.4b and the annealed 15nm Ag film in Figure 5.4e, clearly indicates, as in the case of diffuse reflectance, that the absorption losses are influenced more by the separation distance than the average size of the metal islands.

5.4.4 Integrated Near-Infrared Total and Diffuse Reflectance

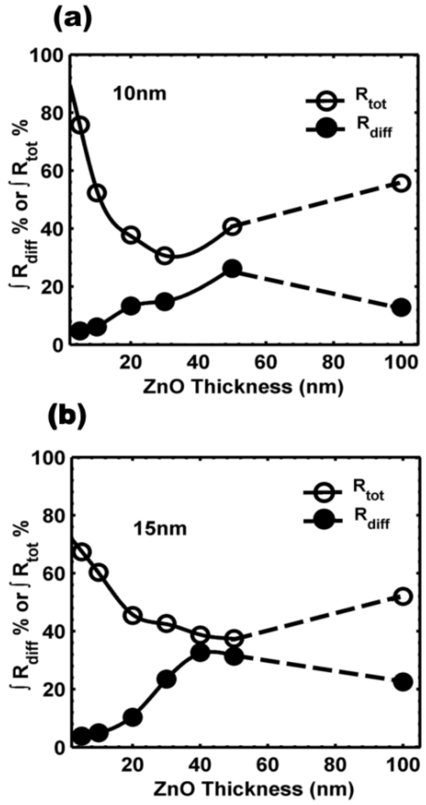

Figure 5.5 Total Integrated reflectance (R_{tot} %) and diffuse reflectance (R_{diff}%) over the 600-1100nm spectral range for metal islands formed by annealing **(a)** 10nm and **(b)** 15nm Ag films at varying separation distances from the Ag mirror.

As light-scattering components for thin film Si solar cells need to be optimised for a specific spectral region, it is useful to integrate the percentage total and diffuse reflectance values of the plasmonic mirror over the near-bandgap spectral range. Figure 5.5a and 5.5b illustrate the integrated percentage total and diffuse reflectance over the 600-1100nm spectral range, for metal islands fabricated using Ag films with thicknesses of 10nm and

15nm, respectively. The median size of the islands formed by annealing the 10nm film is 90nm and for the 15nm film is 200nm.

An ideal scattering component will have a 100% total and diffuse reflectance i.e. no parasitic absorption losses. However, for a non-ideal plasmonic mirror, the collective excitation of LSPs in the metal islands results in the simultaneous activation of radiative and non-radiative processes [32], and hence parasitic absorption losses in the metal-islands cannot be avoided. For an efficient light-scattering system, the absorption losses need to be minimised in the target spectral region.

It can be observed that the trend in the total and diffuse reflectance with separation distance is similar for the two sizes of metal islands. For each metal island size, there is an intermediate distance, between 40-50nm, where the diffuse reflectance reaches a maximum. An important consequence of increasing the average metal island size is the relative increase in the percentage diffuse reflectance at each separation distance. For example, increasing the annealed film thickness from 10nm to 15nm at a separation distance of 50nm, increases the percentage diffuse reflectance by approximately 8% while keeping the total reflectance value (and hence absorption losses) reasonably constant. Interestingly, irrespective of the size of the metal islands, the diffuse reflectance at very close distances to mirror, i.e. between 5-10nm, is significantly reduced.

The percentage absorption for the plasmonic mirror shows a direct correlation with percentage diffuse reflectance, as the separation distance is increased from 5nm to 100nm, (Figures 5.5a and 5.5b). The minimal absorption losses are observed for metal islands at an island-mirror separation distance of 100nm. It is important to note that not all of the absorption is due to parasitic absorption losses in the random array of metal islands. Optical characterisation results (not included) indicate a 15% absorption loss in the 100nm ZnO layer. Hence, the actual parasitic absorption losses due to metal islands must be lower than 48%. The absorption losses can be attributed to the limitations of the fabrication process, which despite being large-scale and commercially viable gives limited control on the surface coverage, shape and size distribution of the metal islands.

5.5 Conclusions

In this Chapter we have studied the effect of varying the island-mirror separation distance on the light-scattering behaviour for Ag islands near a Ag mirror. For a separation distance of 100nm, the plasmonic mirror shows a higher diffuse reflectance and stronger light-scattering in the NIR region when compared to a conventional textured mirror. The diffuse reflectance peak red-shifts and increases in bandwidth with the separation distance. For a given metal island size, there is a separation distance for which the magnitude of the peak diffuse reflectance is optimised. The spectral tunability of the diffuse reflectance and the parasitic absorption loss with separation distance is possibly a consequence of the driving field being influenced by interference effects in the underlying optical stack. The broadband absorption losses in the plasmonic mirror exceed the losses exhibited by a conventional textured mirror. In the next Chapter of this work we will implement a fabrication process which offers more control over the size, shape and interparticle distance of metal nanostructures, with an aim to reduce the broadband absorption losses of a plasmonic mirror structure.

[This page intentionally left blank]

Chapter 6

Plasmonic Mirror by E-beam Lithography

(Results in this Chapter have been published in: R.S.A. Sesuraj, T.L. Temple and D.M. Bagnall, Tunable Low-loss Plasmonic Mirror for Diffuse Optical Scattering, Applied Physics Express, **5**, pp.125205-1–125205-3, 2012)

6.1 Introduction

For metal nanoparticles situated in a homogeneous medium, the localised surface plasmon (LSP) resonances are driven by the electric field of incident photons. If interfaces are present, the interference between the incident light and light reflected at each interface will affect the driving field spectrum. Driving field effects are most strongly evident for metal nanoparticles situated in close proximity to highly reflective surfaces. As reviewed in Chapter 3, Stuart and Hall [27] attributed the long-wavelength variations in diffuse reflection intensity by a Ag islands near a Ag reflector to waveguide-mediated interparticle coupling. However, a later simulation study by Johansson demonstrated that the variations in the diffuse reflectance intensity were due to variations of the driving field intensity caused by interference effects [64].

In the first part of this Chapter, we explain the concept of the plasmonic driving field for an illuminated Ag nanodisc on a multi-layer substrate. We use 3D FDTD single particle simulations to simulate a metal nanodisc-near-mirror structure. The thickness of the spacer layer between the nanodisc and the mirror, and the material type of the mirror and the spacer are varied demonstrate the spectral dependence of the scattering cross-section on the driving field.

In the second part of this Chapter, we develop an e-beam lithography (EBL) process to fabricate a plasmonic mirror with a pseudo-random array of Ag nanodiscs. The peak driving field intensity is spectrally tuned by varying the separation distance between the nanodisc array and the mirror, while the plasmonic resonance position is tuned by modifying the nanodisc diameter. The main focus of this work is to develop an efficient light-trapping component for μc-Si:H solar cells. Hence, in this Chapter, we will aim to fabricate a plasmonic mirror with low broadband absorption losses and a high diffuse reflectivity in the NIR region, over a broad angular range.

6.2 The Electric Driving Field

Figure 6.1 is a simple 2D illustration of the electric fields which dictate the optical behaviour of a metal nanostructure (a nanosphere structure has been chosen for ease of explanation) near a planar mirror. For the case of an isolated sphere in a homogeneous medium, we will consider Figure 6.1 without the planar mirror, i.e. without the contribution of the reflected-scattered field, $\mathbf{E_{rs}(\theta_{rs})}$ and the specular-reflected field, $\mathbf{E_r}$. There are then three fields to consider: a parallel polarized incident field, $\mathbf{E_i}$, the LSP driving field, $\mathbf{E_d}$, and the scattered field, $\mathbf{E_s(\theta_s)}$. For ease of explanation, we consider the case of normal incidence and the excitation of the dipolar LSP mode. Although the optical properties of a metal nanosphere are independent of the polarization of $\mathbf{E_i}$ for normal incidence, the polarization of $\mathbf{E_i}$ has been included to emphasise its effect on $\mathbf{E_d}$.

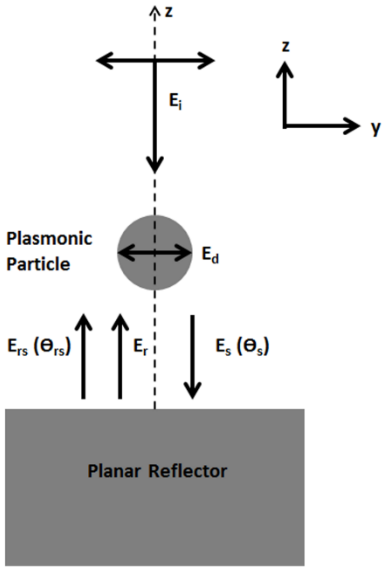

Figure 6.1 2D illustration of the electric fields which dictate the optical behaviour of a metal nanosphere near a planar mirror. $\mathbf{E_i}$ is a parallel polarized incident field at normal incidence, $\mathbf{E_r}$ is the specular-reflected field, $\mathbf{E_d}$ is the LSP driving field, $\mathbf{E_s(\theta_s)}$ is the scattered field radiated from the plasmonic particle and $\mathbf{E_{rs}(\theta_{rs})}$ is the reflected-scattered field.

$\mathbf{E_i}$ induces a dipole moment $\mathbf{P}$ which oscillates in a direction parallel to the polarization of $\mathbf{E_i}$. The dipole moment for the case of an isolated metal nanoparticle in a homogenous medium is given by [35]

$$\mathbf{P} = \alpha\varepsilon_0\mathbf{E_d} \qquad (1)$$

where α is the polarizability of the particle and ε_o is the free-space permittivity.

For the illuminated metal nanodisc in vacuum, the radiative decay of the excited LSPs results in the scattered field $\mathbf{E_s(\theta_s)}$. However, when the disc is near a planar mirror, as in Figure 6.1, two important changes occur. Firstly, $\mathbf{E_d}$ is influenced by the interference between $\mathbf{E_i}$, $\mathbf{E_r}$ and $\mathbf{E_{rs}(\theta_{rs})}$. Secondly, the polarizability, α in (1) is modified into an 'effective polarizability', α_{eff} to account for the effect of the reflected-scattered field [35]. As a result of these two changes, the induced dipole moment in (1) is also modified and this in turn has an effect on the resultant total scattered power P_{scat} and optical scattering cross section C_{scat} which are given by [35]:

$$P_{\text{scat}} = \frac{\pi}{\lambda}\,\text{Im}\,[\,\mathbf{P}^{*}.\,\mathbf{E_d}] \qquad (\mathbf{2})$$

$$C_{\text{scat}} = \frac{P_{\text{scat}}}{I_{\text{in}}} = \frac{2\pi}{\lambda}\,\text{Im}\,[\alpha_{\text{eff}}].\,I_d \qquad (\mathbf{3})$$

where I_d is the intensity of $\mathbf{E_d}$ and I_{in} is the intensity of $\mathbf{E_i}$. The power absorbed and the absorption cross section are calculated in a similar method to equations (2) and (3). Hence, for the design of an efficient plasmonic mirror, based on (2) and (3), it is clear that the interdependence of $\mathbf{E_d}$, $\mathbf{E_{rs}(\theta_{rs})}$ and $\mathbf{E_s(\theta_s)}$ can be exploited to spectrally optimise the power scattered and minimise the power absorbed by the plasmonic scattering system.

6.3 FDTD Simulation Results

3D FDTD simulations have been used to understand the physical mechanism behind the spectral modulation of the scattering cross-section (hence scattered power) with spacer layer thickness and type of mirror and spacer layer material. The scattering cross-section (C_{scat}) and the electric driving field have been simulated for a Ag nanodisc near a Ag mirror structure. We have specifically chosen the scattering cross section (C_{scat}) over power scattered (P_{scat}) to represent the spectral properties of the light scattered by the nanodisc[14]. This is because the simulated value of C_{scat} is independent of the source size.

---

[14] This choice is based on the design restrictions specific to Lumerical Solutions v8.0. The details on the dependence of TFSF source size on scattered power are explained in the reference guide for the software: http://docs.lumerical.com/en/fdtd/user_guide_tfsf_power_normalization.html.

Optical constants for SiO_2 and Ag were taken from the tabulated data by Palik [80] and Johnson and Christy [76], respectively and fitted using a multi-coefficient model. A 1nm mesh override region is used to resolve the curved surfaces of the nanodisc.

6.3.1 Effect of Separation Distance on Plasmonic Scattering

We first consider the case without the nanodisc i.e. only the SiO_2-on-mirror substrate. Here, the electric field intensity, $|\mathbf{E}|^2$, is numerically computed at a distance of 25nm (corresponding to the centre of a nanodisc with a height of 50nm - the fixed height of nanodiscs used in the simulations throughout this work) above the SiO_2 surface, in the plane parallel to the simulated structure.

Without the nanodisc, $\mathbf{E}$ is a result of the interference between the incident field, $\mathbf{E_i}$ and the specular-reflected field $\mathbf{E_r}$, at the air-SiO_2 and SiO_2-Ag interfaces. The resultant electric field intensity, $|\mathbf{E}|^2$, is termed 'normalized electric field intensity'[15] as it is divided by the intensity of the incident field, $|\mathbf{E_i}|^2$. As seen in Figure 6.2, the $|\mathbf{E}|^2$ peak broadens and redshifts with increasing spacer thickness. When the spacer thickness exceeds 75nm, the trough in the $|\mathbf{E}|^2$ spectra redshifts and an additional peak develops at short wavelengths.

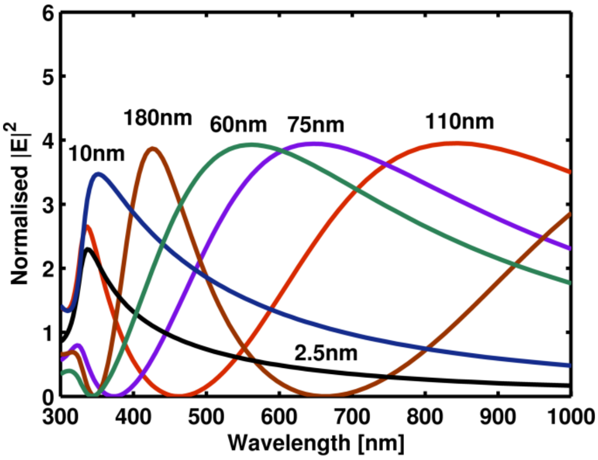

Figure 6.2 Electric field intensity, $|\mathbf{E}|^2$ at a distance of 25nm above varying thicknesses of SiO_2-on-Ag mirror.

---

[15] The term 'normalised' cross-section is used in the FDTD simulations to indicate that the power scattered has been normalised to the source intensity.

Hence, the spectral positions of constructive (peaks) and destructive (troughs) interference in the $|\mathbf{E}|^2$ can be selected by varying the spacer layer thickness.

In the absence of a nanodisc, the reflection from the SiO_2-on-mirror substrate is entirely specular. The introduction of a Ag nanodisc results in the excitation of LSPs, which decay radiatively resulting in scattering, or non-radiatively resulting in absorption. As explained in Section 6.2, the electric field, $\mathbf{E_d}$ at the centre of the nanodisc, is now the result of the interference between $\mathbf{E_i}$ and $\mathbf{E_r}$ and additionally the reflected-scattered field, $\mathbf{E_{rs}}(\boldsymbol{\theta}_{\mathbf{rs}})$ (with an angular dependence indicated by $\boldsymbol{\theta}_{\mathbf{rs}}$). The power scattered ($P_{scat}$) by the nanodisc is given by equation (2) in Section 6.2 and the normalised C_{scat} is calculated as the ratio of P_{scat} to the intensity of the incident source.

Now, we briefly consider the case without the Ag mirror, i.e., when a Ag nanodisc is placed on a semi-infinite SiO_2 substrate, without a mirror. We will initially consider a Ag nanodisc of diameter, 150nm and a height of 50nm. As seen in Figure 6.3a the resonance is principally excited by the incident field and the peak scattering occurs at a wavelength of 750nm. The peak C_{scat} is an order of magnitude higher than the actual geometrical cross-section of the nanodisc (plotted as a dotted line in Figure 6.3a). It can also be observed that the resonance for the nanodisc on semi-infinite SiO_2 is redshifted, with a slight decrease in the peak C_{scat} value, when compared to the resonance of the disc in vacuum. This briefly illustrates the effect of an increase in the refractive index of the underlying matrix on the scattering spectrum. The effect of the refractive index of the spacer layer on electric driving field will be discussed further in Section 6.3.3 of this Chapter.

The introduction of a mirror strongly modifies the scattering spectrum. In Figure 6.3b, the Ag mirror is introduced with 110nm SiO_2 between the nanodisc and the mirror. There is a clear spectral dependence of C_{scat} on $|\mathbf{E}|^2$. The presence of the mirror modifies the driving field which now exhibits a region of destructive interference in 400-500nm wavelength range and constructive interference at a wavelength of 850nm. The modification of the driving field results in the consequent suppression of the scattering in the 400-500nm wavelength range and enhancement of scattering at longer wavelengths. Although $|\mathbf{E}|^2$ continues to rise and eventually peaks at 850nm, C_{scat} steadily decreases in the long-wavelength range as the intrinsic scattering response of the nanodisc (cf. Figures 6.3 a and b) is weak in this region. The dependence of C_{scat} on $|\mathbf{E}|^2$ is further illustrated in Figure 6.3c, where the separation distance is decreased to 50nm. The scattering is now

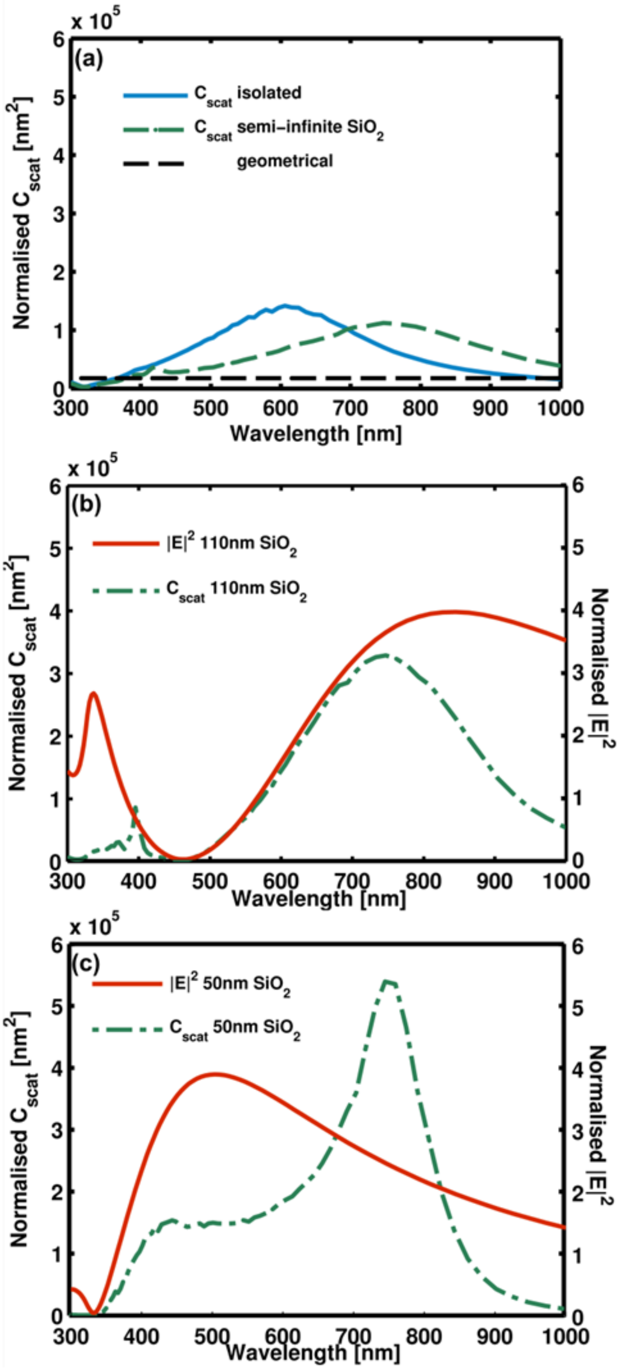

Figure 6.3: Simulation results for: **(a)** Normalised scattering cross section C_{scat} [nm^2] for a Ag nanodisc with 150nm diameter and 50nm height, in vacuum and on a semi-infinite SiO_2 substrate. **(b), (c) $|E|^2$** at 25nm above the SiO_2-on-Ag mirror, without the nanodisc (solid red line), on 110nm and 50nm SiO_2, respectively. Corresponding normalised scattering cross sections C_{scat} [nm^2], for the respective configurations, with the nanodisc are plotted as the green spectra.

enhanced in the 400-500nm wavelength range when compared to Figure 6.3b, because the corresponding **|E|**^{2} spectrum peaks in this wavelength range. The position of the scattering resonance is maintained at 750nm. The introduction of the Ag mirror, results in the magnitude of the scattering being significantly increased when compared to the nanodisc on a semi-infinite SiO_2 substrate.

6.3.2 Effect of Mirror Type on Plasmonic Scattering

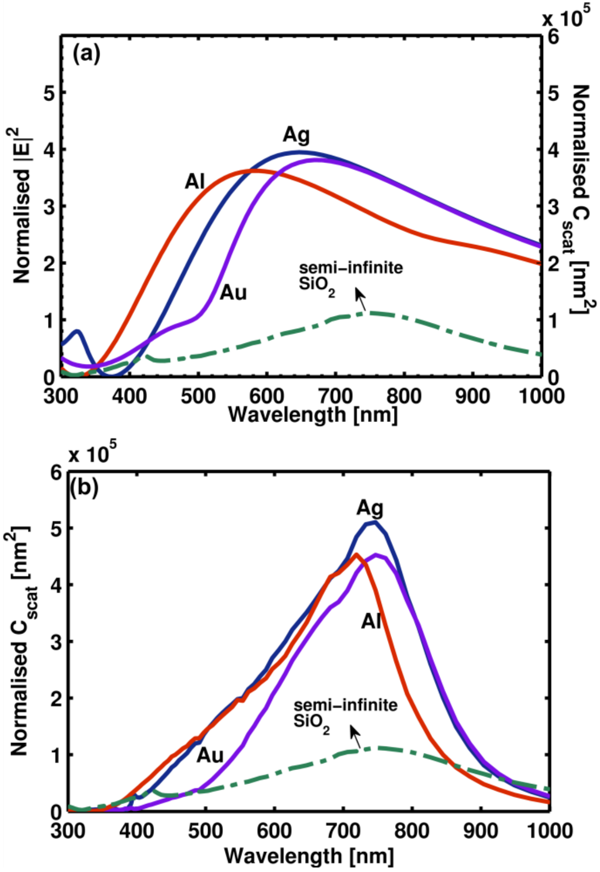

Figure 6.4 Simulation results for: **(a)** Electric field intensity **|E|**^{2} calculated without the nanodisc, at 25nm above 75nm SiO_2 on Au, Ag and Al mirrors. **(b)** Corresponding normalised scattering cross sections C_{scat} [nm^2] for a Ag nanodisc with 150nm diameter and 50nm height on 75nm SiO_2 on Au, Ag and Al mirrors. C_{scat} for the nanodisc on semi-infinite SiO_2 is plotted as the green dotted spectra, in both **(a)** and **(b)** for reference.

In order to further strengthen the argument of the spectral dependence of C_{scat} on **|E|**^{2}, we now evaluate the case of varying the type of mirror. The phase change of light that is reflected at the SiO_2-mirror interface exhibits a dependence on the complex refractive index of the mirror material [81]. Hence, the **|E|**^{2} spectra for the SiO_2-mirror matrix are also modified as a result of changing the type of mirror material (Figure 6.4a). If the thickness of the SiO_2 spacer is kept constant at 75nm, the peak **|E|**^{2} is higher for the case of the SiO_2-on-Ag mirror structure, near the intrinsic resonance wavelength of the nanodisc (750nm), as seen in Figure 6.4a. Accordingly, the peak value of C_{scat} for the nanodisc on SiO_2-Ag mirror substrate is higher than the C_{scat} values for the nanodisc on SiO_2-Au or SiO_2-Al substrates (Figure 6.4b). A comparison of Figures 6.4 a and b, illustrates the spectral dependence of C_{scat} on **|E|**^{2} in the long-wavelength range for the different mirror materials.

6.3.3 Effect of Spacer Type on Plasmonic Scattering

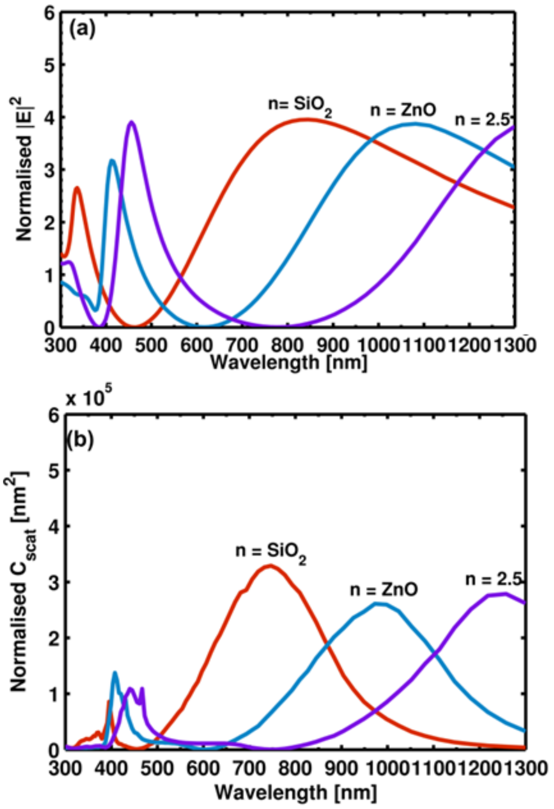

Figure 6.5 Simulation results for: (a) Electric field intensity **|E|^2** calculated without the nanodisc, at 25nm above spacer layers with a thickness of 110nm and different refractive indices, on a Ag mirror. (b) Corresponding normalised scattering cross sections C_{scat} [nm^2] for a Ag nanodisc with 150nm diameter and 50nm height on spacer layers with a thickness of 110nm and different refractive indices, on a Ag mirror. SiO_2 and ZnO have refractive indices of values, n ≈1.5 and n ≈2.0, respectively.

Figure 6.5 shows the spectral dependence of $|\mathbf{E}|^2$ and the corresponding C_{scat} on the refractive index of the spacer material. The distance of the nanodisc from the Ag mirror is kept constant at 110nm. When the refractive index of the spacer material is increased from n ≈1.5 to n ≈ 2.5, the $|\mathbf{E}|^2$ peak red-shifts resulting in a corresponding red-shift of the peak scattering wavelength (cf. Figures 6.5a and b). The peak value of C_{scat} is higher for the nanodisc on the SiO_2 spacer when compared to the spacer layers with higher refractive indices.

Figure 6.2 in Section 6.3.1 of this Chapter showed a spectral red-shift in peak $|\mathbf{E}|^2$ with the spacer layer thickness, for a spacer layer of a given refractive index. Now, the results in Figure 6.5, lead to the conclusion that increasing the refractive index of the spacer layer allows for the usage of a lower spacer layer thickness to achieve the desired spectral red-shift in peak $|\mathbf{E}|^2$ and peak C_{scat}.

FDTD-based single particle simulations have been used to demonstrate the spectral tunability of the plasmonic driving field, with particle-mirror separation distance and type of mirror and spacer layer material. We have demonstrated a spectral dependency of the scattering cross-section on the electric driving field and most importantly, shown that plasmonic scattering can be maximised for a given spectral range if the peak of the driving field is tuned to coincide with the intrinsic resonance of the nanodisc.

6.4 E-beam Lithography Fabrication Process

To date, there is an absence of experimental studies to optimise a random array of nanoparticles-near-mirror system for spectrally selective light-scattering. In Chapter 5, the self-organised method of annealing thin metal films is used to fabricate a random array of nanoscale metal islands near a mirror. Although the self-organised method is a large-scale, commercially-viable process, there is a high variance in the resultant nanoparticle size, shape and interparticle distance (and hence, surface coverage). Further, the nanoparticle morphology and surface coverage are dependent on the thickness of the underlying oxide layer [82]. A lack of control over the interparticle distance may result in interparticle coupling effects and may be one of the reasons for the high absorption losses exhibited by a self-organised plasmonic mirror [83]. Hence, the self-organised fabrication method is less suitable for a strategic study of the influence of spacer layer thickness on light-scattering.

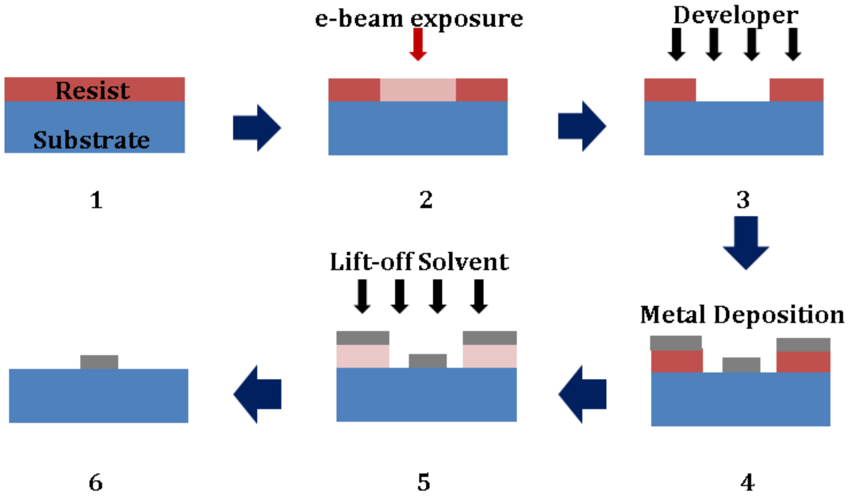

Figure 6.6 The main steps in a metal-lift off based electron beam lithography process. (1) Spin-coating of electron-sensitive resist onto the substrate (2) Exposure to electron beam and subsequent fragmentation of exposed resist (3) Immersion in developer solution to remove exposed resist (4) Evaporation of metal layer onto developed and patterned resist (5) Lift-off of resist and undesired metal layer with suitable solvent (6) Sub-micron scale metal feature remains on substrate after lift-off.

In this Section, we develop an electron beam lithography (EBL) process for the fabrication of nanodiscs near a mirror. Although EBL is commonly used to fabricate periodically arranged nanostructures (refer literature review in Chapter 3), we choose to fabricate a pseudo-random array of nanodiscs. This is because the aim of this work is to facilitate a strategic experimental study of randomly arranged nanoparticles near a mirror, including the effect of spacer layer thickness on light-scattering. We have already highlighted the main disadvantages of the plasmonic mirror with self-organised metal islands in the literature review in Chapter 3 and the experimental study in Chapter 5 of this work. EBL helps to overcome the disadvantages by offering precise control of the nanoparticle morphology and surface coverage. Further, due to the high degree of control on the particle size and shape, we can expect to obtain sharper spectral features. This will enable a comparison of the trend in measured optical properties against single-particle FDTD simulations.

It must be noted that for application in solar cells, the spacer layer material between the nanodiscs and the plasmonic mirror must be a transparent conductive oxide. However, in this Chapter as we only focus on the optical properties of the plasmonic mirror, we use SiO_2 as the spacer layer material. We were restricted to using SiO_2 merely due to the availability of the material during the time of the experiment. Based on the simulation results in Chapter 4 and the results in Section 6.3 of this Chapter, we choose to use Ag nanodiscs of sizes in the order of 100nm to obtain high radiative efficiency in the visible-NIR wavelength region. Section 6.5 details the exact sizes of the nanodiscs used in the experimental studies.

For fabrication of nanoparticles using EBL, an electron beam (e-beam) is used to selectively pattern resists on the nanoscale. EBL, as opposed to optical lithography, facilitates nanoscale patterning as a result of the relatively short wavelength of electrons when compared to the wavelengths of visible light. The general steps of a conventional EBL process are outlined in Figure 6.6.

The substrate on which the sub-micron scale features are to be developed is first coated with a resist. The resist is a material which is sensitive to the e-beam; the molecular chains of resist materials such as poly(methyl methacrylate) (PMMA) or methyl methacrylate (MMA), both positive resists, upon e-beam exposure, undergo a process called chain scission to break up into smaller fragments [84]. This fragmentation process is used to pattern a resist with an electron beam, as shown in step 2 in Figure 6.6. The resist pattern can be pre-designed independently using a CAD tool and then processed into a compatible format to be loaded into the writing software for EBL. After exposure, the resist is immersed in a suitable developer solution to remove the exposed areas with the fragmented molecules of the resist. The resist is now 'patterned' as seen in step 3 of Figure 6.6. The metal layer is then deposited onto the patterned resist, which serves as a template for the designed sub-micron features. The patterned resist with the metal layer is then subjected to a suitable solvent which 'lifts off' or dissolves the resist and subsequently removes the undesired metal layers. At the end of the lift-off stage, only the sub-micron metal features remain on the substrate, as seen in step 6 of Figure 6.6. Appendix 2 describes the development of the *in-situ* EBL process with the detailed recipe used to fabricate Ag nanodiscs.

6.4.1 Patterning Nanodiscs using E-beam Lithography

A disc-shaped morphology was chosen for the plasmonic nanoparticles. Random arrays of Ag nanodiscs were fabricated on SiO_2 on a 130nm Ag substrate. The SiO_2 and the Ag film were deposited using electron beam evaporation. Electron beam lithography (EBL) using a

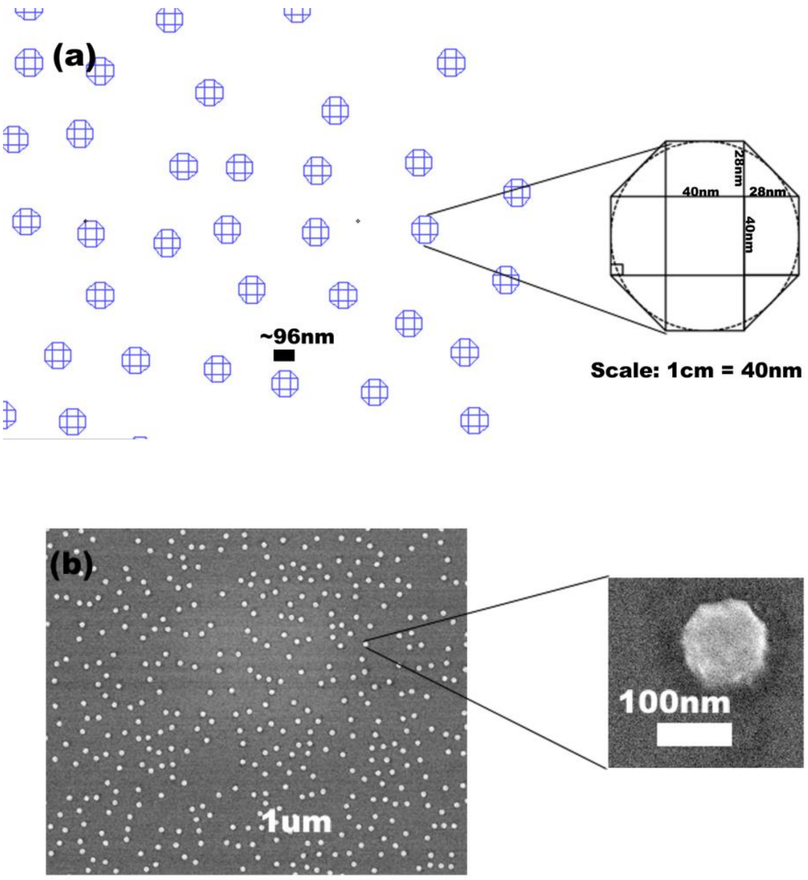

Figure 6.7 (a) Example of L-Edit design layout of randomly arranged octagons. Inset shows a to-scale (1cm = 40nm) example of an octagon designed for 100nm Ag nanodiscs. The dimensions of octagon need to be a multiple of the beam spot-size and hence the designed octagon will be slightly smaller/larger than the required nanodisc diameter – this can be adjusted for using a dose-level test (refer Appendix 2). **(b)** Corresponding fabricated sample 100nm Ag nanodiscs randomly arranged on a Si substrate at 6% surface coverage and dose level of 1305 μC/cm^2.

PMMA/MMA bilayer was used to pattern random arrays of nanodiscs on a given sample area (2mm x 2mm for samples used in optical measurements). The EBL-defined pattern was metallized with 2.5nm of Ti adhesion layer, followed by 50nm of Ag, using electron beam evaporation. The unexposed resist was lifted-off in Acetone to provide the resultant random array of Ag nanodiscs. The ‘nanodisc’ is essentially a cylinder with a defined diameter and a fixed height of around 50nm.

The nanodiscs were patterned using the conventional method by defining the cross sections as octagons; the magnified inset in Figure 6.7b shows an example of a Ag nanodisc with a diameter of 100nm, fabricated using the developed EBL technique. In this case, it is important that every side of the chosen octagon is a multiple of the beam spot-size as indicated in the to-scale example inset in Figure 6.7a.

The designed octagons were pseudo-randomly arranged in the CAD design using a modified version of the C-program-based algorithm by Dr. Tristan Temple (Macquarie University, Australia), which was initially used to randomly arrange square nanoparticles. Optical samples of randomly arranged nanodiscs were fabricated by tiling 50μm x 50μm pseudo-random arrays of nanodiscs on a 2mm x 2mm sample area. The program was configured to check for and avoid overlaps of nanodiscs on edges of the tiles. The minimum edge-edge separation was set to the disc diameter to avoid interparticle coupling effects [83]. Figure 6.7b shows an example of random 100nm nanodiscs at 6% surface coverage, fabricated on Si at an optimised dose level of 1305 μC/cm^2. A detailed description of the optimisation of dose level is given in the Appendix 2. Table 1 in Appendix 2 also details the optimisation of dose level for different surface coverages: 2%, 6%, 10% and 12% of nanodiscs. Due to the lack of interparticle coupling between the nanodiscs (as a result of the interparticle distance designed to be equal to the nanodisc diameter) we observed no significant effect on the spectral position of the plasmonic resonance with varying surface coverage from 2% to 12%. However, for surface coverages larger than 6%, there were complications in the lift-off stage of the EBL fabrication process – it was sometimes difficult to obtain a complete lift-off for nanodisc arrays with surface coverages of 10% and 12%. Hence, for all EBL samples fabricated in this work, we choose to use a nanodisc surface coverage of 6%.

6.5 Experimental Results

6.5.1 Effect of Varying the Nanodisc-Mirror Separation Distance

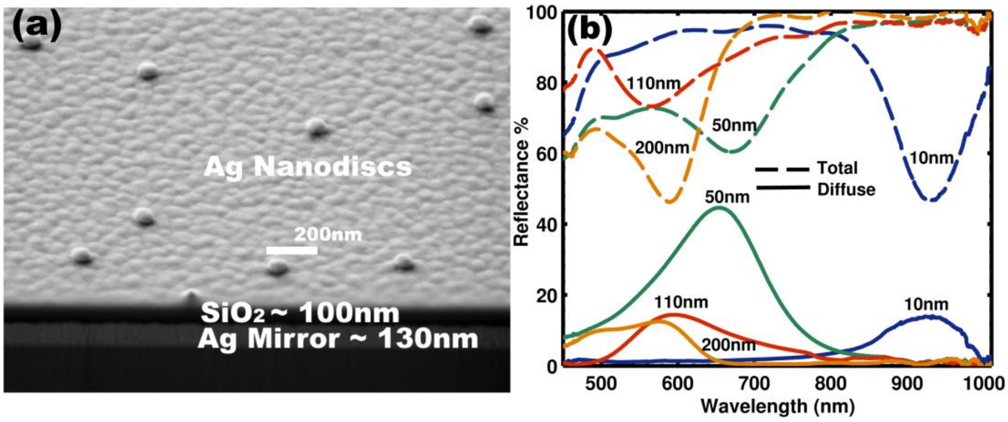

Figure 6.8 **(a)** Cross-sectional SEM image of a plasmonic mirror. **(b)** Optical characteristics of randomly arranged 100 nm Ag nanodiscs on varying thicknesses of SiO_2-on-Ag mirror.

To experimentally investigate the driving field effect, the SiO_2 thickness was varied from 10nm to 200nm, and nanodiscs with diameters of 100nm, 150nm, and 200nm were fabricated to provide a range of resonance positions. Figure 6.8a shows a cross-sectional SEM image of a fabricated plasmonic mirror sample.

The total and diffuse reflectance of the samples were measured using a white light supercontinuum (Fianium SC450, wavelength range: 450–2000nm) laser source and an integrating sphere connected to a spectrometer (B&W TEK). The sample was illuminated at 8^o to the sample normal and the diffuse reflectance was measured as the light scattered at angles greater than 8^o to the sample normal. Total reflectance is the sum of diffuse and specular reflectance. The spot-size of the laser beam was focused to be within the 2mm x 2mm sample area. A port-cap of the integrating sphere with a highly diffuse-reflective Spectraflect coating on the interior, exhibiting a reflectance greater than 95% over the wavelength range of 400-1000nm, is used as the reflectance calibration standard[16]. In order to ensure reliable measurements, we experimentally measured the total and diffuse

---

[16] For details on the Spectraflect coating on the interior of the integrating sphere kindly refer to the product details online: www.labsphere.com/products/reflectance-materials-and-coatings/white-coatings/spectraflect.aspx (Accessed: April 2011).

reflectance for a piece of bare polished Si and verified that there is a good agreement between the experimental results and the known reflectance of Si simulated using the optical constants tabulated by Palik [86].

Figure 6.8b illustrates the spectral features of the total and diffuse reflectance for a plasmonic mirror with 100nm Ag nanodiscs on varying thicknesses of SiO_2. Metal nanoparticles both absorb and scatter light, leading to troughs in the total reflectance and peaks in the diffuse reflectance, respectively. The spectral position and the line shape of the peaks and troughs are highly sensitive to the spacer layer thickness (Figure 6.8b). For 100nm nanodiscs, increasing the spacer thickness from 10nm to 200nm results in a spectral blue shift of the peak diffuse reflectance from 950nm to around 600nm (Figure 6.8b).

6.5.2 Effect of Varying the Size of the Nanodisc

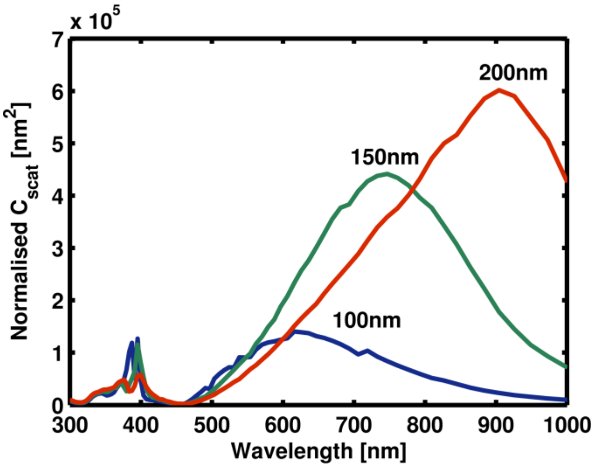

Figure 6.9 Simulation of the normalised scattering cross section C_{scat} [nm^2] for single Ag nanodiscs of 100-, 150-, and 200nm-diameter, on 110nm SiO_2-on-Ag mirror.

The plasmonic mirror can be integrated at the rear of a thin μc-Si solar cell to scatter light in the near-bandgap region of around 600-1100nm. For photovoltaic applications, it would be desirable for the plasmonic mirror to exhibit high scattering (diffuse reflectance) in the required wavelength range with low broadband absorption losses. Additionally, based on the review of plasmonic solar cells in Chapter 3, it would also be beneficial for the mirror to scatter light over a broad range of large angles.

For long-wavelength light scattering, we initially consider a SiO_2 thickness of 110nm so that $|\mathbf{E}|^2$ peaks in the near-infrared (NIR) at a wavelength of around 850nm (refer Figure 6.2). Simulations in Figure 6.9 show the effect of increasing nanodisc diameter on the peak C_{scat} value, for the mirror with a nanodisc on 110nm SiO_2. As the diameter is increased from 100 to 200nm, the peak value of the C_{scat} increases due to a red-shift of the plasmonic resonance peak. The C_{scat} also red-shifts to a wavelength of 900nm with no significant loss in the spectral scattering bandwidth.

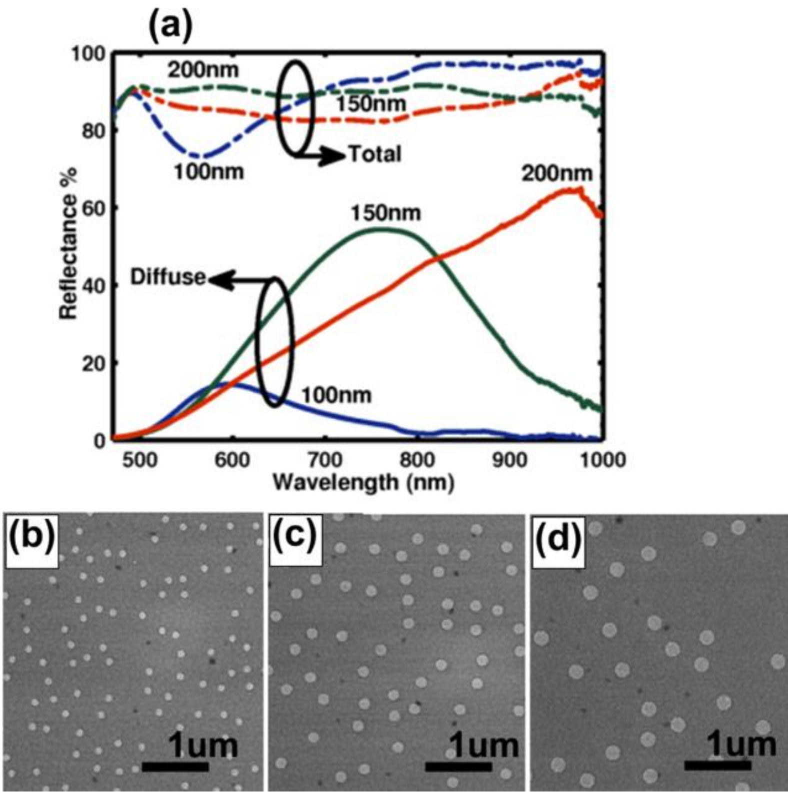

Figure 6.10 (a) Optical characteristics and **(b-d)** SEM images of random arrays, of 100-, 150-, and 200-nm-diameter nanodiscs, respectively, on 110 nm SiO_2-on-Ag mirror.

Comparing Figures 6.9 and 6.10a, the diffuse reflectance spectra for 100- , 150- , and 200nm-diameter nanodiscs on 110nm SiO_2, show good agreement with the simulated trends in the magnitude and peak position of the scattering cross-section. Additionally, Figure 6.10a indicates that the broadband total reflectance value increases with increasing nanodisc diameter. This is an encouraging trend for scattering applications, where low parasitic absorption losses are desired. Figures 6.10 (b-d) show the SEM images for the fabricated 100-, 150- and 200nm-diameter nanodiscs on 110nm SiO_2.

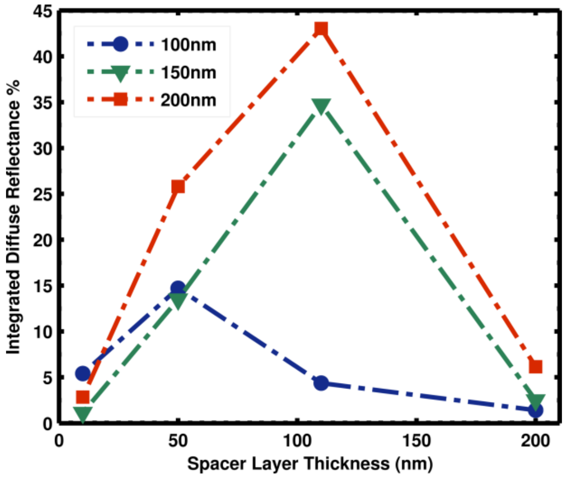

Figure 6.11 Diffuse reflectance integrated over the near-infrared, 600-1000nm wavelength range for plasmonic mirror samples with 100nm, 150nm and 200nm discs, at 6% surface coverage, on varying thicknesses of SiO_2-on-Ag mirror substrate

For a given nanodisc diameter, the measured integrated diffuse reflectance (in the 600-1000nm wavelength range) shows a strong dependence on the spacer thickness (Figure 6.11). For each diameter, there is an optimum thickness at which the integrated diffuse reflectance reaches a maximum value. At a given spacer thickness, the magnitude of the integrated diffuse reflectance increases with the nanodisc diameter (except for the 10nm SiO_2 case). However, when the thickness is 200nm, the spacer thickness has a greater influence than the nanodisc diameter. This is clearly illustrated in Figure 6.11, where, at a thickness of 200nm, despite doubling the diameter of the nanodiscs, the increase in diffuse reflectance is relatively minimal.

6.5.3 Plasmonic Mirror versus Conventional Textured Ag Mirror

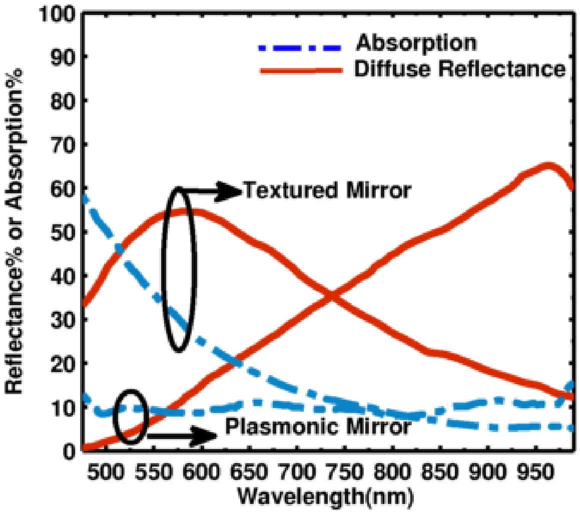

Figure 6.12 Optical characteristics of the optimised plasmonic mirror with 6% surface coverage of 200 nm Ag nanodiscs on 110 nm SiO_2 compared to the conventional textured mirror fabricated by Sai *et al.* by depositing 200nm of Ag onto an Asahi-U TCO substrate [20].

In this particular experiment, the mirror with 200-nm-diameter Ag nanodiscs on a 110nm SiO_2 spacer appears to be optimum for NIR light scattering applications with a 65% peak diffuse reflectance at a wavelength of around 950nm, and a broadband total reflectance above 80%. Figure 6.12 shows the comparison of the diffuse reflectance and absorption characteristics of the plasmonic mirror with the corresponding spectral data for a conventional textured mirror fabricated by depositing 200nm of Ag onto an Asahi-U type TCO substrate. The textured mirror is the conventional light-trapping component used in thin silicon solar cells. Note that the spectral data for the textured mirror has been obtained by the digitisation[17] of published results in a recent study by Sai *et al.* [20]. The fabrication and characterisation of the textured mirror by Sai *et al.* has also been discussed in Chapter 5, in more detail. The Asahi-U texture has a σ_{rms} of 30nm [20].

In Figure 6.12, the optimized plasmonic mirror with a significantly lower σ_{rms} of 13.5 nm, outperforms the textured mirror in the NIR region of by exhibiting a higher NIR diffuse reflectance beyond 750nm with a maximum reflectance of approximately 65%

---

[17] The digitisation of the graph from the paper by Sai *et al.* [20] was done using a freely available digitiser developed by Ankit Rohatgi: http://arohatgi.info/WebPlotDigitizer.

around 950nm. As the σ_{rms} of the plasmonic mirror is much lower than that of the textured mirror, it can be concluded that the significantly high NIR diffuse reflectance is mainly due to enhanced plasmonic scattering by the Ag nanodiscs near the mirror. Further, the plasmonic mirror with the 200nm nanodiscs also exhibits low broadband absorption losses; the parasitic absorption loss is significantly less than the textured mirror in the short-wavelength region and comparable to the absorption characteristics of the textured mirror beyond a wavelength of 800nm.

6.5.4 Angular Scattering Properties of the Plasmonic Mirror

In order to investigate wide-angle scattering properties, we analysed the plasmonic mirror samples using a custom-made Wavelength-Angle Resolved Scattering (WARS) system [85]. A white light supercontinuum (Fianium SC450, wavelength range: 450–2000 nm) laser source is used to illuminate the plasmonic mirror sample at normal incidence. The light scattered by the sample is collected by a mini integrating sphere which spans the angular range from 5^o to 80^o as measured from the sample normal. As the sample consists of randomly arranged nanodiscs, it is assumed to exhibit uniform scattering properties over the 5^o to 160^o angular range [85]. A BWTEK spectrometer with a wavelength range of 450nm to 900nm is used to analyse the scattering spectrum. The details of the experiment and measurement technique can be found in [85] by Payne *et al*. Here we will focus on the analysis of the results obtained using the WARS system. Figure 6.13(a-c), clearly indicate the effect of varying the spacer thickness on the wavelength-angle resolved scattering properties of the plasmonic mirror with 100nm nanodiscs. The wide-angle scattering properties of the mirror are maintained as the spacer thickness is increased from 10nm to 110nm. The trend in the scattering intensity and spectral bandwidth of the scattering peak shows a very good correlation with the integrating sphere measurements of the same parameters (cf. Figures 6.8b and 6.13(a-c)). At ultra-thin separation distances, although the mirror exhibits wide-angle scattering with high scattering intensity, the resonance peak exhibits a very narrow spectral bandwidth. The 100nm nanodiscs exhibit maximum scattering intensity and spectral bandwidth (approximately 550-750nm) over a wide angular range, at a distance of 50nm from the Ag mirror. The nanodiscs with a diameter of 200nm also show consistent wide-angle scattering for spacer thickness from 10-110nm. As in the case of the random array of 100nm nanodiscs, the 200nm nanodiscs also exhibit

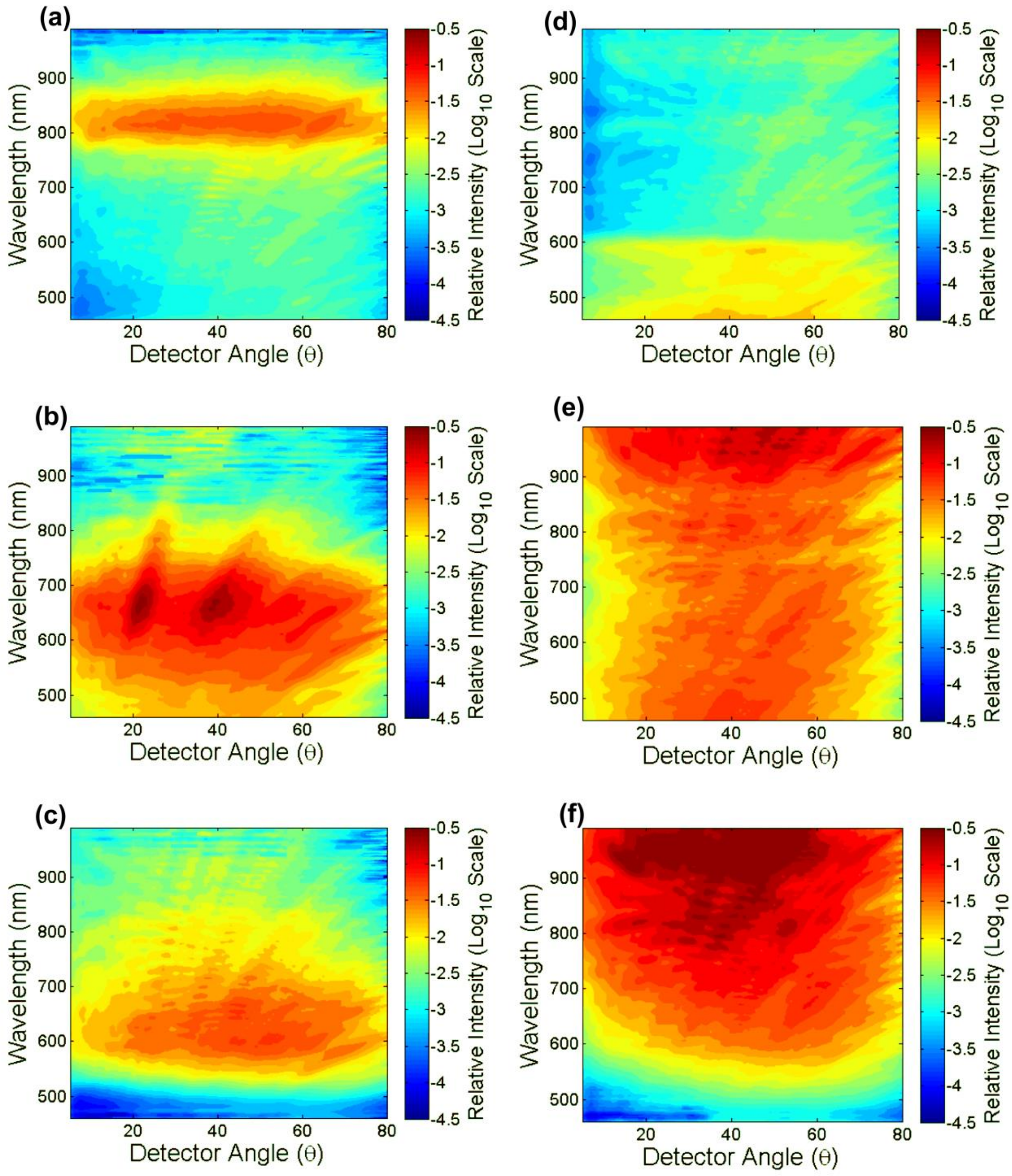

Figure 6.13 Wavelength-angle resolved scattering properties for random arrays of: **(a-c)** 100nm discs near a Ag mirror coated with 10-, 50- and 110nm of SiO_2 , respectively and **(d-f)** 200nm discs near a Ag mirror coated with 10-, 50- and 110nm of SiO_2 , respectively.

a clear dependence of scattering intensity and peak scattering bandwidth with spacer thickness (Figure 6.13(d-e)). Interestingly, doubling the size of the nanodiscs from 100nm to 200nm, at 6% surface coverage results in a significant widening the peak scattering bandwidth from 450-950nm, while maintaining high scattering intensity and wide-angle scattering.

6.6 Conclusion

We have demonstrated using FDTD simulations that the driving field for a plasmonic nanodisc near a mirror can be spectrally tuned by varying the disc-mirror separation distance and the material type of the mirror and the spacer layer. The driving field strongly influences the spectral properties of the scattering cross-section for a nanodisc-near-mirror structure. We used e-beam lithography to fabricate a plasmonic mirror with pseudo-random arrays of Ag nanodiscs. The optical scattering properties of the mirror can be tuned by varying the thickness of the spacer layer. Additionally, to maximize scattering, the nanodisc size must be tuned such that the plasmonic resonance peak coincides with the peak of the driving field intensity in the required spectral range. Our optimized plasmonic mirror with low broadband absorption losses and a high diffusive reflectivity in the NIR over a broad angular range, is a promising system for light-scattering applications in µc-Si:H solar cells. The broadband absorption loss in the mirror can be lowered given the development of an adhesion-free EBL process; such an improvement has the potential to further reduce the parasitic absorption losses in the plasmonic mirror when compared to the losses in conventional textured mirror substrates. The dependence of the surface coverage of nanodiscs on the optical behaviour of the plasmonic mirror is an additional area of interest for future experiments.

[This page intentionally left blank]

Chapter 7

Microcrystalline Silicon Solar Cell with an Integrated Plasmonic Mirror

(Publication of results in this Chapter: in progress as of April 2014)

7.1 Introduction

In Chapter 6, we developed a plasmonic mirror with pseudo-randomly arranged Ag nanodiscs for purposes of NIR light-scattering. The optimised mirror showed low broadband absorption losses and a high diffusive reflectivity in the NIR region, over a broad angular range. These characteristics make the plasmonic mirror a promising candidate for light-scattering applications in thin film solar cells.

As reviewed in Chapter 3, thin microcrystalline silicon (μc-Si) solar cells require optical absorption enhancement in the near-bandgap, near-infrared wavelength region from around 700nm to 1150nm. To date there have been experimental studies on using plasmonic gratings [19] and metal island films [24] as efficient light-trapping components at the rear of thin μc-Si:H solar cells. In this Chapter we aim to enhance the optical absorption in μc-Si:H solar cells by using the light-scattering properties of the plasmonic mirror with Ag nanodiscs. In the first part of this Chapter we use FDTD simulations to briefly study the influence of a nearby Si layer on the scattering cross-section of a nanodisc-near-mirror system. In the second part of this Chapter, we fabricate an n-i-p μc-Si:H solar cell with the plasmonic mirror integrated at the rear of the device. We study and compare the optical and electrical properties of the plasmonic solar cell with its planar counterpart and a solar cell deposited on a conventional textured surface. In addition to this, we also study the effect of varying the nanodisc-mirror separation distance on the optical and electrical performance of the n-i-p μc-Si:H solar cell.

7.2 Simulation Results

In this Section, we will study the effect of a nearby Si layer[18] on the scattering cross section of a Ag nanodisc-near-Ag mirror structure. However, before introducing the Si layer, we will simulate the optical behaviour of the Ag nanodisc-near-Ag mirror structure (with ZnO as the spacer layer material) in air. The Ag disc has a diameter of 150nm and a height of 50nm. The optical constants for Ag were obtained from the tabulated data by Johnson and Christy [76] and the optical constants data for ZnO has been provided by Dr. Fujiwara of AIST, Tsukuba, Japan. The calculation of C_{scat} using the FDTD simulation method has already been explained in detail in Chapter 4 and Chapter 6.

7.2.1 Optical Behaviour of the Plasmonic Mirror in Air

In this Section we aim to briefly analyse the optical behaviour of the mirror in air. First, we will simulate the C_{scat} of the nanodisc on a semi-infinite ZnO layer, *without* the presence of the Ag mirror: we term the C_{scat} calculated in this manner as the *intrinsic* C_{scat}. In this case, the resonance is principally excited by the incident field and the peak intrinsic C_{scat} value occurs at a wavelength of around 760nm (Figure 7.1a).

Next, we introduce the Ag mirror and simulate the electric field intensity, $|\mathbf{E}|^2$ for varying ZnO spacer thicknesses on the Ag mirror. Note that $|\mathbf{E}|^2$ is simulated only for the ZnO/Ag mirror structure i.e. without the Ag nanodisc. As seen in Figures 7.1(b-d), the peak $|\mathbf{E}|^2$ red-shifts with an increase in the spacer layer thickness without any significant changes in the magnitude.

In Chapter 6, we observed that $|\mathbf{E}|^2$ has a strong influence on the C_{scat} of a nanodisc-near-mirror structure. The peak value of the C_{scat} can be maximised if the spacer thickness is tuned, such that, the spectral position of the peak $|\mathbf{E}|^2$ coincides with the position of the peak *intrinsic* C_{scat} of the nanodisc. In figures 7.1(b-d) it can be seen that peak C_{scat} follows the trend in $|\mathbf{E}|^2$ and also exhibits a gradual red-shift with spacer thickness. The maximum value for the C_{scat} occurs at a nanodisc-mirror separation distance of 70nm.

---

[18] The Si layer is chosen to be semi-infinite so that complex optical phenomena such as interference fringes are avoided to aid a better understanding of the simulation results.

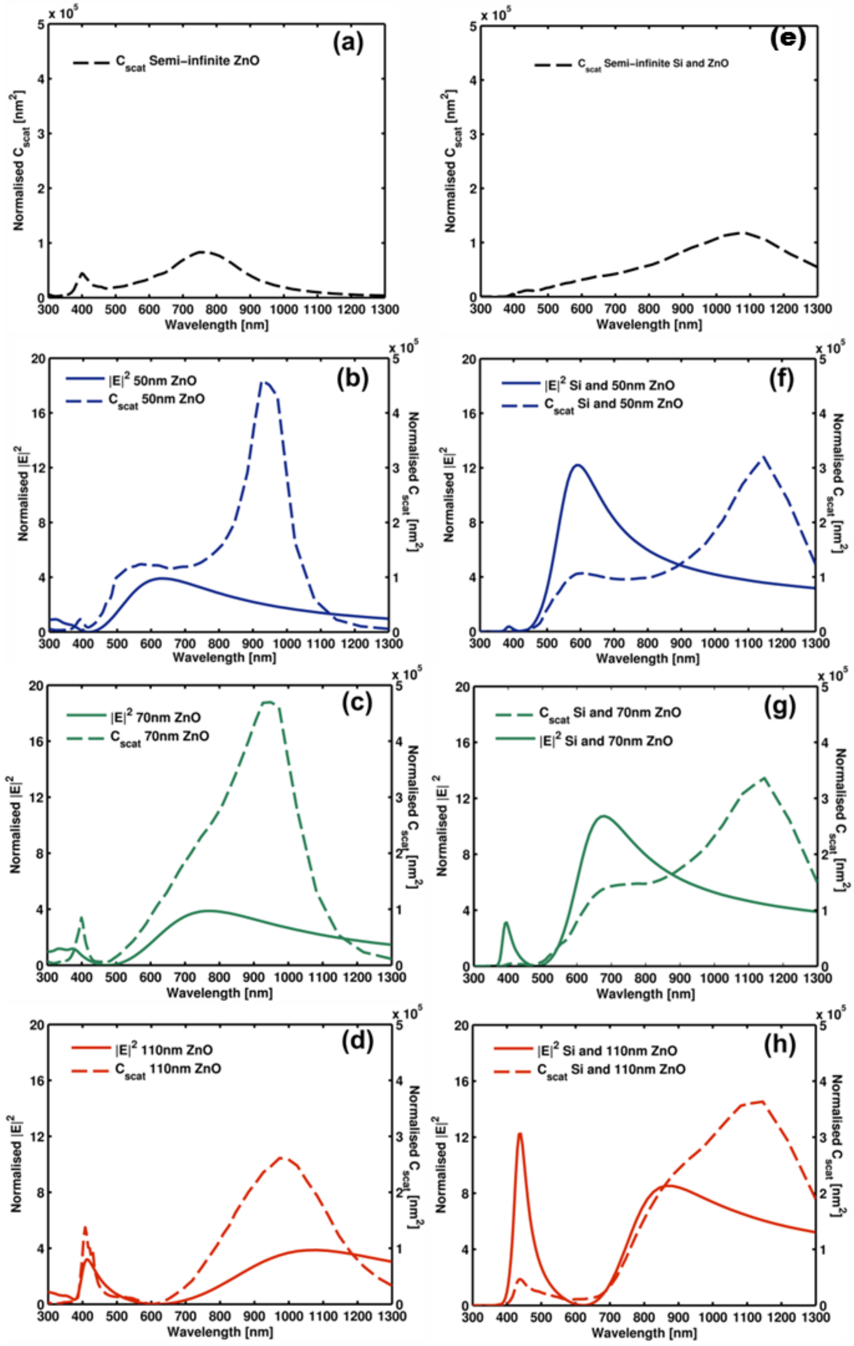

Figure 7.1 FDTD simulation results for: **Mirror in air:** **(a)** Normalised C_{scat} [nm^2] for a Ag nanodisc with 150nm diameter and 50nm height, on a semi-infinite ZnO substrate. **(b-d)** **|E|**^{2} is calculated at 25 nm above the ZnO-on-Ag mirror, without the nanodisc (solid red line), on 50nm, 70nm and 110nm ZnO, respectively. **|E|**^{2} is calculated 25nm from the ZnO surface as this distance corresponds to the centre of the plasmonic nanodisc of height 50nm. Corresponding normalised C_{scat} [nm^2], for the respective configurations, with the nanodisc are plotted as dotted lines. **Mirror near Si:** **(e)** Normalised C_{scat} [nm^2] for the Ag nanodisc embedded in a finite ZnO layer, on Ag mirror, near a semi-infinite Si layer. **(f-h)** **|E|**^{2} for Si/ZnO/Ag mirror (solid red line), without nanodisc for 50nm, 70nm and 110nm ZnO, respectively. Corresponding normalised C_{scat} [nm^2], for the respective configurations, with the nanodisc are plotted as dotted lines.

7.2.2 Optical Behaviour of the Plasmonic Mirror near a Si layer

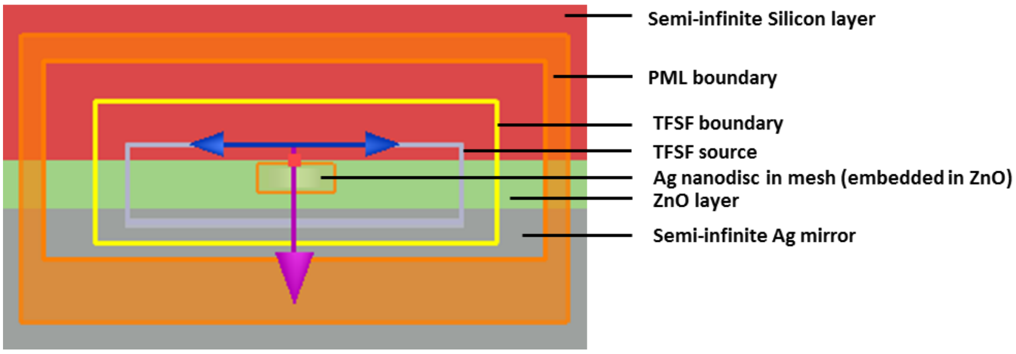

Figure 7.2 2D cross-section of the simulated Si/ZnO/Ag structure with the Ag nanodisc at the rear.

In this Section we will introduce the Si layer near the plasmonic mirror. Figure 7.2 shows a 2D cross-section of the simulated Si/ZnO/Ag structure with the nanodisc embedded in the ZnO layer. There is a thin 'capping' layer of ZnO above the nanodisc to avoid direct contact with the Si layer.

The TFSF source is incident from within the Si layer. The distance from the point-of-incidence of the TFSF source and the surface of the embedded Ag nanodisc is around 40nm from the Si/ZnO interface, in order to minimise absorption of short-wavelength photons in the Si layer. This helps to obtain reliable values of C_{scat} even in the short-wavelength range. The optical constants data for Si are obtained from the tabulated data by Palik [86].

Figure 7.1e shows the *intrinsic* C_{scat} spectrum for the structure comprising of semi-infinite Si on a nanodisc embedded in semi-infinite ZnO. Comparing Figures 7.1e and 7.1a, the peak intrinsic C_{scat} experiences a strong red-shift from a wavelength of 750nm to around 1080nm with the introduction of the Si layer.

Next, we introduce the Ag mirror. The peak $|\mathbf{E}|^2$ is simulated only for the Si/ZnO/Ag mirror structure, without the presence of the Ag nanodisc. The peak $|\mathbf{E}|^2$ exhibits an overall spectral red-shift and a decrease in magnitude with the thickness of the spacer layer (Figure 7.1(f-h)). Comparatively, for the mirror in air, the peak $|\mathbf{E}|^2$ did not show any significant changes in magnitude when the thickness of the spacer layer was increased (refer Figures 7.1 (b-d)).

The spectral dependence of C_{scat} on $|\mathbf{E}|^2$ is maintained for the plasmonic mirror near a Si layer. However, the thickness of the spacer layer required for maximising the value of the C_{scat}, is much larger for the mirror near Si when compared to the mirror in air (c.f. Figures 7.1c and 7.1h). This is due to the strong red-shift in the peak intrinsic C_{scat} with the introduction of Si. As the peak $|\mathbf{E}|^2$ red-shifts with thickness of the spacer layer, a much larger value of spacer thickness is required in order to tune the spectral peak position of the $|\mathbf{E}|^2$ near the peak intrinsic C_{scat}.

Hence, the simulations results demonstrate that at a given nanodisc-mirror separation, the peak C_{scat} position is significantly red-shifted with the introduction of the Si layer, when compared to the mirror in air. The spectral dependence of C_{scat} on $|\mathbf{E}|^2$ is maintained for plasmonic mirror near the Si layer. The optimum thickness of the spacer layer, for maximum peak C_{scat} magnitude, is larger for the mirror near Si when compared to the mirror in air.

7.3 Fabrication

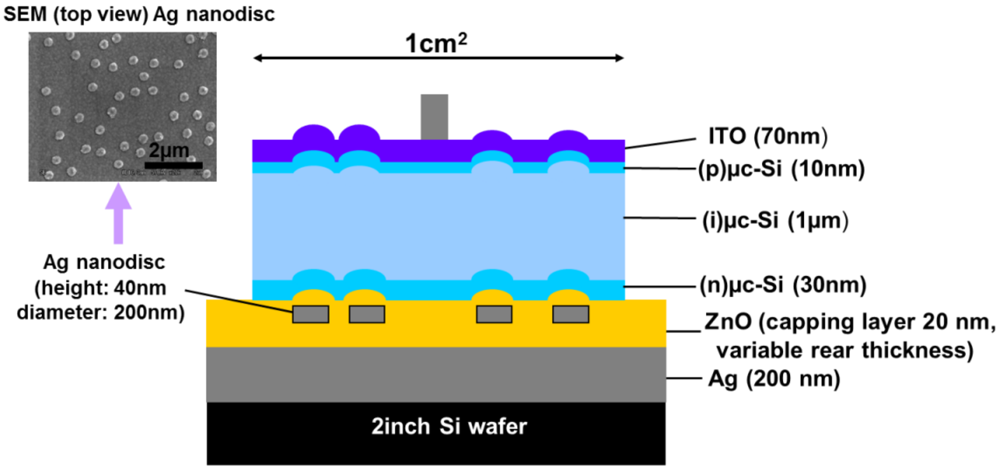

Figure 7.3 Cross-section schematic of the fabricated n-i-p μc-Si:H solar cell with the plasmonic mirror at the rear.

Thin μc-Si:H solar cells with the plasmonic mirror structure at the rear, were fabricated and characterised as part of a placement funded by a JSPS fellowship, at the National Institute of Advanced Industrial Science and Technology (AIST) in Tsukuba, Japan. The project was collaboration between AIST and the Southampton Nanofabrication Centre (SNC), University of Southampton, Southampton, U.K.

Figure 7.3 shows a cross-section schematic of the fabricated n-i-p μc-Si:H solar cell with the plasmonic mirror at the rear. The ZnO-on-Ag substrates were fabricated at AIST and shipped to SNC for fabrication of random arrays of Ag nanodiscs using the EBL process described in Chapter 6 and Appendix 2.

For preparation of the substrate, the 200nm Ag mirror was deposited using DC-sputtering of a Ag target onto a 2-inch Si wafer, at 200 W and Ar flow rate at 200sccm, for 6min. The 2-inch Si wafer merely serves as a substrate and does not influence the electrical or optical properties of the final device. The Ga:ZnO layer, which functions as the rear spacer layer between the Ag nanodiscs and Ag mirror, was deposited by DC-sputtering a ZnO target at 200 W with an Ar flow rate of 200sccm. The deposition time was varied according to the desired ZnO spacer thickness. In this experiment, three different thickness of rear ZnO spacer layer: 70nm, 90nm and 110nm were deposited by sputtering for 210s, 270s and 300s, respectively. A table with the details of the samples prepared in this experiment is included later in this Section. All sputtering was done in a model SBR-2306 ULVAC sputterer at a pressure of approximately 1x 10^{-5} Torr.

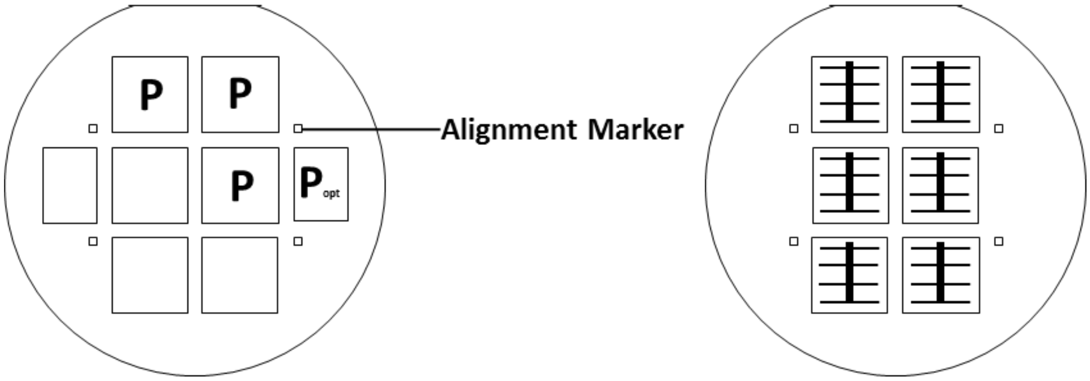

Figure 7.4 To-scale images of masks used for deposition of **(a)** ITO and **(b)** Ag grid contacts

Figure 7.4a and 7.4b represent to-scale images of masks used for deposition of ITO and Ag grid contacts, respectively, in the later stages of cell fabrication. The ITO mask was also used as a template in the EBL process to define the cell areas to be patterned with random arrays of Ag nanodiscs. In Figure 7.4a, the letters are used merely as labels to aid explanation in this Section. The letter 'P' indicates the cell areas patterned with Ag nanodiscs. P_{opt} indicates an area of 1.0cm x 0.70cm patterned with Ag nanodiscs, for purposes of optical measurements only. Ag nanodiscs with a diameter of 200nm and height of 40nm were fabricated in random arrays in the areas labelled with letters 'P' and 'P_{opt}' in Figure 7.4a. The interparticle distance was set to the nanodisc diameter. Details of the EBL procedure are discussed in Chapter 6 and the Appendix 2.

The remaining squares in Figure 7.4a, define the locations of the reference devices (1.0cm x 1.0cm) and the reference optical sample area (1.0cm x 0.70cm) without any nanodiscs. Hence on each 2-inch substrate with a given rear ZnO thickness, there are three identical plasmonic devices and three identical non-plasmonic or *planar* devices. In addition to this, on the same substrate, there is one plasmonic sample area and one *planar* sample area, without any Ag grid contacts, for purposes of optical measurements.

EBL was also used to define alignment markers as indicated in Figure 7.4a, the positions of which correspond with the alignment marker positions in the ITO and Ag grid contact masks. This ensures good alignment of the EBL-patterned areas with the cell areas defined by ITO and Ag grid contact masks in the later stages of fabrication. The fabrication of the plasmonic and planar devices on the same substrate, under the same deposition conditions, allows for a fair comparison of the corresponding electric and optical properties of these devices.

After EBL patterning, the 2-inch substrate is sputtered with a 20nm layer of Ga:ZnO. In the case of the patterned areas, the 20nm Ga:ZnO layer is defined as the 'capping layer' on the nanodiscs to prevent direct contact between the μc-Si:H layer and the metal nanodiscs. Without a capping layer, the metal nanodiscs may behave as recombination centres when placed in direct contact with the μc-Si:H layer, leading to a deterioration in the electrical performance of the device.

Subsequently an n-i-p μc-Si:H layer structure was deposited using a RF plasma-enhanced chemical vapour deposition (PECVD) system. The deposition of the n-i-p μc-Si:H was performed by Dr. Hitoshi Sai at AIST. The details of the deposition procedure are mentioned by Sai *et al.* [20] in a recent paper on light-trapping in textured μc-Si:H solar cells. However, the details of the recipe are included again in this Section for sake of completeness. The thicknesses of the n-, i- and p- layers were 30nm, 1μm and 10nm, respectively, in that order of deposition. The μc-Si:H i-layer was deposited using a mixture of SiH_4/H_2 [10.5:380 SCCM(SCCM denotes cubic centimetre per minute at STP)] under a pressure of 1.5 Torr and a temperature of 170 °C. For p- and n-type doping, B_2H_6 and PH_3 gases were added to SiH_4 and H_2, respectively [20].

The next stage involves the deposition of a 70nm ITO layer by RF sputtering of an ITO target onto the substrate, through the shadow mask in Figure 7.4a, at a power of 100W for 11min, under Ar and O_2 flow rates of 200sccm and 1.5sccm, respectively. The cells were then isolated by reactive-ion-etching and Ag finger grid contacts were deposited by sputtering through the mask in Figure 7.4b. The resulting active area of the electrical device is $1cm^2$. The Ag grid mask in Figure 7.4b, ensures that grid contacts are not deposited on the 1.0cm x 0.70cm sample areas which are used for optical measurements. The final stage of the fabrication process involves post-annealing of the cell at 175^oC for 2 hours in a vacuum oven.

7.4 Optical and Electrical Characterisation

The plasmonic and planar optical samples (co-deposited with the electrical devices, but without the electrical grid contacts) were measured for total reflectance using a Perkin-Elmer Lambda 950 spectrophotometer fitted with a 150mm diameter Lab-Sphere integrating sphere. The performance of the plasmonic and planar solar cells was evaluated using J-V and EQE (external quantum efficiency) measurements. J-V measurements were conducted with a system consisting of a Keithley Series 2400 Source Measure Unit (SMU) and a solar simulator with an AM1.5 filter and intensity of $100mW/cm^2$. EQE measurements were also obtained by using the spectrally filtered output of a tungsten halogen lamp source and without implementing any voltage or light bias. Appendix 3 details the main steps involved in an EQE measurement. Measurements were made over a 300nm to 1200nm wavelength range, in 10nm step sizes. A 4-point probe contact technique was used for both the J-V and EQE measurement systems.

7.5 Experimental Results

In this Section, we experimentally investigate the potential of the plasmonic mirror as a NIR-light trapping component for thin n-i-p μc-Si:H solar cells. The EBL-defined plasmonic mirror is integrated into the rear of a thin n-i-p μc-Si:H solar cell, as described in the earlier Sections of this Chapter.

Sample	**Device Type**	**Total rear ZnO thickness (nm)**
A	Plasmonic	90nm: 20nm Capping + 70nm disc-mirror
	Planar	90nm
B	Plasmonic	110nm: 20nm Capping + 90nm disc-mirror
	Planar	110nm
C	Plasmonic	130nm : 20nm Capping + 110nm disc-mirror
	Planar	130nm

Table 7.1 Summary of the fabricated solar cells. An additional device D, was also co-deposited on a substrate of 200nm Ag on textured Asahi-U transparent conducting oxide (SnO2:F).

The aim of the experiment is two-fold : (i) to evaluate whether the plasmonic solar cell provides a higher short-circuit current density and higher efficiency due to better optical performance in the NIR, when compared to a solar cell with a planar mirror and no nanodiscs (ii) to evaluate the influence of changing the rear ZnO thickness, i.e. the nanodisc-mirror separation distance, on the optical and electrical performance of the thin plasmonic n-i-p μc-Si:H solar cell.

Table 7.1 shows a summary of the fabricated devices. We use plasmonic devices **A**, **B** and **C**, to evaluate the effect of changing the disc-mirror separation on optical and electrical performance of the device, by varying the disc-mirror separations as: 70nm, 90nm and 110nm, respectively. The thickness of the ZnO capping layer (i.e. separation between Si and the nanodiscs) on the plasmonic mirror is kept constant at 20nm in all devices. As indicated in Table 7.1 and detailed in Section 7.3, planar devices without any nanodiscs were co-deposited on the same substrate as the plasmonic device. In order to further compare the light-trapping behaviour of a device with plasmonic mirror to a device on a conventional textured substrate, an additional device **D**, was also co-deposited on a substrate of 200nm Ag on textured Asahi-U transparent conducting oxide (SnO_2:F).

7.5.1 Analysis of TEM cross-section images and AFM results

Figure 7.5 shows TEM cross-section images obtained for device set A, with the planar device in Figure 7.5a (zoomed version of the highlighted rear section in Figure 7.5d), plasmonic device in Figure 7.5b (zoomed version of the highlighted rear section in Figure 7.5e), and device D in Figure 7.5c (zoomed version of the highlighted rear section in Figure 7.5f). For the plasmonic device, we observe that the sputtered, thin ZnO capping layer forms a good continuous conformal coating on surface of the nanodisc. Also, the measurements of the nanodisc in the TEM image (Figure 7.5e) indicate that the surface morphology of the nanodisc, i.e. the disc diameter and height are not significantly affected as a result of the bottom-up device fabrication processes which follow the plasmonic mirror fabrication stage. The TEM cross-sections for solar cells fabricated on the planar, plasmonic and textured substrates indicate a 'natural' texture formation on the front of the devices. This is due to the morphological characteristics of the rear substrate being transferred, by a certain extent, onto the front surface as a result of conformal growth of the thin film solar cell. Although the TEM images indicate a front-texture formation, it is difficult to even qualitatively distinguish the difference in front surface roughness between the devices, by merely examining the TEM images. Hence an AFM analysis is performed to characterise the front surface and measure the root mean square surface roughness (σ_{rms}) of the three devices, the results of which are shown in Figures 7.5g to 7.5i. In the AFM images, the colour gradation is used to give an idea of the height of the surface features, with a lighter shade of colour indicating an increase in the height of the observed features.

A close observation of the AFM images 7.5g and 7.5h indicates that the plasmonic device (Figure 7.5h) consists of two main regions: a darker region indicating features of heights similar to that in the planar device and lighter regions indicating higher surface features. The regions with the higher surface features appear to be dispersed and have a maximum height of 150nm, which is 38nm higher than the maximum height of the surface features in the planar device. These two observations indicate that the higher surface features on the plasmonic device are most probably due to a direct transfer of the surface characteristics of randomly arranged Ag nanodiscs with a height of approximately 40nm on the rear substrate. The AFM image for device D on the other hand, indicates maximum

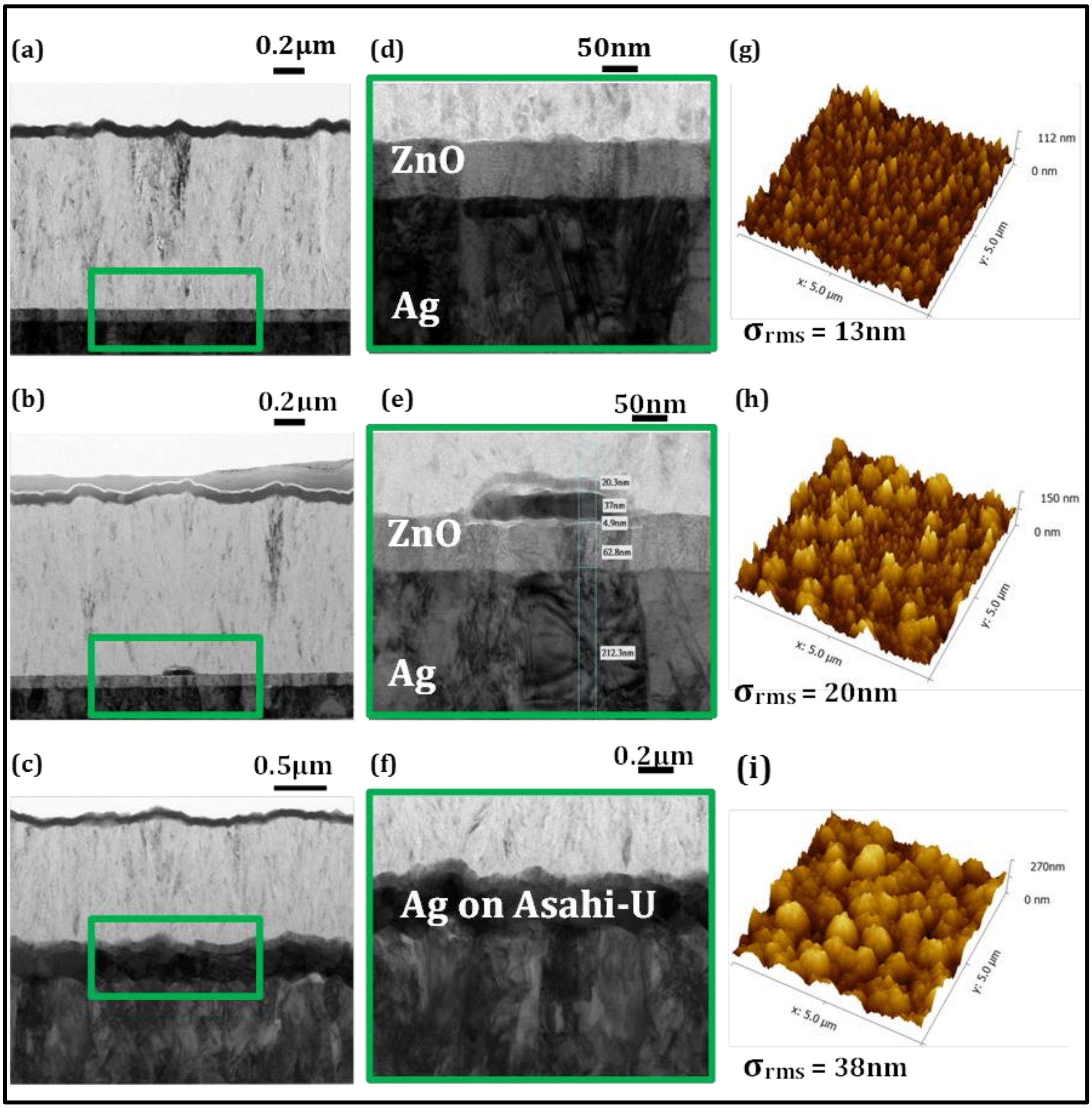

Figure 7.5 TEM cross-section images of **(a)** planar device A **(b)** plasmonic device A **(c)** device D fabricated on conventional textured mirror substrate. **(d-f)** Zoomed TEM cross-section images of the highlighted (in green) device sections in Fig 7.5 a-c. **(g-i)** AFM images and corresponding root mean square surface roughness (σ_{rms}) measurements for the devices in Fig. 7.5 (a-c).

surface feature height of 270nm with the front surface exhibiting no sign of features similar to that of the planar substrate.

The σ_{rms} of the front surface texture for the plasmonic device is around 20nm which slightly higher than the corresponding σ_{rms} value of 13nm for the planar device. On the other hand, Device D has a σ_{rms} value of around 38nm which is almost three times the surface roughness of the planar device. It was reported earlier in this work that the plasmonic mirror substrate (prior to deposition of the solar cell) has a σ_{rms} value of around 13.5nm. The typical value for the σ_{rms} of Asahi-U type substrates is around 30nm [20]. As will be seen in Sections 7.5.4 and 7.5.5 of this Chapter, knowledge of the front surface roughness (and roughness of the rear substrate) will be useful when comparing the performance of the plasmonic device with the device fabricated on a textured substrate.

7.5.2 Electrical performance summary of the fabricated solar cells

Figure 7.6 shows a summary of the measured short circuit current density (J_{sc}), open-circuit voltage (V_{oc}) and the conversion efficiency (η) values for the devices listed in Table 7.1. The plasmonic solar cells, for all the disc-mirror separation distances, have higher J_{sc}, V_{oc} and η values when compared to their planar cell counterparts. The η of the plasmonic solar cells is almost comparable, (in fact higher for the case of plasmonic device A), to that of the device fabricated on a conventional textured substrate. Although the plasmonic solar cells have a higher V_{oc} than the device fabricated on a textured substrate, the J_{sc} of the plasmonic devices is lower than the J_{sc} of the device on textured substrates. It can also be observed that despite changing the disc-mirror separation distances, the relative increase in the J_{sc}, V_{oc} and η parameters of the plasmonic devices A, B and C over their planar device counterparts is similar across the device sets. As detailed in Section 7.3 and Figure 7.4, for each sample type: A,B and C, three identical plasmonic devices and three identical planar counterparts were fabricated. Hence, the error bars in Figure 7.6 represent the standard deviation from the mean for the values of J_{sc}, V_{oc} and η for the plasmonic and planar device sets in sample types: A, B and C. A similar approach is used to calculate the error bars for the textured device D.

As will be seen in the later Sections of this Chapter, the J-V characteristics of all the fabricated devices indicate a low leakage current. Hence, the J_{sc} can be viewed as a direct measurement of the effect of optical absorption enhancement on the electrical properties of the solar cell. In order to evaluate the effect of enhanced NIR light-trapping by the plasmonic nanodiscs, it is important to confirm if the enhanced J_{sc} in the plasmonic devices is due to increased optical absorption enhancement in the NIR, 700-1150 nm wavelength region. This evaluation will be performed in Sections 7.5.4 and 7.5.5 of this Chapter, where we will also analyse the factors which contribute to a decreased J_{sc} in the plasmonic device

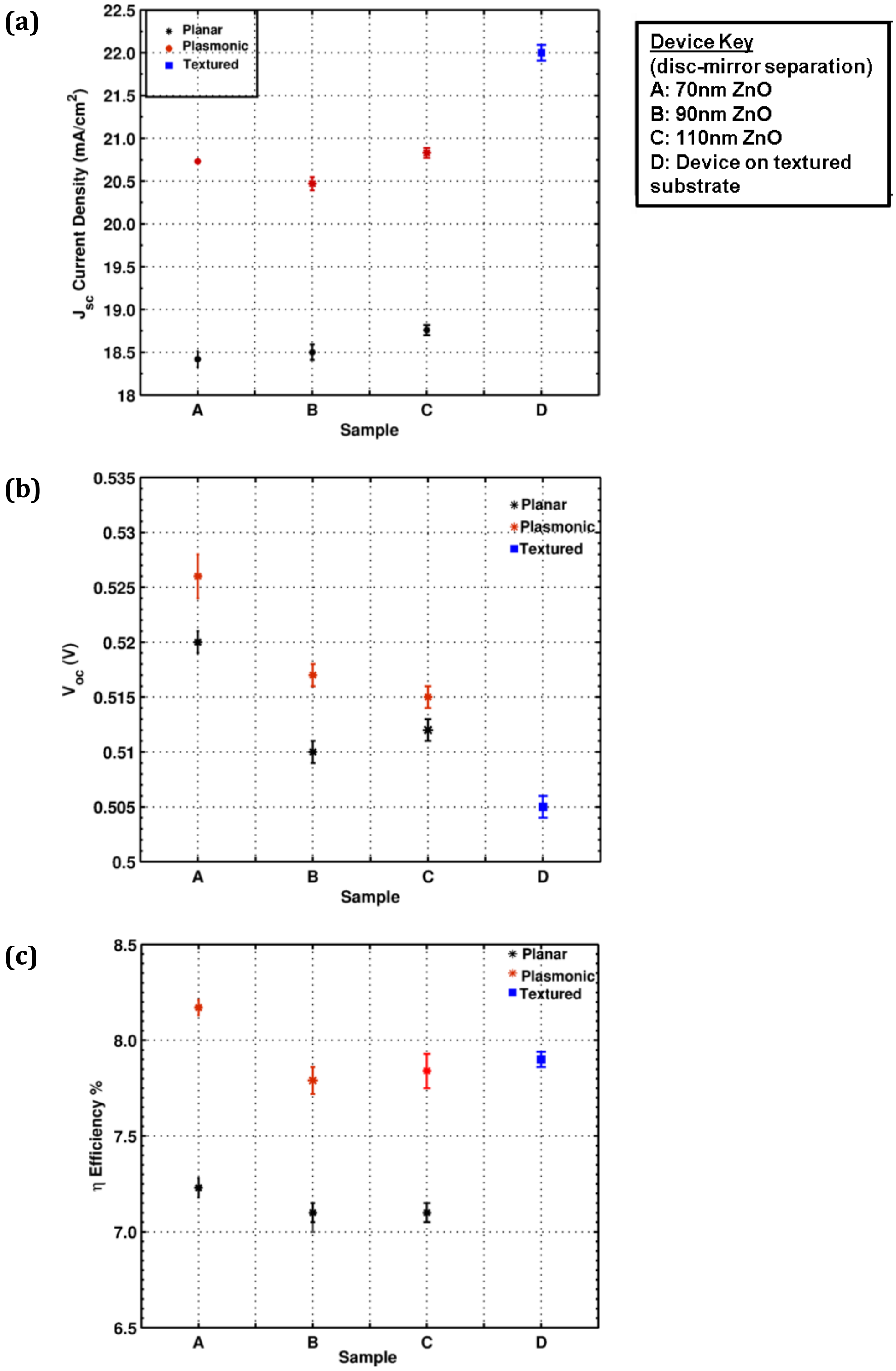

Figure 7.6 Summary of the measured **(a)** short circuit current density (J_{sc}), **(b)** open-circuit voltage (V_{oc}) and **(c)** the conversion efficiency η values for the planar and plasmonic devices: A, B, C and device on textured substrate: D. The devices are listed in Table 7.1. The error bars represent the standard deviation from the mean for J_{sc}, V_{oc} and η for the plasmonic and planar devices of sample types: A, B and C and textured device D.

when compared to the device on a textured substrate. Finally, in Section 7.5.6 of this Chapter, we will evaluate the reasons behind the minimal variations in the values of J_{sc}, V_{oc} and η despite changing the disc-mirror separation distances in plasmonic devices A, B and C.

7.5.3 Simulated Characteristics of a Planar Device

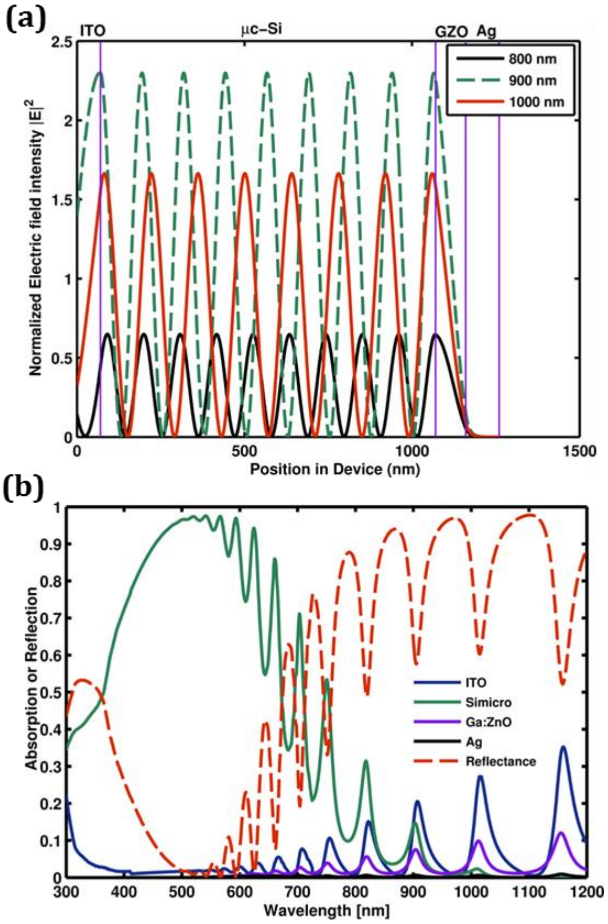

Figure 7.7: Transfer-matrix based simulation results for **(a) $|E|^2$** plotted at three wavelengths: 800nm, 900nm and 1000nm, as a function of position in a planar device consisting of (top-to-bottom) ITO/ μc-Si:H/ ZnO/Ag layers of thicknesses, 70nm, 1000nm, 90nm and 200nm, respectively. **(b)** Simulated reflection of light by the planar device across the 300-1200nm spectral range (dashed red line). The solid lines show the simulated absorption spectrum in each layer of the planar device, across the 300-1200nm wavelength range.

Before comparing the performance of a plasmonic device with its planar counterpart, we will simulate and briefly evaluate the optical properties of a planar device, i.e. a thin μc-Si:H solar cell with no nanodiscs, using a simple transfer-matrix optical model, available as an open source Matlab program developed by the McGehee Group at Stanford University [87]. The full details of the functions in the transfer matrix model can be found in a recent paper by McGehee *et al*. [87].

The thicknesses of the layers (top to bottom) in the simulated planar solar cell are: 70nm, 1000nm, 90nm and 200nm for the ITO, μc-Si:H, ZnO and Ag layers, respectively. These thicknesses correspond to the respective layer thicknesses in the fabricated planar device A. For reasons of simplicity, we have omitted the thin p-doped and n-doped μc-Si:H layers for the simulated device. This omission is not expected to drastically affect the results which are purely based on the simulation of the optical properties of the device. The optical constants for the ITO and Ga:ZnO layers have been provided by Dr. Fujiwara of AIST and the data for μc-Si:H layer have been provided by Dr. Sai of AIST. The optical constants for Ag have been obtained from tabulated data by Johnson and Christy [76]. The simulation model assumes perfectly planar layers – i.e. it does not account for inherent surface roughness which may exist in the layers for a fabricated device. However, these preliminary simulation results will be used to understand the optical absorption losses which already exist in a planar device before the incorporation of any plasmonic nanodiscs or texturing for enhanced light trapping.

In Figure 7.7a, we can observe the interference patterns of the electric field intensity $|\mathbf{E}|^2$ in the finite layers of the device. The $|\mathbf{E}|^2$ is plotted as a function of position in the device at three wavelengths in the NIR region: 800nm, 900nm and 1000nm. It can be observed that the magnitude of $|\mathbf{E}|^2$ at any point in the device shows a clear dependence on the wavelength of incident light. As we already discussed in earlier sections of this Chapter, the spectral properties of the $|\mathbf{E}|^2$ in the Ga:ZnO layer will influence the plasmonic resonance of the nanodiscs which will be embedded in this layer for the case of a plasmonic device.

In Figure 7.7b, the fraction of light reflected (R) from the simulated planar device is plotted as a dashed red-line. The fringes in the reflectance spectrum, which become predominant with increasing wavelength, can be attributed to the interference effects prevalent in the device, as demonstrated in Figure 7.7a. The absorption in the entire multilayer structure is then calculated as 1-R.

However, not all of the optical absorption occurs in the μc-Si:H layer. In Figure 7.7b, the solid lines indicate the absorption spectrum for each of the layers in the planar device.

In the 1μm μc-Si:H layer (solid line labelled 'Simicro'), the absorption rapidly decreases after approximately 600nm from 90% to negligible near-zero values in the NIR range at 1100nm. Hence light-trapping is required to enhance the optical absorption between 600-1100nm wavelength range for the 1μm μc-Si:H absorber layer. We also observe that there are parasitic absorption losses in the ITO and Ga:ZnO layers. In the ITO layer, there is absorption in the deep-ultraviolet range from 300nm to 400nm due to band-to-band absorption [20]. The ITO and Ga:ZnO layers also exhibit high parasitic absorption losses in the long-wavelength range, beyond 600nm, due to free-carrier absorption. The Ag mirror also exhibits negligible non-zero absorption losses in the NIR range.

Hence, the transfer-matrix simulation results demonstrate that in a planar device, not all of the optical absorption that occurs in the multilayer structure is useful absorption. The absorption in the 1μm μc-Si:H layer rapidly decreases to negligible near-to-zero values beyond a wavelength of 600nm. The ITO and Ga:ZnO layers exhibit high parasitic absorption losses which increase rapidly with incident wavelength, beyond 600nm. Based on these simulations, the model has also been used to calculate the J_{sc} based on the assumption that every absorbed photon generates a pair of charge carriers and that there is no recombination loss in the device. The predicted J_{sc} value of 19.0mA is only 0.6mA higher than the actual J_{sc} value of 18.4mA, measured for the fabricated planar device A. The good agreement between the predicted and measured J_{sc} values indicates that the simulated optical properties can be viewed as a good approximation of the absorption processes that occur in the different layers of the fabricated planar device A.

7.5.4 Comparison of the Plasmonic Solar Cell with a Planar Solar Cell

Figure 7.8a depicts the measured J-V characteristics for the planar and plasmonic devices in set A, where the disc-mirror separation is 70nm. It can be seen that the devices exhibit good J-V characteristics with low leakage currents, and reasonable fill-factors (FF); this helps to validate the comparison of the electrical performance of the two devices. The plasmonic device shows a clear increase of 2.3mA in the $J_{sc,}$ 6mV increase in V_{oc} and an increase of 0.97% in conversion efficiency when compared to the planar device. Hence, based on the key electrical measurement results, the plasmonic device performs better than the planar device.

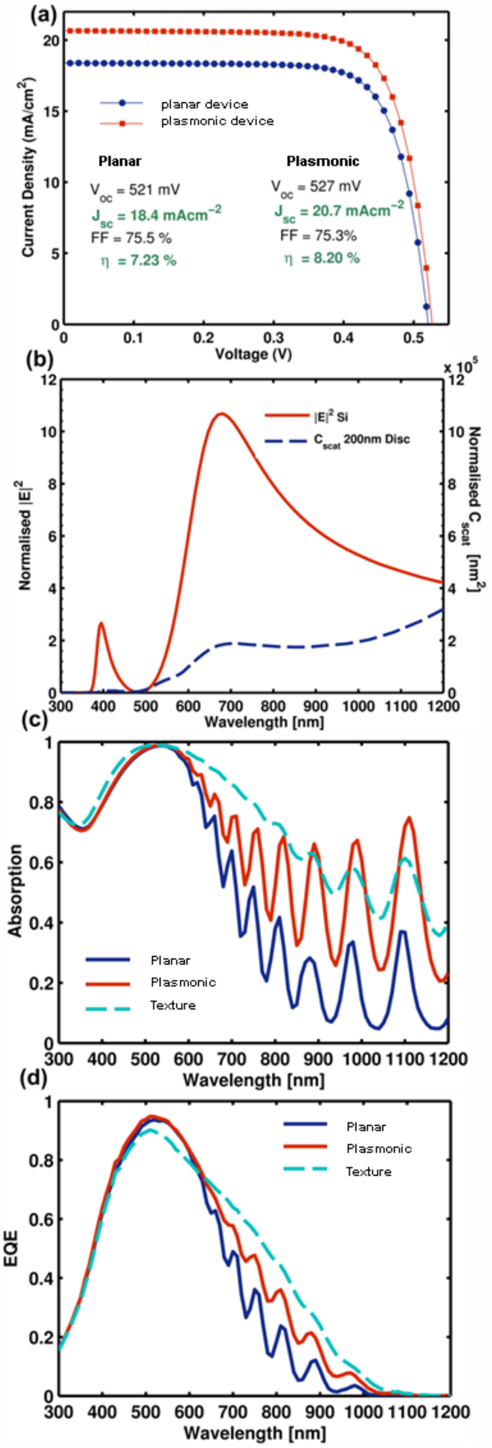

Figure 7.8 (a) Measured J-V characteristics for the planar and plasmonic devices in device set A, with a 70nm disc-mirror separation. **(b)** FDTD simulation results for normalised C_{scat} [nm^2] and $|\mathbf{E}|^2$ for semi-infinite Si/ 90nm ZnO/semi-infinite Ag mirror structure with a 200nm diameter nanodisc embedded in ZnO, with a 70nm disc-mirror separation distance. **(c)** Measured absorption spectra and **(d)** Measured external quantum efficiency (EQE) spectra for planar and plasmonic devices in device set A and for device D, fabricated on a conventional textured mirror substrate.

In order to evaluate whether the enhanced J_{sc} is truly an effect of plasmonically enhanced light-trapping, we refer to Figure 7.8b which illustrates the simulated C_{scat} of a 200nm Ag nanodisc at 70nm separation from the mirror and 20nm separation from a semi-infinite Si layer. As already seen in Section 7.2.2, the introduction of the Si layer results in an increased bandwidth of the peak C_{scat} and red-shift of the peak C_{scat} wavelength into the NIR region. In the current set-up, the peak C_{scat} of the 200nm diameter Ag nanodisc is shifted beyond 1200nm. However, the value of C_{scat} in the 700-1200nm wavelength range is still higher than the geometrical cross-section (3.14×10^4 nm^2) of the disc. Figure 7.8c indicates that the optical absorption in the plasmonic device is higher than the planar device in the 700-1200nm range. The wavelength range for absorption enhancement falls within the wavelength range of the plasmonic scattering predicted by the simulation results in Figure 7.8b. This observation indicates that the plasmonic scattering of NIR photons by the 200nm Ag nanodiscs is likely to have contributed to the observed increase in optical absorption enhancement in this region for the plasmonic device.

Further, the wavelength region for EQE enhancement is the same as the wavelength region for absorption enhancement in the plasmonic device (c.f. Figures 7.8c and 7.8d). Hence, the absorption enhancement in the NIR region has contributed to 'useful absorption' in the plasmonic device and resulted in an increase in the number of charge carriers generated by the NIR photons when compared to the planar device. In Section 7.5.5 of this Chapter, we will quantify the 'useful' optical absorption enhancement and parasitic losses in the NIR region and calculate the exact photogenerated current due to enhanced absorption by the plasmonic device in the NIR region.

For device D, fabricated on a conventional textured substrate, the rough texture and conformal growth of the device on the substrate result in subdued interference fringes in the absorption spectrum as seen in Figure 7.8c. The interference fringes are more pronounced in the absorption spectrum of the plasmonic device when compared to device D. Further, the spectral position of the interference fringes in the plasmonic device coincide very well with the spectral positions of the interference fringes in the planar device. These two observations can be viewed as a qualitative indication of the similarity in the 'flatness' of the plasmonic device to the planar substrate. As a result of this similarity we can also conclude that the enhanced optical absorption in the NIR region is more likely due to plasmonic light-scattering rather than an increase in the surface roughness of the device due to the presence of nanoscale features in the rear substrate.

7.5.5 Comparison of the Plasmonic Solar Cell with a Textured Solar Cell

In Section 7.5.1 of this Chapter, the plasmonic device was shown to have a significantly lower surface roughness when compared to device D on a textured substrate. It would hence be useful to compare the optical and electrical performance of the low-surface-roughness plasmonic device with a conventional textured solar cell.

First, we briefly analyse the characteristics of the absorption and EQE spectra for the plasmonic device and device D, when normalised to the absorption and EQE

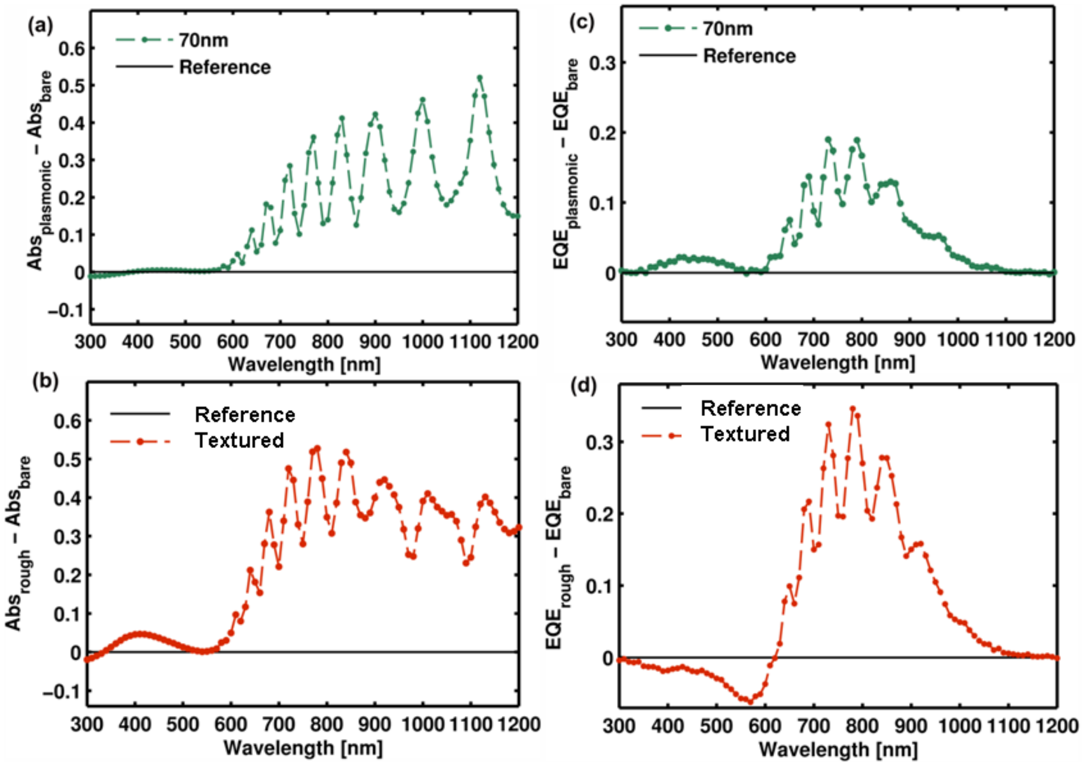

Figure 7.9 Normalised absorption for **(a)** plasmonic device A with 70nm disc-mirror separation and **(b)** device D, fabricated on a conventional textured mirror substrate. Normalisation is done by subtracting the is performed by subtracting the absorption spectrum for the planar device from the absorption spectra of plasmonic device and device D, across the 300-1200nm spectral range. Normalised EQE spectra for **(c)** plasmonic device A and **(d)** device D. The normalisation for the EQE spectra is performed in the same way as the normalisation for the absorption spectra.

characteristics of the planar device. Here, the normalisation is performed by subtracting the absorption and EQE values for the planar device from the absorption and EQE values for the plasmonic device and device D, across the 300-1200nm spectral range. The resulting normalised spectra are plotted in Figures 7.9a to 7.9d. The reference spectrum is plotted as a solid line in all the figures. Although the as-measured absorption and EQE spectra for the plasmonic device and Device D have already been shown in Figure 7.8c, it is useful to normalise the spectra in order to clearly highlight features and differences which are otherwise not as explicit when comparing the as-measured plots.

The plasmonic device exhibits a clear overall increase in optical absorption in the NIR region from 600-1200nm, when compared to the planar device (Figure 7.9a). However, the near-bandgap region of μc-Si:H solar cells is just below a wavelength of approximately 1120nm. Comparing the normalised absorption and EQE spectra for the plasmonic device (Figures 7.9a and 7.9c, respectively), the photons absorbed beyond 1050nm do not contribute to an increase in EQE of the plasmonic device. Comparing the normalised absorption and EQE spectra for device D (Figures 7.9b and 7.9d, respectively), we note that the photons absorbed between 620nm to 1050nm contribute to an increase in the EQE for Device D, which is higher than the absolute increase in EQE for the plasmonic device.

In Figure 7.9b, in the short wavelength region, between 350nm to 500nm, the normalised absorption spectrum of device D indicates an increase in optical absorption. However, the increased absorption in the short wavelength region does not appear to contribute to an increased EQE for device D (Figure 7.9d); in fact, the EQE of device D is less than that of the planar device in the 300nm to 620nm wavelength range. Hence, we conclude the device on textured substrate shows a significant parasitic absorption loss in the short-wavelength region. Unlike the device on the textured substrate, the plasmonic device does not exhibit a parasitic absorption loss in the short wavelength region.

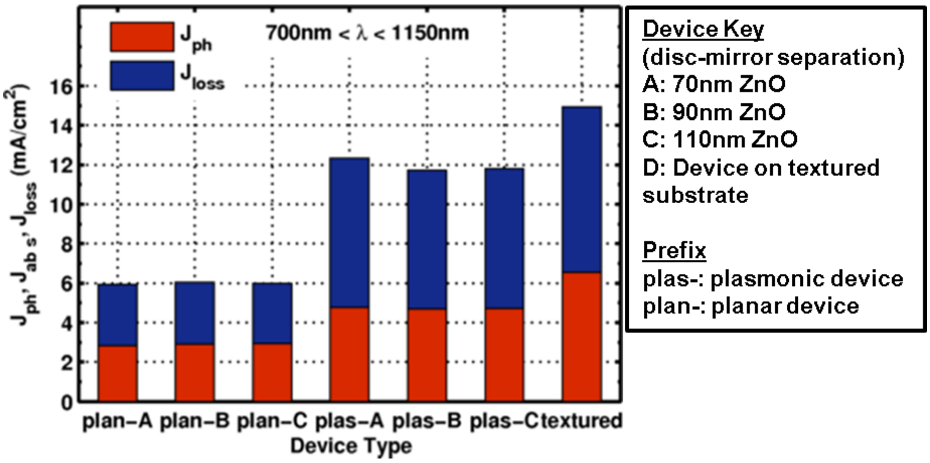

Figure 7.10 Calculated current density from measured absorption (J_{abs}), photocurrent density (J_{ph}) and quantified absorption loss (J_{loss}), in the NIR wavelength region, for plasmonic devices A, B and C and their planar counterparts and for device D. J_{abs} is defined as the sum of J_{ph} and J_{loss}.

As the plasmonic mirror has been developed for light-trapping in the NIR region, it is useful to compare the optical and electrical performance of the plasmonic devices A, B and C with Device D and their planar device counterparts, in the NIR region. We will quantify the optical absorption enhancement in the NIR region by calculating the photocurrent density, J_{ph}, generated by photons with wavelengths between 700nm to 1150nm. Additionally, we will compare the absorption loss that occurs in the devices, in the NIR region. We will implement the same method to calculate the absorption loss and photocurrent density in the NIR region, as stated by Sai *et al.* in a recent paper comparing the performance of different types of front and rear textures in thin solar cells [20].

The expected current density as predicted by the absorption spectrum for a given device can be calculated as:

$$J_{abs} = q \times \int_{\lambda_1}^{\lambda_2} Abs(\lambda) I_{solar}(\lambda) d\lambda \qquad \textbf{(1)}$$

The photocurrent density in the NIR region can be calculated using the EQE spectrum as:

$$J_{ph} = q \times \int_{\lambda_1}^{\lambda_2} EQE(\lambda) I_{solar}(\lambda) d\lambda \qquad \textbf{(2)}$$

And hence the absorption loss in the NIR region can be quantified as :

$$J_{loss} = J_{abs} - J_{ph} \qquad \textbf{(3)}$$

Where, ‘q’ is the elementary charge, ‘I_{solar}’ is the spectral photon density for a standard AM1.5 solar spectrum, and Abs(λ) and EQE(λ)are the measured absorption and EQE spectra, respectively. The integration is performed in the NIR wavelength region from 700nm to 1150nm.

Figure 7.10 shows the J_{abs}, J_{ph} and J_{loss} for plasmonic devices A, B and C and their planar counterparts and for device D. It can be observed that the plasmonic devices show a clear 2.0mA increase in J_{ph} when compared to their planar counterparts. In fact, if the calculated increase of 2.0mA in the J_{ph} in NIR region is compared with the increase in J_{sc} between the plasmonic devices and their planar counterparts, which is only slightly higher than 2.0mA, (Figure 7.8a, Section 7.5.4), we observe that the increase in J_{sc} in the plasmonic devices is entirely due to increase in the photocurrent density, J_{ph} , in the NIR region. Hence the optical absorption enhancement by NIR plasmonic light-trapping has indeed been effective by contributing to useful NIR absorption and increase in the J_{ph} in the NIR region.

Device D on the other hand shows a 3.6mA increase in NIR J_{ph} when compared to the planar devices. However, it must be re-emphasised that the plasmonic devices have surface roughness values which are significantly lower than (almost half the value of) the surface roughness of Device D. Hence, despite exhibiting a low surface roughness, and a low surface coverage of plasmonic nanodiscs, the difference in the J_{ph} generated by the plasmonic devices when compared to Device D, is around 1.6mA. While it is currently difficult to state whether the value of 1.6mA is a substantial difference, further studies can be conducted to evaluate whether higher nanodisc surface coverages and a non-adhesion layer free EBL process can result in plasmonic devices with J_{ph} in the NIR region being comparable to or even higher than that of a device on a conventional textured substrate.

The plasmonic devices and Device D exhibit a higher J_{loss} when compared to the planar devices. The J_{ph} /J_{abs} ratio for the plasmonic devices and Device D is less than 0.43, indicating that more than half of the absorbed photons are lost in the NIR region. However, the processes accounting for absorption loss in the plasmonic device may differ from that in Device D, as the former includes parasitic absorption loss in the nanodiscs, as a result of plasmonic resonance. It is interesting to note however, that in the fabricated plasmonic devices, the incurred absorption loss which also includes plasmonic absorption losses, does not exceed the absorption loss that is usually encountered in conventional textured devices.

We note that despite changing the disc-mirror separation between plasmonic devices A, B and C, the J_{ph}, J_{loss} and J_{abs} characteristics in the NIR region are very similar for all three devices. In the following Section, we will analyse the reason for this apparent similarity in the optical and electrical performances for plasmonic devices with varying disc-mirror separation distances.

7.5.6 Effect of changing disc-mirror separation

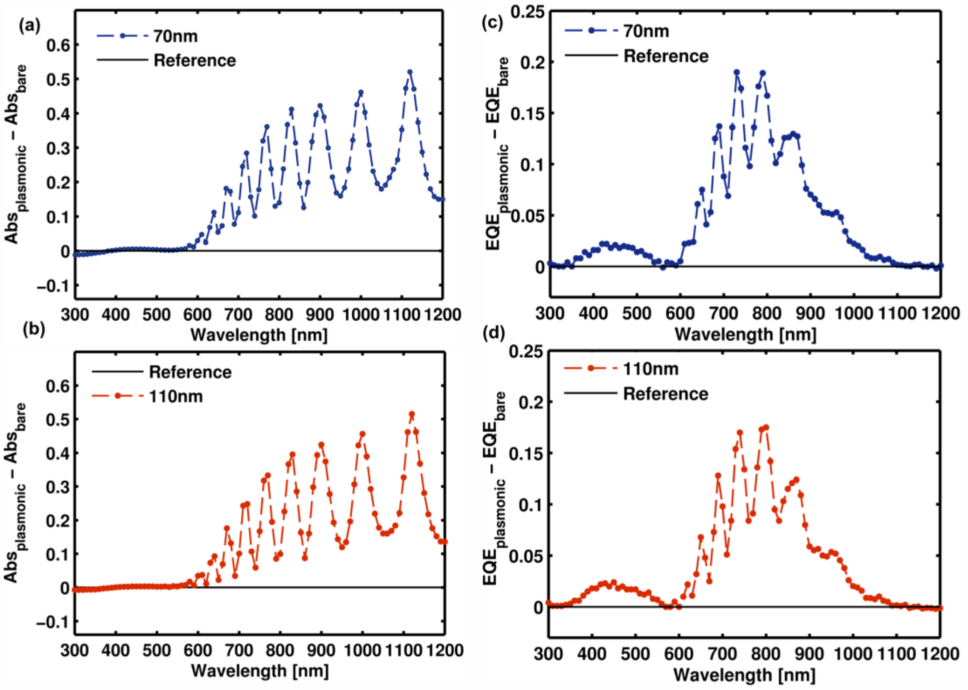

Figure 7.11 Normalised absorption for **(a)** plasmonic device A with 70nm disc-mirror separation and **(b)** plasmonic device C, with 110nm disc-mirror separation. Normalisation is done by subtracting the is performed by subtracting the absorption spectrum for the planar device from the absorption spectra of plasmonic device A and plasmonic device C, across the 300-1200nm spectral range. Normalised EQE spectra for **(c)** plasmonic device A and **(d)** plasmonic device C. The normalisation for the EQE spectra is performed in the same way as the normalisation for the absorption spectra.

The plasmonic devices: A, B and C have different disc-mirror separations of 70nm, 90nm and 110nm, respectively. However, as observed earlier in Figure 7.6 the values for the electrical parameters: J_{sc}, V_{oc} and η for all three devices are similar. Figure 7.11 shows the normalised absorption and normalised EQE spectra for plasmonic device A (Figure 7.11a and 7.11c) and plasmonic device C (Figure 7.11b and Figure 7.11d). Although the disc-mirror separation increases by 40nm in device C when compared to device A, there is no significant change in the optical absorption characteristics and the resultant EQE characteristics between the two devices. We have not included the corresponding normalised spectra for device B in the above comparison as the reference planar device in this case, had to be re-fabricated due to a shunted reference cell in the first fabrication attempt. As the re-fabricated reference cell was not co-deposited with the plasmonic device B, there might be slight variations in the normalised absorption and EQE spectra for device B, when compared to the corresponding normalised spectra for devices A and C. However, the raw-data for the optical absorption, measured J-V and EQE characteristics for plasmonic devices B and C is included in Appendix 3, where the similarity in the optical and electrical characteristics between the devices can, once again, be clearly observed.

We attempt a preliminary explanation for the similarity in the optical behaviour between the plasmonic devices, by simulating the C_{scat} spectra for a 200nm Ag nanodisc, at 20nm from an overlying semi-infinite Si layer and at varying disc-mirror separations of 70nm, 90nm and 110nm. As already demonstrated in Section 7.2.2, for a given disc-mirror separation, the C_{scat} spectrum is dependent on the spectral properties of the intrinsic C_{scat} and the $|\mathbf{E}|^2$ calculated in the ZnO layer of the multilayer structure, without the nanodisc. The value of C_{scat} at a given separation distance, will be maximised if there is good spectral alignment between the peak intrinsic C_{scat} position and the spectral peak of the corresponding $|\mathbf{E}|^2$ at that separation distance.

First we consider the C_{scat} of the nanodisc in the multilayer, without the presence of the Ag mirror. That is, we consider the intrinsic C_{scat} for the 200nm nanodisc embedded in a semi-infinite ZnO layer, at 20nm distance from an overlying semi-infinite Si layer. The resulting intrinsic C_{scat} spectrum (Figure 7.12a, dotted line), peaks in the deep infrared range at a wavelength of around 1250nm.

Next, we simulate the driving field intensity, $|\mathbf{E}|^2$, in the ZnO layer of the Si/ZnO/Ag multilayer structure, without the nanodisc. The thickness of the ZnO from the mirror is varied as: 70nm, 90nm and 110nm (accounting for a constant 20nm ZnO 'capping layer' the total ZnO thickness between the Si and Ag mirror is varied as: 90nm, 110nm and 130nm, respectively). We observe that the peak $|\mathbf{E}|^2$ undergoes a spectral red-shift and simultaneous decrease in magnitude with increasing thickness of the ZnO from the mirror

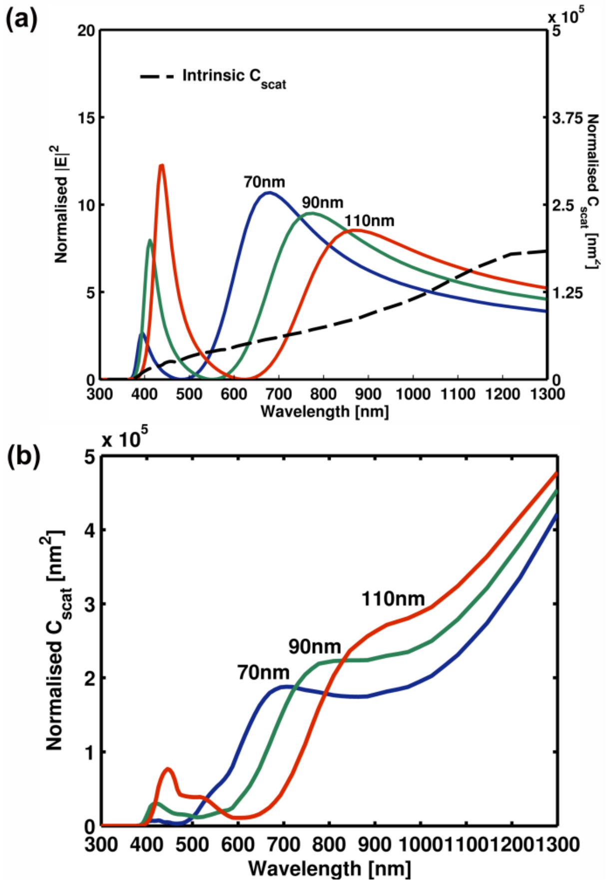

Figure 7.12 FDTD simulation results of **(a)** normalised intrinsic C_{scat} [nm^2] for a 200nm diameter Ag nanodisc of height 40nm, embedded in a semi-infinite ZnO layer, at 20nm distance from an overlying semi-infinite Si layer (dotted line); normalised |**E**|^2 (solid lines), in the ZnO layer of the Si/ZnO/Ag multilayer structure, without the nanodisc. The thickness of the ZnO from the mirror is varied as: 70nm, 90nm and 110nm. **(b)** Normalised C_{scat} [nm^2] at 70nm, 90nm and 110nm disc-mirror separations for the Si/ZnO/Ag multilayer structure with the Ag nanodisc.

(Figure 7.12a). As a result, the value of |**E**|^2, at any given wavelength up to approximately 700nm, decreases with separation distance. Beyond 800nm, the value of |**E**|^2 at any given wavelength shows a moderate increase with separation distance.

Finally, we simulate the C_{scat} at different disc-mirror separations for the Si/ZnO/Ag multilayer structure with the Ag nanodisc (Figure 7.12b). The resultant trend in the C_{scat} value closely follows the trend in |**E**|^2 with separation distance. At any given wavelength, up to 700nm, the value of the C_{scat} decreases with the disc-mirror separation distance. Beyond 800nm, the value of C_{scat} increases with disc-mirror separation.

As can be observed in Figure 7.12b, the peak C_{scat} will occur beyond 1200nm. However, at a given separation distance, a local maximum occurs in the C_{scat} spectrum, the position of which, coincides with spectral position of the peak $|\mathbf{E}|^2$ at that distance. The local maximum in the C_{scat} falls within the required 700-1150nm wavelength range, for all three separation distances. However, the increase in the local maximum C_{scat} value with separation distance is moderate, from a factor of 7 to a factor of 10 times the geometrical cross section (3.14×10^4 nm^2) of the 200nm nanodisc. The increase in C_{scat} is moderate, mainly because the value of the intrinsic C_{scat} at the spectral positions of the peak $|\mathbf{E}|^2$ for 70, 90 and 110nm separation distances, is much lower than the peak intrinsic C_{scat} value.

Based on the above simulations results, we can conclude that one of the main reasons for the similarities observed in the measured optical and electrical performance of the plasmonic devices with separation distances of 70nm, 90nm and 110nm, is that the increase in C_{scat} with disc-mirror separation is moderate and hence, not significant enough to cause a discernible difference in the optical behaviour of the plasmonic devices.

7.6 Conclusion

In the first part of this Chapter we demonstrated using FDTD simulations that the spectral dependence of C_{scat} on $|\mathbf{E}|^2$ is preserved even with the introduction of a nearby Si layer. The introduction of the Si layer results in a significant red-shift of the peak C_{scat} wavelength into the NIR region, when compared to the spectral properties of the peak C_{scat} for the plasmonic mirror in air. The optimised thickness of the spacer layer, for maximum peak C_{scat} magnitude, is larger for the mirror near Si when compared to the mirror in air. We fabricated a thin n-i-p μC-Si:H solar cell with the plasmonic mirror integrated at the rear of the device. The optimised plasmonic solar cell showed an increase of 2.3mA in the J_{sc}, 6mV in V_{oc} and 0.97% in η, when compared to the planar cell counterpart with no nanodiscs. The increase in J_{sc} was demonstrated to be mainly due to optical absorption enhancement in the NIR region as a result of plasmonic scattering, by detailed calculation of the exact photogenerated current in the plasmonic and planar devices, for the 700-1150nm wavelength range. The plasmonic solar cell with 70nm separation distance showed a η of 8.20% which was slightly higher than that of the device fabricated on a conventional textured mirror substrate. However, the J_{sc} of the plasmonic solar cell was lower by 1mA when compared to the device on textured substrate. There is a potential to further increase the J_{sc} of the plasmonic device by increasing nanodisc surface coverage and using an adhesion-free EBL process for fabrication of the nanodiscs. Varying the nanodisc-mirror separation distance from 70nm to 110nm, still resulted in plasmonic solar cells with higher V_{oc}, J_{sc} and η than their planar cell counterparts. However, varying the disc-mirror separation distance did not result in any significant change in the optical and electrical behaviour of the plasmonic devices. One possible reason for this similarity was demonstrated using FDTD simulations - the increase in the maximum C_{scat} with disc-mirror separation, for the Si/ZnO/Ag mirror structure with the 200nm Ag nanodisc at the rear, is moderate, from a factor of 7 to a factor of 10 times the geometrical cross section of the nanodisc. This moderate increase in C_{scat} with separation distance is not significant enough to cause a discernible difference in the optical behaviour of the plasmonic devices.

[This page intentionally left blank]

Chapter 8

Discussions, Conclusions and Future Work

8.1 Discussions

The development of μc-Si:H solar cells is a relatively new research area given that the first devices were only fabricated in the early 1990s [9]. Research into the development of μc-Si:H devices has recently gained momentum because of several important advancements in thin film photovoltaics. Firstly, μc-Si:H as a material does not show light-induced degradation in material quality like a-Si:H. Secondly, due to its bandgap value being close to that of c-Si (refer Chapter 1), NIR photons can be absorbed more efficiently in μc-Si:H solar cells when compared to a-Si:H solar cells. Further, the growing interest in multijunction solar cells has also spurred research into the optimisation of μc-Si:H. In a multijunction a-Si:H/μc-Si:H solar cell, the a-Si:H layer is optimised to absorb short-wavelength photons up to around 700nm and μc-Si:H layer is used to absorb the photons in NIR region, thus providing a wider coverage of the AM1.5 spectrum. Hence, given the growing interest in μc-Si:H solar cells, it follows that developing methods to increase the optical and electrical efficiency of these devices is of crucial importance. In this Section, we will critically evaluate the contribution of this work, on developing a plasmonic light-scattering system for μc-Si:H solar cells, to the recent research advancements in the same area.

8.1.1 Contribution of this Thesis to Recent Advancements in Plasmonic μc-Si:H Solar Cells

8.1.1.1 Enhancement in J_{sc}

In Chapter 3 of this work we reviewed recent advancements in enhancing the optical absorption in μc-Si:H solar cells using light-scattering by plasmonic nanostructures integrated into the rear of the device. Figure 8.1 compares the J_{sc} enhancement results for

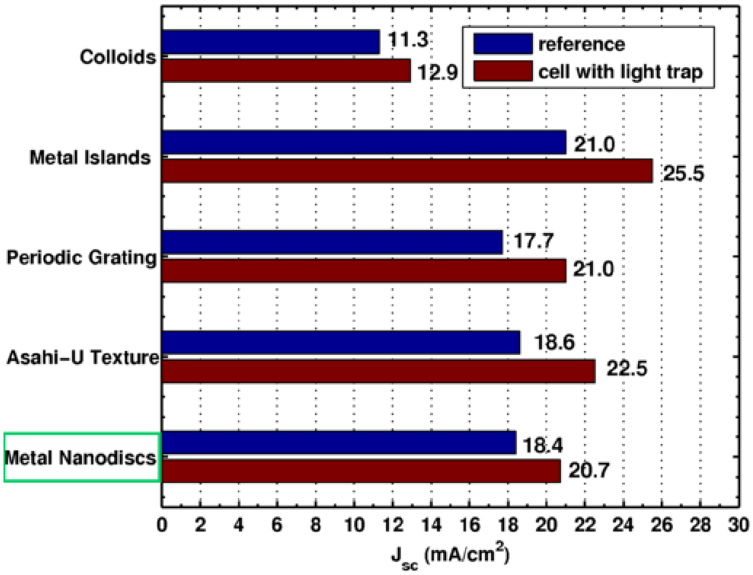

Figure 8.1. Summary of the results which represent the 'best' (highest) J_{sc} values for the plasmonic device with corresponding J_{sc} value for reference device, for different plasmonic back mirror configurations: colloids [70], Ag islands [24], periodic grating [19], and Asahi-U texture [18]. The corresponding results for the plasmonic mirror with Ag nanodiscs (label highlighted in green) fabricated in this work is also included.

the n-i-p μc-Si:H device with Ag nanodiscs developed in this work, with the different plasmonic devices developed by other research groups. These devices were already reviewed in detail in Chapter 3. It can be observed that the increase in the J_{sc} (2.3mA) of our device with the nanodiscs is significantly better than the increase offered by using colloids near the rear mirror – a structure developed by Mizuno *et al*. [70]. In fact, the enhancement in J_{sc} by using the Ag nanodiscs only differs marginally (by 1mA) from the corresponding enhancement offered using the periodic grating structures developed by Paetzold *et al*. [19]. The metal islands-near-mirror configuration developed by Tan *et al*., offers the highest increase in J_{sc} : almost double the increase offered by the plasmonic nanodiscs. However, as will be seen in the next Section, it is also important to improve the electrical efficiency of the solar cell which is determined by the V_{oc}, FF and J_{sc} values.

8.1.1.2 Electrical Quality of the Solar Cell

The mirror with a high surface coverage of 20% of large irregular metal island (with a 600nm average diameter), developed by Tan *et al*. may be expected to exhibit a high root-

	Reference Device	**Plasmonic Device**
Metal Islands (Tan *et al.* [24])	**η** = 6.30% $\mathbf{V_{oc}}$ = 479mV **FF** = 66.3%	**η** = 7.30% $\mathbf{V_{oc}}$ = 498mV **FF** = 57.5%
Ag Nanodiscs (this work)	**η** = 7.23% $\mathbf{V_{oc}}$ = 521mV **FF** = 75.5%	**η** = 8.20% $\mathbf{V_{oc}}$ = 527mV **FF** = 75.3%

Table 8.1: Efficiency, (η), V_{oc} and J_{sc} values for the μc-Si:H solar cell with metal islands developed by Tan *et al.* [24] and Ag nanodiscs, developed in this work.

mean-square surface roughness (σ_{rms}). Although the authors do not state the value of the surface roughness, it can be seen in Table 8.1 that the FF of the device with the metal islands has significantly decreased by 8.8%. As reviewed in Chapter 3, one of the main reasons for a decrease in FF, especially in μc-Si:H solar cells is an increase in the shunt resistance (R_{sh}) of the device [9]. R_{sh} is increased due to a degradation in the material quality of the intrinsic μc-Si:H layer due to its conformal growth on a significantly rough substrate or a substrate where the features of the texture have high-aspect ratios. [23, 24] Comparatively, our plasmonic device shows a constant FF value – this can be attributed to the low σ_{rms} of around 13.5nm for of the plasmonic nanodiscs (refer Chapter 6). Hence, despite the a significant enhancement of the J_{sc} with metal island, due to a significant decrease in the FF value, the plasmonic device with metal islands exhibits an efficiency increase that is similar to our device with Ag nanodiscs.

We also note here that the textured devices (on Asahi-U substrates) fabricated in this work also showed a 5% decrease in the FF when compared to a device on a planar metal substrate. This observation re-iterates the fact that although a textured substrate may exhibit efficient light-scattering properties, if it has a high σ_{rms}, it will decrease the FF value of the device, thereby negating the effect of the enhanced J_{sc} value on the overall efficiency of the device.

In this Section, we have critically analysed the optical and electrical properties of the plasmonic device developed in this work to the optimised plasmonic devices developed by other research groups. The main advantage of the plasmonic mirror with nanodiscs is the increase the optical absorption of the solar cell, *without* a degradation in the electrical quality of the intrinsic μc-Si:H layer as a result of integrating the mirror. Also, the surface coverage of the nanodiscs is only 6% indicating that there may be a potential for further enhancement in J_{sc} if a higher surface coverage of nanodiscs is used - although this is a topic for further research. In the following section we will summarise the main results of this work.

8.2 Conclusions

The interaction of light, of a given wavelength, with a metal nanostructure results in the resonant excitation of the electron cloud on the surface of the nanostructure. It is possible to tune this excitation also known as the plasmonic resonance, to enable a strong scattering of light by the nanostructure. The radiative efficiency, the wavelength and the bandwidth of the plasmonic dipolar resonance increase with particle size. An increase in the refractive index of the surrounding medium causes a red-shift in the plasmonic resonance with no significant decrease in peak magnitude. The broadband radiative efficiency comparisons for large nanospheres composed of different types of metals: Ag, Al, Au and Cu, demonstrated that the Ag nanosphere has the highest broadband radiative efficiency in the visible to NIR wavelength range, followed by the Au nanosphere. This is mainly because the lossy interband transitions occur outside this target wavelength range for both the metals.

Plasmonic metal nanoparticles designed to strongly scatter light can be integrated into thin solar cells for light-trapping applications. For applications in thin Si solar cells, the metal nanoparticle must strongly scatter light in the near-bandgap, near-infrared wavelength region. A critical review of the recent progress in plasmonic-light trapping applications for μc-Si:H solar cells showed that nanoparticles placed at the rear of solar cells can overcome losses due to back-scattering. The forward-scattered light can be reflected by the planar metal back contact in the solar cell to reinforce the plasmonic light-scattering mechanism. The reviewed studies demonstrated an enhancement in the J_{sc} value and hence the optical absorption efficiency of the μc-Si:H solar cell as a result of the integration of nanoparticles near the rear metal contact. However, it was observed that substrates with a high surface roughness or with features which have high-aspect ratios degrade the electrical quality of the μc-Si:H layer deposited onto them thereby negatively affecting the FF, V_{oc} and efficiency values of the device. An important design rule for integration of the plasmonic layer is to ensure that the enhanced optical efficiency offered by the plasmonic layer is not outweighed by the negative effects on electrical efficiency due to surface morphology of the nanostructures.

An experimental investigation on the effect of varying the nanoparticle-mirror separation, for Ag islands near a Ag mirror, showed a red-shift and an increase in bandwidth of the diffuse reflectance peak with the separation distance. For a given metal island size, there is a separation distance for which the magnitude of the peak diffuse reflectance is optimised. The mirror with metal islands shows a stronger NIR light-scattering but significantly higher broadband absorption losses when compared to a conventional textured mirror. We concluded that the irregular distribution in the shape and size of the metal islands coupled with a high surface coverage (hence, smaller interparticle distance) is one of the possible reasons for large broadband absorption losses.

Numerical simulation results based on the FDTD method, demonstrated that one main reason the spectral tunability in diffuse reflectance with nanoparticle-mirror separation distance is the tunability of the electric field driving the plasmonic resonance, with the separation distance. The driving field strongly influences the spectral properties of the scattering cross-section for the nanoparticle near the mirror. The plasmonic scattering can be maximised for a given spectral range if the peak of the driving field at a given separation distance, is tuned to coincide with the intrinsic resonance (resonance without the mirror) of the nanoparticle

An EBL process was successfully developed to fabricate a plasmonic mirror with pseudo-random arrays of Ag nanodiscs. The EBL process offers a high degree of control over the size, shape and interparticle distance of the metal nanostructures. The optical scattering properties of the mirror with Ag nanodiscs are tunable with thickness of the spacer layer. Scattering is maximised by tuning the size of the nanodisc such that the plasmonic resonance peak coincides with the peak of the driving field intensity in the required spectral range. The optimized plasmonic mirror showed higher diffusive reflectivity than a conventional textured mirror in the NIR region, over a broad angular range. More importantly, the plasmonic mirror demonstrated low broadband absorption losses, almost comparable to that of the conventional textured mirror, thereby outperforming the plasmonic mirror with Ag islands. The optimised mirror also shows a low surface roughness with a σ_{rms} value of 13.5nm.

Simulation results show that the introduction of the Si layer onto the nanoparticle-near-mirror structure results in a significant red-shift of the peak scattering cross section when compared to the scattering properties for the plasmonic mirror in air. The optimised thickness of the spacer layer for maximum scattering cross-section, is larger for the mirror near Si when compared to the mirror in air.

We successfully fabricated an efficient thin n-i-p μc-Si:H solar cell with the plasmonic mirror integrated at the rear of the device. The optimised plasmonic solar cell showed an increase of 2.3mA in the J_{sc}, 6mV in V_{oc} and 0.97% in η, when compared to the planar cell counterpart with no nanodiscs. The low surface roughness of the plasmonic mirror ensures no degradation in the electrical quality of the μc-Si:H layer – this is also confirmed by the constant value of the FF. The increase in J_{sc} was demonstrated to be mainly due to optical absorption enhancement in the NIR region as a result of plasmonic scattering, by detailed calculation of the exact photogenerated current in the plasmonic and planar devices, for the 700-1150nm wavelength range. The plasmonic solar cell with 70nm separation distance showed a η of 8.20% which was slightly higher than that of the device fabricated on a conventional textured mirror substrate. However, the J_{sc} of the plasmonic solar cell was lower by 1mA when compared to the device on textured substrate. An evaluation of the optical losses in the device with plasmonic mirror showed that the losses are comparable to that of a device fabricated on a conventional textured substrate. Transfer-matrix simulations of the planar device structure confirmed that not all of the absorption losses occur due to the plasmonic nanoparticles. The front ITO and rear Ga:ZnO layers exhibit high parasitic absorption losses, due to free-carrier absorption, which increase rapidly with incident wavelength, beyond 600nm.

Varying the nanodisc-mirror separation distance did not result in any significant change in the optical and electrical behaviour of the plasmonic solar cells. This is probably because the moderate increase in the (strongly red-shifted) scattering cross-section spectrum with separation distance is not significant enough to cause a discernible difference in the optical behaviour of the plasmonic devices.

8.3 Suggestions for Future Work

In this work, the plasmonic mirror with Ag nanodiscs was fabricated using EBL lithography. Noble metal nanoparticles do not adhere well to oxide layers and hence may be removed during the lift-off stage in the EBL process [88]. Ti and Cr are commonly used as adhesion layers to ensure good adherence between noble metal nanoparticles and oxide surfaces [88]. In our fabrication process we used a thin Ti adhesion layer to deposit the Ag nanodiscs onto an underlying TCO layer. Although using Cr as an adhesion layer has been shown in the literature to significantly attenuate the plasmonic resonance of Au on a silica substrate [88], a comparative study on the choice of the adhesion layer material, with an aim to minimise the attenuation in resonance, would be beneficial to further optimise the EBL fabrication process. The optimised mirror fabricated in this work shows low broadband absorption losses comparable to that of a conventional textured mirror. However, there is a potential for a further decrease in parasitic absorption losses if an adhesion-free EBL process is developed. As EBL is a time-consuming fabrication method, it is not possible to use this technique for commercial purposes. Nanoimprint lithography can be used for the large-scale fabrication of the plasmonic nanostructures, with a high degree of control on the distribution of size, shape and interparticle distance.

The influence of the surface coverage of metal nanostructures on the optical scattering properties of the plasmonic mirror is an important area for future research. If such a study can aim to predict the expected efficiency for a solar cell for a given surface coverage of the plasmonic nanostructures, then the results will be useful benchmarks for the large-scale fabrication of plasmonic mirrors using nanoimprint lithography. Such precise benchmarks are difficult to define for mirrors using metal islands due to the lack of control on the size and shape of the islands.

Another interesting area of research is the dependence of optical absorption enhancements for a device on the angle of the incident light, as the optical properties of the plasmonic mirror may vary with the angle of incidence [89].

The experimental results in Chapter 5 showed that the optical behaviour for metal islands at a separation of 10nm is independent of the island size. A very interesting scientific study would be to investigate the effect of placing plasmonic particles very close to the planar mirror. In this case, the surface coverage or interparticle distance can also be varied to study the influence of the mirror and possible LSP-PSP coupling on interparticle interactions [67].

Appendices

Appendix 1: Basic operation of a Solar Cell

A1.1 The PN junction

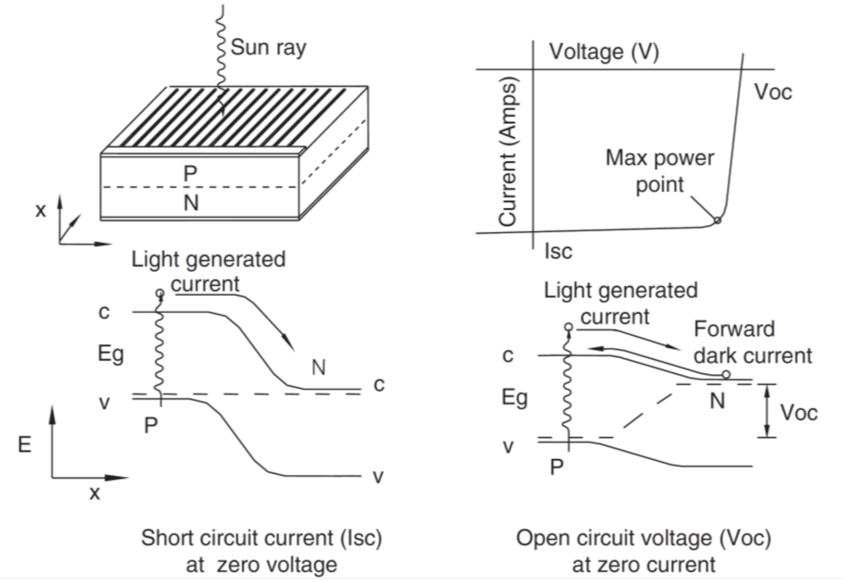

Figure 1. Basic operation of a p-n junction in a solar cell. Taken from [90]

Explanation of the Basic Operation of a p-n junction

As seen in Figure 1, a conventional solar cell consists of two electronically dissimilar materials brought together to form a junction. Typically, a p-type layer is formed by doping an intrinsic semiconductor such that there is an excess of holes e.g. silicon (Si) doped with boron (B) atoms and an n-type layer is formed by doping an intrinsic semiconductor with an excess of electrons e.g. Si doped with phosphorous (P) atoms. When the p and n layers are brought together, there is a diffusion of charge carriers from a region of high concentration to a region of low concentration; i.e. electrons diffuse to the p-type layer and holes diffuse to the n-type layer (Figure 1). This diffusion process results in the eventual formation of a p-n junction where electrons and holes have recombined such that this region is depleted of free charge with a built-in voltage. The band gap energy (E_g) of the semiconductor used for the solar cell determines the photon energies that can excite an electron from valence to conduction band and generate electron-hole pairs in the p-n junction of the solar cell. Electrons at the edge of the p-n junction are swept into the n-layer as a result of the electric field across the depletion region. If an external conductive pathway is connected between the n-type and p-type layers, the electrons in the n-type layer travel via the external path to the p-type, resulting in an external electrical current. Photons with energy less than E_g, fail to excite electrons and hence are not absorbed.

A1.2 Band Diagram of the p-i-n junction

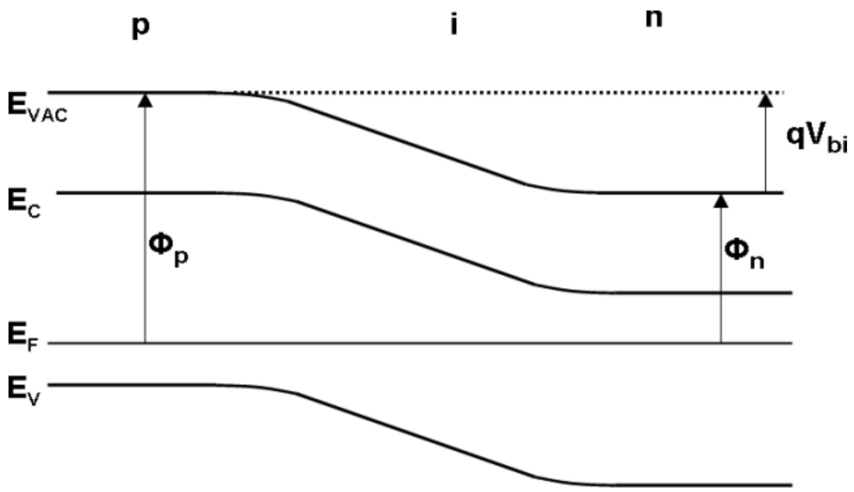

Figure 2: Band diagram of a p-i-n junction in equilibrium. E_F is the Fermi level, E_V is the energy level of the valence band, E_c is the energy level of the conduction band and E_{vac} is the vacuum energy level. V_{bi} is the built-in voltage which gives rise to the electric field in equilibrium. ϕ_p and ϕ_n are the work functions of the p-type layer and n-type layer respectively. Taken from [91].

Figure 2 shows the band diagram of a p-i-n junction in equilibrium. The main difference between the p-n junction in Figure 1 and the p-i-n junction in Figure 2 is the introduction of the intrinsic i-layer in the latter configuration. The i-layer has a typical thickness of 1-3μm and the built-in electric field is experienced over the length of the i-layer. The creation of electron-hole pairs due to energy transfer by incident photon occurs in the i-layer and the movement of the charge carriers is assisted by the electric field by drift rather than diffusion. A more detailed discussion of the p-i-n junction in μc-Si:H solar cells is discussed in Chapter 1 of this work.

Appendix 2: Stages of the Bi-Layer EBL Process

A2.1 EBL Recipe

The main reason for using a bi-layer process over a single-layer process is the undercut obtained in the resultant resist profile. The lack of a clear undercut in a single layer process may result in incomplete lift-off of the metal layer. In a bilayer process, an undercut ensures that there is no continuous path from the evaporated metal on the patterned resist to the substrate, i.e. there is no side-wall metal coverage to inhibit the lift-off of the resist. We have implemented a bi-layer PMMA/MMA EBL process primarily developed by Yudong Wang of the Nano Research Group, in the University of Southampton The first stages of the development outlined in this Section involve the fabrication of nanoparticles on a standard Si wafer. The main stages of the implemented bi-layer EBL process are:

1. CAD (L-edit) design of the resist pattern.
2. Spin coating of the copolymer MMA 8.5 (300nm) and then PMMA 495 (150nm) onto a Si wafer. As MMA is relatively more sensitive to electron beam exposure, it is spin coated first to facilitate undercut formation. The spin-speed is varied during the duration of the spin as follows: 0-500rpm for 5s, 500-5000rpm for 2s, 5000rpm 45s, 5000-100rpm 1s and 100rpm -0 for 1s. The same spin speed ramp up and ramp down times are used for PMMA and MMA as MMA is relatively more adhesive compared to PMMA. Note that there is an intermediate soft-bake of the substrate after MMA coating for 70s at 150^{o}C. There is a second soft-bake of the substrate with the bi-layer for 70s at 180^{o}C. As MMA and PMMA have similar optical refractive indices, the total thickness of the bilayer was checked using an ellipsometer to be ~400nm in thickness.
3. The resultant bi-layer resist is patterned with the design specified in the CAD layout. The accelerating voltage of the electron beam is 100kV (provides better resolution than 50kV) at beam current of 1na and spot size of 4nm. The 0% dose level i.e. base dose level has a value of 900μC/cm^2 (micro-Coulombs per square centimetre). Note that in the discussions throughout this thesis, unless stated otherwise, the dose levels are given as a percentage relative to the 900μC/cm^2

base dose level. A JEOL EBL system (model: JBX 9300FS) was used for the EBL procedure.

4. Development of the resultant patterned resist with a solution of MIBK:IPA 1:3 for 70s, followed by an IPA rinse for 30s. This step ensures the removal of the areas of the resists exposed by the electron beam. It is important to note here that the concentration of MIBK in the MIBK:IPA mixture, affects the sensitivity of the resist, with a higher concentration resulting in a higher sensitivity. Iterative testing with different developer concentrations has shown MIBK:IPA 1:3 to offer improved edge features in square-shaped nanoparticles, when compared to MIBK:IPA 1:1 which results in rounded edges for the same exposure dose.
5. A highly-directional LAB700 electron-beam evaporator with a vertical deposition is used for evaporating the metal layer. A highly directional, vertical/perpendicular deposition ensures minimal sidewall coverage due to the metal layers deposited at an angle to the substrate. The choice of the deposition rate affects, to a certain degree, the roughness of the surface and edges of the nanoparticle. This in turn, could affect both the morphology and optical properties of the fabricated nanoparticles. The effect of the deposition rate on the roughness of the particle surface will be briefly evaluated in Section A2.2.1.
6. The metallised samples are immersed in acetone and a manual pipette-based lift-off technique is used to remove the unexposed metallised resist layers. The duration of immersion in acetone is dependent on the sample – the quickest lift-off achieved with the current technique was 15min immersion time in acetone for 6% surface coverage of 100nm nanodiscs on a 2mm x 2mm Si substrate. Immediately after lift-off, the samples are immersed in high grade IPA to ensure complete removal of acetone. The final step involves a nitrogen-gun based drying of the sample.

A2.2 Development of the Bi-Layer EBL Process

A2.2.1 Effect of deposition rate on the surface roughness of the Ag layer

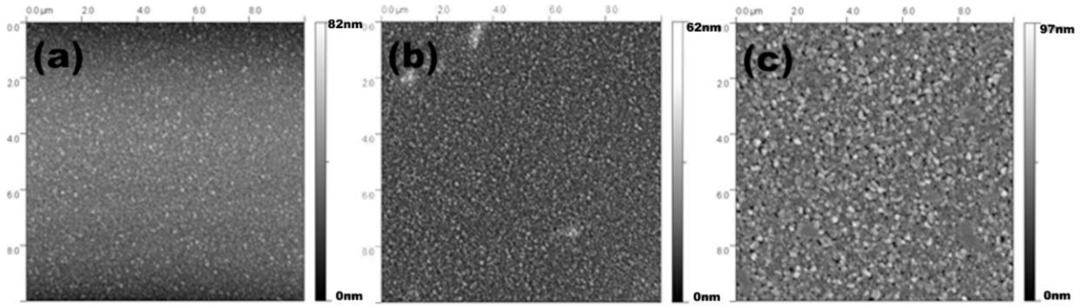

Figure 3. AFM images illustrating the effect of deposition rate on root-mean-square (RMS) surface roughness of the evaporated Ag layer on Si substrate. The resultant RMS roughness measurements for the different deposition rates have been calculated after the AFM images were adjusted by line correction by matching height median: **(a)** 0.1Ås^{-1}, surface roughness: 4.96nm **(b)** 1Ås^{-1}, surface roughness: 4.46nm **(c)** 10Ås^{-1}, surface roughness: 11.3 nm.

The stage of metal deposition needs to be optimised to achieve a metal layer which has a relatively smooth surface. This optimisation is crucial in order to avoid discrepancies in optical measurements due to surface/edge roughness in the metal nanoparticles. Before depositing Ag onto the developed resist samples, a surface roughness test was conducted by evaporating 30nm Ag metal layers onto a Si substrate at deposition rates of 0.1Ås^{-1}, 1Ås^{-1} and 10Ås^{-1}. This effect of deposition rate on the surface roughness of the metal layer is evident when comparing the AFM images in Figure 3. The resultant Ag surface at a deposition rate of 10Ås^{-1} exhibited a relatively high RMS surface roughness when compared to the Ag metal layers deposited at 0.1Ås^{-1} and 1Ås^{-1}. Based on these results, a deposition rate of 1Ås^{-1} was chosen to fabricate nanoparticles with relatively smooth surfaces.

A2.3 The E-beam Dose-level

A2.3.1 Effect of Dose-level on Bilayer Undercut

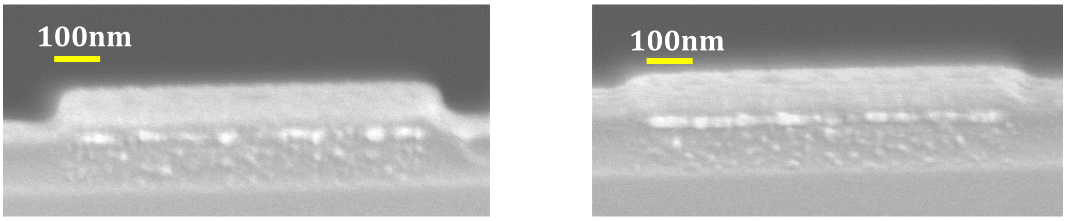

(a) -20%, no undercut **(b)** -40%, no undercut

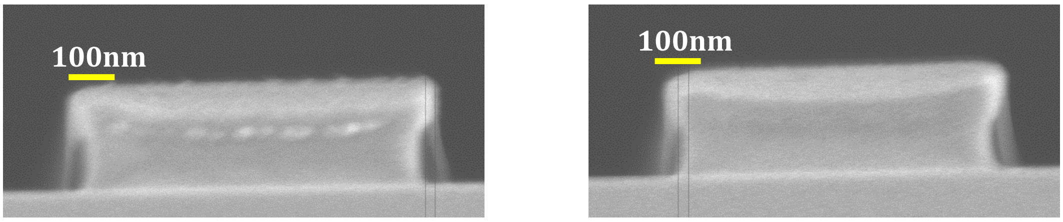

(c) +20%, undercut: 23nm **(d)** +40%, undercut: 26nm

Figure 4 (a-d) Cross sectional SEM images depicting an example of the effect of varying dose levels on the resultant undercut of the bi-layer resist. Note that base dose here is 800μC/cm^2 and the samples have been coated with a thin conductive layer of Au to enable SEM imaging.

In the preliminary development stage, the design patterns with nanosquares with dimensions in the order of 100 nm, were replicated on the bi-layer resist for 10 dose levels. The bi-layer resist on Si substrate was exposed to a range of dose levels: -50% to 50% in steps of 10%, in order to optimise the dose level for a suitable undercut. The undercut in the bi-layer resist was determined by analysing cross-sectional SEM images of the areas of resist sample exposed to the different dose levels (Figure 4(a-d)).

A2.3.2 Optimisation of Dose-level

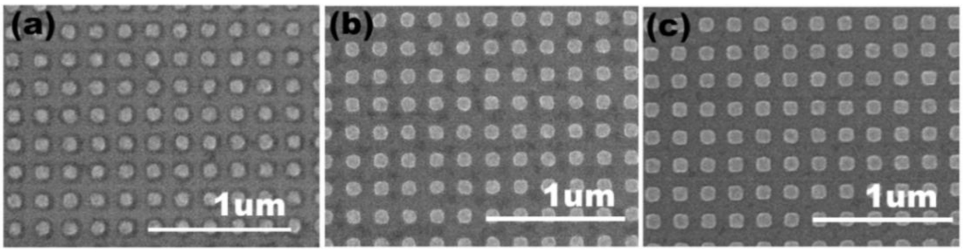

Figure 5 Effect of varying the dose level on resultant nanoparticle shape. Base dose level is 900μm/cm^2 **(a)** underexposed sample at +25% dose level **(b)** sample exposed at +55% dose level, still underexposed and features are not well resolved **(c)** sample exposed at the optimised +80% dose level; nanoparticles are close to the designed pattern and are well-resolved.

A series of dose tests were carried out to determine an optimised dose level for the current bilayer process. Figure 5 is an example of a periodic square nanoparticle pattern (pitch of 200nm) exposed at three different dose levels. The sample exposed at +25% of the base dose level is clearly underexposed. Figure 5c, shows the optimised +80% of base dose level for this particular pattern of periodically arranged nanoscale squares.

Surface coverage of nanodiscs (%)	**Dose level used ($\mu C/cm^2$)**	**Dose boostage (%) over base dose level of 900 $\mu C/cm^2$**
2	1386	54
6	1305	45
10	1206	40
12	1215	35

Table 1 Variance of optimised dose level with surface coverage of 100nm nanodiscs on a 2mm x 2mm Si sample area.

In addition to optimising for the nanoparticle shape, the dose level also needs to be optimised for the surface coverage of the nanoparticles. Table 1 shows the variance of the dose level with the surface coverage of the nanodiscs. The dose level is shown to decrease with increasing surface coverage of nanoparticles. Extremely high surface coverages may make a complete lift-off difficult to achieve (although this effect is yet to be tested).

Appendix 3: Additional Solar Cell Characterisation Details and Results

A3.1 EQE Measurement Technique[19]

The EQE of a solar cell is defined as the ratio of the number of carriers collected in the device to the number of photons of a given wavelength incident onto the device [74]. For single-junction solar cells, the spectrally-filtered output of a light source, (typically a Quartz tungsten halogen (QTH) or a Xenon lamp for the visible to near-infrared region), is used together with a monochromator to simulate the standard solar spectrum. The EQE value is then measured for each wavelength of the incident light (set by the wavelength step-size), across the specified wavelength range.

The first step in the measurement of EQE involves measuring the number of photons per second for a given wavelength of incident light. This can be determined as shown in Equation 1, by measuring the incident beam power (P(λ)) for a given wavelength:

$$\frac{Number\ of incident\ photons}{s} = P(\lambda).\frac{\lambda}{hc} \qquad (\mathbf{1})$$

Where, λ is the wavelength of incident light, *P(λ)* is the beam power measured at the incident wavelength, *h* is the Planck's constant and *c* is the speed of light.

P(λ) is determined using Equation 2, i.e. by measuring the generated photocurrent ($I_{ref}(\lambda)$) of a calibrated reference photodetector with a known spectral responsivity ($R_{ref}(\lambda)$):

$$R_{ref}(\lambda) = \frac{I_{ref}(\lambda)}{P(\lambda)} \qquad (\mathbf{2})$$

---

[19] The main equations and steps explained in this section have been obtained from references:

(i) IPCE Monochromator User Guide, Nathan Heston. [Online]. Available: mccl.chem.ufl.edu/sec/manual/User_Manual_MCCL_IPCE.docx. Accessed: 2014.

(ii) Bentham: Spectral Characterisation of Photovoltaic Devices, Techinical note. [Online]. Available: http://www.bentham.co.uk/pdf/PV_Technical_Note.pdf Accessed: 2014.

In order to accurately determine $I_{ref}(\lambda)$ and hence $P(\lambda)$, it is crucial to properly align and position the beam spot such that it covers an area on the photodetector equal to the active area of the test solar cell (often 1cm^2 is used as the standard active area for solar cells).

The second step in the measurement of EQE involves measuring the photocurrent of the test solar cell ($I_{cell}(\lambda)$) in order to determine the number of electrons per second, generated for a given wavelength of incident light (Equation 3)

$$\frac{Number\ of\ collected\ electrons}{s} = \frac{I_{cell}(\lambda)}{q} \qquad (\mathbf{3})$$

Where q is the electronic charge.

It is important to note that $I_{cell}(\lambda)$ is typically determined under short-circuit conditions (i.e. $V_{bias} = 0\,V$).

The EQE for a given wavelength is then given by dividing Equation 3 by Equation 1:

$$EQE(\lambda) = \frac{Number\ of\ collected\ electrons}{Number\ of\ incident\ photons} = \frac{I_{cell}}{q} . \frac{hc}{P(\lambda).\lambda} \qquad (\mathbf{4})$$

By substituting Equation 2 for $P(\lambda)$ into Equation 4, EQE can also be expressed as

$$EQE(\lambda) = \frac{I_{cell}(\lambda)}{I_{ref}(\lambda)} . \frac{hc}{q.\lambda} .\ R_{ref}(\lambda) \qquad (\mathbf{5})$$

A3.2 Additional Solar Cell Characterisation Results

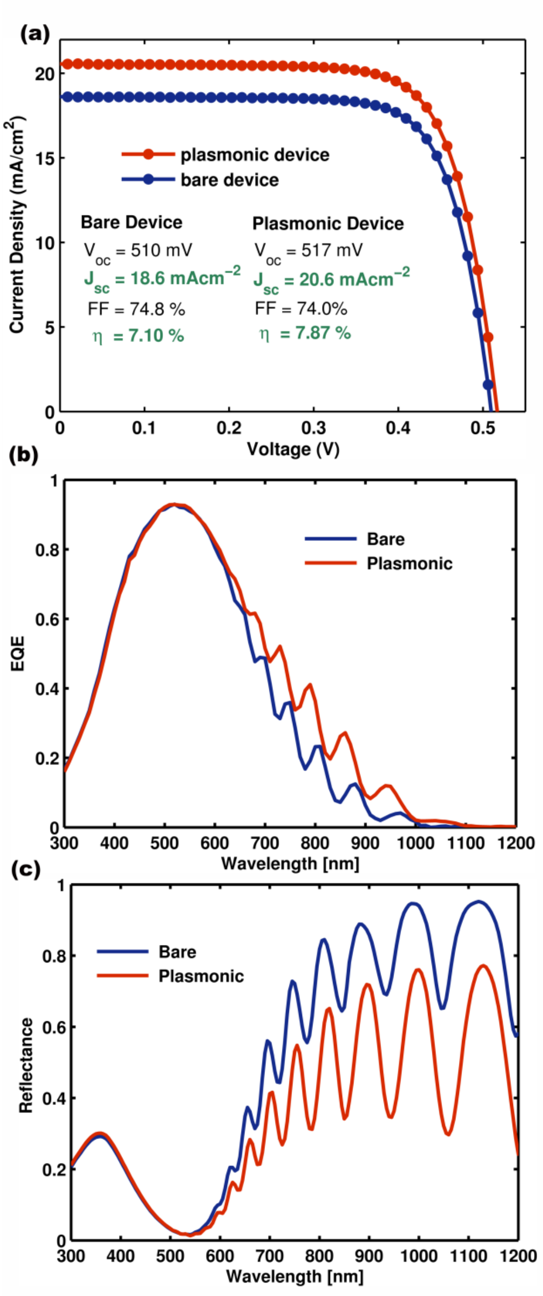

Figure 6 (a) Measured J-V characteristics **(b)** Measured external quantum efficiency (EQE) spectra and **(c)** Measured absorption spectra for the planar and plasmonic devices in device set B, with a 90nm disc-mirror separation. (110nm total rear ZnO thickness)

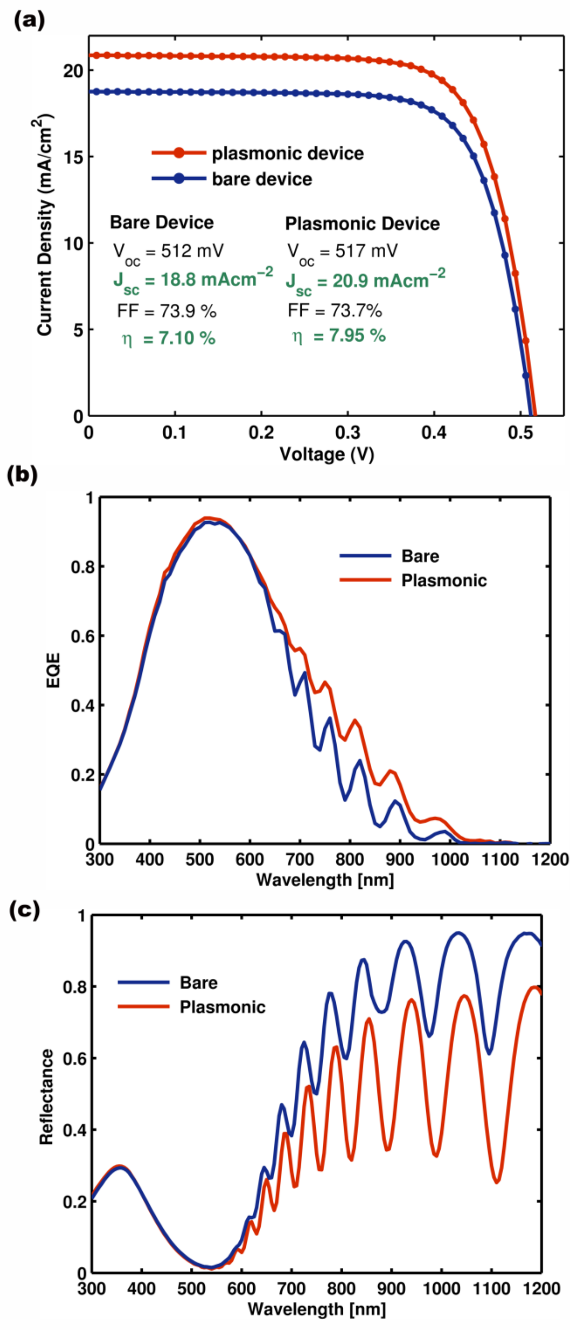

Figure 7 (a) Measured J-V characteristics **(b)** Measured external quantum efficiency (EQE) spectra and **(c)** Measured absorption spectra for the planar and plasmonic devices in device set C, with a 110nm disc-mirror separation. (130nm total rear ZnO thickness)

[This page intentionally left blank]

Bibliography

[1] A. Becquerel, *Comptes Rendus,* vol. 9, pp. 561-567, 1839.

[2] NREL, 2011. [Online]. Available: http://rredc.nrel.gov/solar/spectra/am1.5/.

[3] D. Chapin, C. Fuller and G. Pearson, *Journal of Applied Physics,* vol. 25, p. 676, 1954.

[4] M. A. Green, K. Emery, Y. Hishikawa and W. a. D. E. D. Warta, *Progress in Photovoltaics: Research and Applications,* vol. 21, pp. 1-11, 2013.

[5] A. Einstein, *Annalen der Physik,* vol. 17, pp. 132-148, 1905.

[6] J. Czochralski, *Zeitschrift für Physikalische Chemie,* vol. 19, pp. 219-221, 1918.

[7] C. Fritts.US Patent US1213613 A, 1880.

[8] V. Petrova-Koch, R. Iezel and A. Goetzberger, High-Efficient, Low-cost Photovoltaics: Recent Developments, Springer, 2008.

[9] A. Shah, J. Meier, E. Vallat-Sullivan, C. Droz, U. Kroll, N. Wyrsch, J. Guillet and U. Graf, *Thin Solid Films,* Vols. 403-404, pp. 179-187, 2002.

[10] M. Green, Solar Cells, Prentice Hall, 1982.

[11] K. Chopra, P. Paulson and V. Dutta, *Progress in Photovoltaics: Research and Applications,* vol. 12, pp. 69-92, 2004.

[12] A. Shah, E. Vallat-Sauvain, P. Torres, J. Meier, U. Kroll, C. Hof, C. Droz, M. Goerlitzer, N. Wyrsch and M. Vanecek, *Material Science and Engineering:B,* vol. 69-70, pp. 219-226, 2000.

[13] E. Vallat-Sauvain, U. Kroll, J. Meier, A. Shah and J. Pohl, *Journal of Applied Physics,* vol. 87, p. 3137, 2000.

[14] TU Delft Courses: Solar Cells, Chapter 7, [Online]. Available: http://ocw.tudelft.nl/fileadmin/ocw/courses/SolarCells/res00030/CH7_Thin_film_Si_solar_cells.pdf.

[15] S. Veprek and V. Marecek, *Solid State Electronics,* vol. 11, p. 683, 1968.

[16] M. Vanecek, *Journal of Non-Crystalline Solids,* vol. 967, p. 227, 1998.

[17] V. Jain and A. Verma, Physics of Semiconductor Devices, Springer, 2014.

[18] H. Sai and M. Kondo, *Journal of Applied Physics,* vol. 105, pp. 094511-1, 2009.

[19] U. Paetzold, E. Moulin, D. Michaelis, W. Bottler and C. Wacheter, *Applied Physics Letters,* vol. 99, p. 181105, 2011.

[20] H. Sai, H. Jia and M. Kondo, *Journal of Applied Physics,* vol. 108, p. 044505, 2010.

[21] W. Bottler, V. Smirnov, J. Hupkes and F. Finger, *Journal of Non-Crystalline Solids,* vol. 358, pp. 2474-2477, 2012.

[22] S. Hanni, D. T. L. Alexander, L. Ding, G. Bugnon, M. Boccard, C. Battaglia, P. Cuony, J. Escarre, G. Parascandolo, S. Nicolay, M. Cantoni, M. Despeisse, F. Meillaud and C. Ballif, *IEEE Journal of Photovoltaics,* vol. 3, p. 11, 2013.

[23] E. Moulin, J. Sukmanowski, M. Schulte, A. Gordijn, F. Royer and H. Stiebig, *Thin Solid Films,* vol. 516, pp. 6813-6817, 2008.

[24] H. Tan, L. Sivec, B. Yan, R. Santbergen, M. Zeman and A. Smets, *Applied Physics Letters,* vol. 102, p. 153902, 2013.

[25] H. Sai, Y. Kanamori and M. Kondo, *Applied Physics Letters,* vol. 98, p. 113502, 2011.

[26] Y. Liu et al., *Nature Communications,* vol. 2, p. 579, 2011.

[27] H. Stuart and D. Hall, *Physical Review Letters,* vol. 80, p. 5663, 1998.

[28] H. Atwater and A. Polman, *Nature Materials,* vol. 9, p. 206, 2010.

[29] X. Huang, P. Jain, I. El-Sayed and M. El-Sayed, *Lasers in Medical Science,* vol. 23, no. 217-228, 2008.

[30] J. Rovey, NASA, [Online]. Available: http://www.nasa.gov/content/plasmonic-force-propulsion-revolutionizes-nanopicosatellite-capability/.

[31] S. Maier, Plasmonics: Fundamentals and Applications, New York, USA: Springer Science & Business Media LLC, 2007.

[32] C. Bohren and D. Huffman, Absorption and scattering of light by small particles, Wiley, 1998.

[33] X. Wei and S. Weiss, *Optics Express,* vol. 19, p. 11330, 2011.

[34] E. Wijaya, C. Lenaerts, S. Maricot, J. Hastanin, S. Habraken, J. Vilcot, R. Boukherroub and S. Szunerits, *Solid State and Materials Science,* vol. 15, pp. 208-224, 2011.

[35] J.Mertz, *Journal of Optical Society of America:B,* vol. 17, p. 1906, 2000.

[36] U. Kreibig and M. Vollmer, Optical properties of metal clusters, Springer, 1995.

[37] P. West, S. Ishii, G. Naik, N. Emani, V. Shalev and A. Boltasseva, *Laser Photonics Review ,* vol. 4, pp. 795-808, 2010.

[38] G. Mie, *Annals of Physics,* vol. 25, p. 377, 1908.

[39] M. Brongersma and P. Kik, Surface Plasmon Nanophotonics, Springer, 2007.

[40] M. Farland and V. Duyne, *Nano Letters,* vol. 3, p. 1057, 2003.

[41] S. Underwood and P. Mulvaney, *Langmuir,* vol. 10, pp. 3427-3430, 1994.

[42] C. Langhammer, M. Schwind, B. Kasemo and I. Zoric, *Nano Letters,* vol. 8, pp. 1461-1471, 2008.

[43] S. Schatz, G. Chan, J. Zhao, E. M. Hicks and R. Van Duyne, *Nano Letters,* vol. 7, pp. 1947-1952, 2007.

[44] C. Langhammer, B. Kasemo, I. Zoric and Z. Yuan, *Nano Letters,* vol. 6, pp. 833-838, 2006.

[45] M. Hiramatsu, K. Imaeda, N. Horio and M. Nawata, *Journal of Vacuum Science and Technology: A,* vol. 16, pp. 669-673, 1998.

[46] J. Parsons, C. Burrows, J. Sambles and W. Barnes, *Journal of Modern Optics,* vol. 57, pp. 356-365, 2010.

[47] I. Sosa, C. Noguez and R. Barrera, *Journal of Physical Chemistry: B,* vol. 107, pp. 6269-6275, 2003.

[48] J. Webbs, *Reports on Progress in Physics,* vol. 58, pp. 1673-1712, 1995.

[49] K. Yee, *IEEE Trans. Ant. Prop.,* vol. 14, p. 302, 1966.

[50] P. Yang, G. Kattawara and K. Liou, *Applied Optics,* vol. 43, pp. 4611-4624, 2004.

[51] A. Taflove and S. Hagness, Computation Electrodynamics: The Finite Difference Time Domain Method, Boston: Artech House, 2005.

[52] B. Wiley, S. Im, Z. Li, J. McLellan, A. Siekkinen and Y. Xia, *Journal of Physical Chemistry: B,* vol. 110, pp. 15666-15675, 2006.

[53] B. Wiley, Y. Sun and Y. Xia, *Nano Letters,* vol. 7, pp. 1032-1036, 2007.

[54] J. Bhattacharya, N. Chakravarty, S. Pattnaik, W. Slafer, R. Biswas and V. Dalal, *Applied Physics Letters,* vol. 99, p. 131114, 2011.

[55] I. Zoric, M. Zach, B. Kasemo and C. Langhammer, *ACS Nano,* vol. 5, pp. 2535-2546, 2011.

[56] C. Cobley, S. Skrabalak, D. Campbell and Y. Xia, *Plasmonics,* vol. 4, pp. 171-179, 2009.

[57] J. Anker, W. Hall, O. Lyanders, N. C. Shah, J. Zhao and R. Van Duyne, *Nature*

Materials, vol. 7, pp. 442-453, 2008.

[58] C. Haynes and R. Van Duyne, *Journal of Physical Chemistry: B,* vol. 107, pp. 7426-7433, 2003.

[59] W.E.I. Sha, W.C.H. Choy, Y.G. Liu and W.C. Chew, *Applied Physics Letters,* vol. 99, p. 113304, 2011.

[60] V. Kochergin, L. Neely, C. Jao and H.D. Robinson, *Applied Physics Letters,* vol. 98, p. 133305, 2011.

[61] T.L. Temple, G.D.K. Mahanama, H.S. Reehal and D.M. Bagnall, *Solar Energy Materials and Solar Cells,* vol. 93, p. 1978, 2009.

[62] E. G. Matveeva, I. Gryczynski, A. Barnett, Z. Leonenko, J.R. Lakowicz and Z. Gryczynski, *Analytical Biochemistry,* vol. 363, p. 239, 2007.

[63] K. Drexhage, *Progress in Optics,* vol. 12, p. 165, 1974.

[64] P. Johansson, *Physical Review B,* vol. 64, pp. 165405-1, 2001.

[65] K. Catchpole and S. Pillai, *Journal of Applied Physics,* vol. 100, pp. 044504-1, 2006.

[66] W. Holland and D. Hall, *Physical Review Letters,* vol. 52, p. 1041, 1984.

[67] H. Stuart and D. Hall, *Applied Physics Letters,* vol. 69, p. 2327, 1996.

[68] U. Paetzold, M. Matthias, E. Moulin, V. Smirnov, B. Pieters, U. Rau and R. Carius, *Materials Science and Engineering: B,* vol. 178, p. 631, 2012.

[69] Y. Chu and K. Crozier, *Optics Letters,* vol. 34, p. 244, 2009.

[70] H. Mizuno, H. Sai, K. Matsubara and M. Kondo, *Japanese Journal of Applied Physics,* vol. 51, p. 042302, 2012.

[71] J. Chantana, Y. Yang, Y. Sobajima, C. Sada, A. Matsuda and H. Okamoto, *Journal of Non-Crystalline Solids,* vol. 358, pp. 2319-2323, 2012.

[72] K. Catchpole and A. Polman, *Applied Physics Leters,* vol. 93, pp. 191113-1, 2008.

[73] C. Eminain, F.-J. Haug, O. Cubero, X. Niquille and C. Ballif, *Progress in Photovoltaics: Research and Applications,* vol. 19, pp. 260-265, July 2011.

[74] S. Bowden and C. Honsberg. [Online]. Available: http://pvcdrom.pveducation.org/CELLOPER/QUANTUM.HTM.

[75] E. Yablonovitch, *Journal of the Optical Society of America,* vol. 72, pp. 899-907, 1982.

[76] P. B. Christy and R.W.Johnson, *Phys. Rev. B.,* vol. 6, p. 4370, 1972.

[77] C. Bohren, *American Journal of Physics,* vol. 51, pp. 323-327, 1983.

[78] Lumerical [Online].
Available: http://docs.lumerical.com/en/fdtd/user_guide_tfsf_sources.html.
Accessed: 2011

[79] Lumerical [Online].
Available:http://docs.lumerical.com/en/fdtd/user_guide_integrating_poynting_vector.html.
Accessed: 2011

[80] H.R. Philipp, "Silicon Dioxide (Glass)," in *Handbook of Optical Constants*, New York, E.D. Palik Ed., Academic, 1985, p. 749.

[81] T. Doi, K. Toyoda and Y. Tanimura, *Applied Optics,* vol. 36, no. 28, pp. 7157-7158, 1997.

[82] R.S.A. Sesuraj, T.L. Temple and D.M. Bagnall, in *MRS Online Proceedings (MRS Fall Meeting 2011)*, Boston, 2011.

[83] I. Romero, J. Aizpurua, W. Bryant and F. Javier Garcia de Abajo, *Optics Express,* vol. 14, pp. 9988-9999, 2006.

[84] "NTUF EBL Resists and Processing," [Online]. Available: https://depts.washington.edu/ntuf/facility/docs/NTUF_Resists.pdf.

[85] D. Payne, S. Boden, O. Clark, A. Delahoy and D.M.Bagnall, "Characterisation of Experimental Textured ZnO:Al Films for Thin Fiilm Solar Cell Applications and Comparison with Commerical and Plasmonic Alternatives," in *35th IEEE Photovoltaic Specialists Conference*, Honolulu HI, 2010.

[86] H.R. Philipp, "Silicon," in *Handbook of Optical Constants*, New York, E.D. Palik Ed., Academic, 1985, p. 547.

[87] G. F. Bukhard, E. T. Hoke and M. D. McGehee, *Advanced Materials,* vol. 22, pp. 3293-3297, 2010.

[88] T. L. Temple and D. M. Bagnall, *Journal of Applied Physics,* vol. 109, p. 084343, 2011.

[89] Y. Yang, S. Pillai, H. Kampwerthy, M. Green, H. Mehrvarz and A. Ho-Baillie, *Solar Energy Materials and Solar Cells,* vol. 117, pp. 343-349, 2013.

[90] L. Frass and L. Partain, Solar Cells and their Applications, Wiley, 2010.

[91] Solar Cells [Online] , H. Lund, R. Nilsen, O. Salomatova, D. Skåre and E. Riisem

Available: http://org.ntnu.no/solarcells/pages/Chap5.php
Accessed: 2013.

[92] D. Pines and D. Bohm, *Physical Review,* vol. 85, p. 338, 1952.

[93] J. Maxwell, *Royal Society Transactions,* vol. CLV, p. 459, 1865.

[94] R. Ritchie, *Physical Review,* vol. 106, p. 874, 1957.

[95] C. Powell and J. Swan, *Physical Review,* vol. 115, p. 869, 1959.

[96] E. Stern and R. Ferrell, *Physical Review,* vol. 120, p. 130, 1960.

[97] A. Clebsch, *Journal für Mathematik,* vol. 61, p. 195, 1863.

[98] L. Rayleigh, *Proceedings of the Royal Society of London,* vol. 567, p. 25, 1910.

[99] A. Love, *Proceedings of the London Mathematical Society,* vol. 30, p. 308, 1899.

[100] O. Keller, "Optical works of L.V. Lorenz," *Progress in Optics,* vol. 43, p. 285, 2002.

[101] P. Andrew and W. Barnes, *Physical Review B,* vol. 64, p. 125405, 2001.

[102] G. Lévêque and J. Martin, *Optics Express,* vol. 14, p. 9971, 2006.

[103] F. Beck, E. Verhagen, S. Mokkapati, A. Polman and K. Catchpole, *Optics Express,* vol. 19, p. A153, 2011.